Cell Reports
Medicine

Article

Pharmacologic reversal of advanced Alzheimer's disease in mice and identification of potential therapeutic nodes in human brain

Graphical abstract

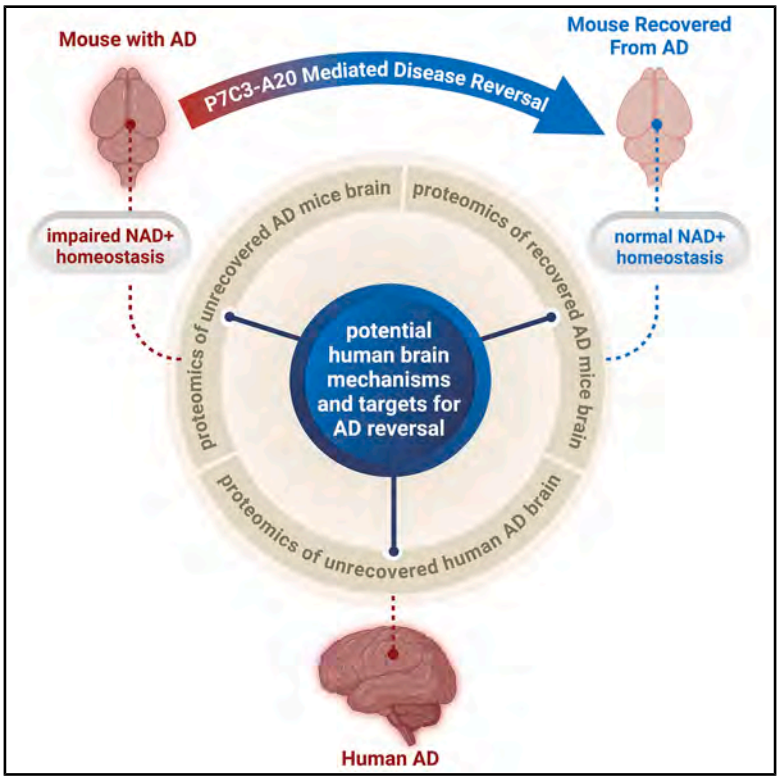

Highlights

- Severity of Alzheimer's disease (AD) correlates with NAD^+ homeostasis dysregulation
- Preserving brain NAD^+ homeostasis prevents AD in mice
- Restoring brain NAD^+ homeostasis reverses advanced AD in mice
- Multiomics across human and mouse AD brain identifies nodes for human AD reversal

Authors

Kalyani Chaubey, Edwin Vázquez-Rosa, Sunil Jamuna Tripathi, ..., David E. Kang, Bindu D. Paul, Andrew A. Pieper

Correspondence

andrew.pieper@case.edu

In brief

Chaubey et al. demonstrate that restoration of brain resilience reverses advanced disease in two different mouse models of Alzheimer's disease (AD), challenging the century-long dogma of AD irreversibility, and further identify potential therapeutic nodes in human AD brain.

Chaubey et al., 2026, Cell Reports Medicine 7, 102535
January 20, 2026 Published by Elsevier Inc.
https://doi.org/10.1016/j.xcrm.2025.102535

CellPress

Cell Reports Medicine

CellPress
OPEN ACCESS

Article

Pharmacologic reversal of advanced Alzheimer's disease in mice and identification of potential therapeutic nodes in human brain

Kalyani Chaubey,[1,2,3,4] Edwin Vázquez-Rosa,[1,2,3,4] Sunil Jamuna Tripathi,[5] Min-Kyoo Shin,[1,2,3,4,6,7] Youngmin Yu,[1,2,3,4,8] Matasha Dhar,[1,2,3,4] Suwarna Chakraborty,[5] Mai Yamakawa,[9] Xinming Wang,[10] Preethy S. Sridharan,[1,2,3,4,11] Emiko Miller,[1,2,3,4,11] Zea Bud,[1,2,3,4,12] Sofia G. Corella,[1,2,3,4,10] Sarah Barker,[1,2,3,4,10] Salvatore G. Caradonna,[1,2,3,4,10] Yeojung Koh,[1,2,3,4,10] Kathryn Franke,[1,2,3,4] Coral J. Cintrón-Pérez,[1,2,3,4] Sophia Rose,[1,2,3,4,13,14]

(Author list continued on next page)

[1]Department of Psychiatry, Case Western Reserve University, Cleveland, OH 44106, USA
[2]Brain Health Medicines Center, Harrington Discovery Institute, University Hospitals Cleveland Medical Center, Cleveland, OH 44106, USA
[3]Geriatric Psychiatry, GRECC, Louis Stokes VA Medical Center, Cleveland, OH 44106, USA
[4]Institute for Transformative Molecular Medicine, School of Medicine, Case Western Reserve University, Cleveland, OH 44106, USA
[5]Department of Physiology, Pharmacology & Therapeutics, Johns Hopkins University School of Medicine, Baltimore, MD 21205, USA
[6]College of Pharmacy and Research Institute of Pharmaceutical Sciences, Seoul National University, Seoul 08226, Republic of Korea
[7]Natural Products Research Institute, College of Pharmacy, Seoul National University, Seoul 08826, Republic of Korea
[8]University of Toledo College of Medicine and Life Sciences, Toledo, OH 43606, USA
[9]Department of Neurology, David Geffen School of Medicine, University of California, Los Angeles, Los Angeles, CA, USA
[10]Department of Pathology, Case Western Reserve University, Cleveland, OH 44106, USA
[11]Department of Neurosciences, Case Western Reserve University, Cleveland, OH 44106, USA
[12]Frances Payne Bolton School of Nursing, Case Western Reserve University, Cleveland, OH 44106, USA
[13]Shaker Heights High School, Shaker Heights, OH 44120, USA
[14]Carnegie Mellon University, Pittsburgh, PA 15213, USA
[15]Hathaway Brown School, Shaker Heights, OH 44122, USA
[16]Massachusetts Institute of Technology, Cambridge, MA 02139, USA
[17]Beachwood High School, Cleveland, OH 44122, USA
[18]Department of Neurology, Case Western Reserve University School of Medicine, Cleveland, OH 44106, USA
[19]Cryo-Electron Microscopy Core, Case Western Reserve University School of Medicine, Cleveland, OH, USA
[20]Mesulam Institute for Cognitive Neurology and Alzheimer's Disease, Feinberg School of Medicine, Northwestern University, Chicago, IL, USA
[21]Department of Psychiatry and Behavioral Sciences, Northwestern University Feinberg School of Medicine, Chicago, IL 60611, USA

(Affiliations continued on next page)

SUMMARY

Alzheimer's disease (AD) is traditionally considered irreversible. Here, however, we provide proof of principle for therapeutic reversibility of advanced AD. In advanced disease amyloid-driven 5xFAD mice, treatment with P7C3-A20, which restores nicotinamide adenine dinucleotide (NAD^+) homeostasis, reverses tau phosphorylation, blood-brain barrier deterioration, oxidative stress, DNA damage, and neuroinflammation and enhances hippocampal neurogenesis and synaptic plasticity, resulting in full cognitive recovery and reduction of plasma levels of the clinical AD biomarker p-tau217. P7C3-A20 also reverses advanced disease in tau-driven PS19 mice and protects human brain microvascular endothelial cells from oxidative stress. In humans and mice, pathology severity correlates with disruption of brain NAD^+ homeostasis, and the brains of nondemented people with Alzheimer's neuropathology exhibit gene expression patterns suggestive of preserved NAD^+ homeostasis. Forty-six proteins aberrantly expressed in advanced 5xFAD mouse brain and normalized by P7C3-A20 show similar alterations in human AD brain, revealing targets with potential for optimizing translation to patient care.

INTRODUCTION

Alzheimer's disease (AD), commonly considered irreversible since its discovery over a century ago, is the leading cause of dementia and is projected to afflict >150 million people by 2050.[1–3] Current therapies targeting amyloid beta (Aβ) or clinical symptoms offer limited benefit to patients,[4–20] highlighting the need for complementary and alternative treatments. Notably, people

This is an open access article under the CC BY-NC-ND license (http://creativecommons.org/licenses/by-nc-nd/4.0/).

Hua Fang,[1,2,3,4,15,16] Adrian A. Cintrón-Pérez,[1,2,3,4,17] Taylor Tomco,[1,2,3,4] Xiongwei Zhu,[10,18] Hisashi Fujioka,[19] Tamar Gefen,[20,21] Margaret E. Flanagan,[20,22,23] Noelle S. Williams,[24] Brigid M. Wilson,[3,25] Lawrence Chen,[26] Lijun Dou,[27] Feixiong Cheng,[27,28,29] Jessica E. Rexach,[9] Jung-A Woo,[10] David E. Kang,[10,30] Bindu D. Paul,[5,31,32,33] and Andrew A. Pieper[1,2,3,4,10,11,33,34,*]

[22]Glenn Bigg's Institute for Alzheimer's and Neurodegenerative Diseases, San Antonio, TX 78229, USA
[23]Departments of Pathology and Neurology, University of Texas Health Science Center at San Antonio, San Antonio, TX 78229, USA
[24]Department of Biochemistry, University of Texas Southwestern Medical Center, Dallas, TX 75390, USA
[25]Division of Infectious Diseases and HIV Medicine in the Department of Medicine, Case Western Reserve University, Cleveland, OH 44106, USA
[26]Lawrence Chen Program in Neurogenetics, Department of Neurology, David Geffen School of Medicine, University of California, Los Angeles, Los Angeles, CA 90095, USA
[27]Department of Genomic Sciences and Systems Biology, Cleveland Clinic Research, Cleveland Clinic, Cleveland, OH 44106, USA
[28]Cleveland Clinic Genome Center, Cleveland Clinic Research, Cleveland Clinic, Cleveland, OH 44106, USA
[29]Department of Molecular Medicine, Cleveland Clinic Lerner College of Medicine, Case Western Reserve University, Cleveland, OH 44106, USA
[30]Louis Stokes VA Medical Center, Cleveland, OH 44106, USA
[31]Department of Psychiatry and Behavioral Sciences, Johns Hopkins University School of Medicine, Baltimore, MD 21205, USA
[32]The Solomon H. Snyder Department of Neuroscience, Johns Hopkins University School of Medicine, Baltimore, MD 21205, USA
[33]Lieber Institute for Brain Development, Baltimore, MD 21205, USA
[34]Lead contact
*Correspondence: andrew.pieper@case.edu
https://doi.org/10.1016/j.xcrm.2025.102535

who carry autosomal dominant AD mutations can remain symptom-free for decades before clinical onset, and some individuals known as nondemented with Alzheimer's neuropathology (NDAN) accumulate abundant amyloid plaques yet remain cognitively intact.[21–27] These findings imply the existence of intrinsic brain resilience mechanisms that delay or counteract disease progression, suggesting the possibility of preserving or enhancing such processes to modify disease trajectory or foster recovery from AD.

Nicotinamide adenine dinucleotide (NAD^+) homeostasis is central to cellular resilience against oxidative stress, DNA damage, neuroinflammation, blood-brain barrier (BBB) deterioration, impaired hippocampal neurogenesis, synaptic plasticity deficits, and neurodegeneration. Prior studies report NAD^+ depletion in AD models and partial attenuation of pathology with NAD^+ precursor supplementation.[28–39] However, NAD^+ precursors may also produce supraphysiologic NAD^+ levels that promote cancer.[40–50] Thus, maintaining physiologic NAD^+ homeostasis is critical. Notably, the relationship between NAD^+ homeostasis, disease severity, and therapeutic reversibility of AD has not been previously explored.

Here, we show that pharmacologic restoration of NAD^+ homeostasis via P7C3-A20, a neuroprotective compound that restores NAD^+ homeostasis without producing supraphysiologic NAD^+ levels,[51–56] reverses cognitive deficits and neuropathology in advanced Aβ- and tau-driven AD models. We identify conserved molecular signatures between human and mouse AD and show that the magnitude of NAD^+ homeostasis disruption correlates with pathology and symptom severity in mouse and human AD. We also demonstrate that NDAN brains display transcriptional profiles compatible with preserved NAD^+ homeostasis and that P7C3-A230 restores NAD^+ homeostasis and prevents oxidative damage and mitochondrial dysfunction in oxidatively stressed human brain microvascular endothelial cells (HBMVECs), a key component of the BBB. We additionally identify 46 conserved protein alterations in human and mouse AD brain that are corrected by AD reversal, together with overlapping transcriptomic changes in human AD. This highlights potential mechanisms and therapeutic targets for preserving and restoring brain resilience to AD.

These findings of cognitive recovery and pathological reversal in diverse models of advanced AD support disease progression as modifiable and driven by diminished brain resilience, with early cognitive impairment resulting from processes that promote neurodegeneration rather than solely from fixed neuronal loss. We propose that therapies to restore brain resilience, such as normalization of NAD^+ homeostasis, merit clinical evaluation for prevention and reversal of AD and related dementias.

RESULTS

Brain NAD^+ homeostasis normalization in amyloid-driven 5xFAD mice by P7C3-A20

We assessed whether brain NAD^+ homeostasis deteriorates with disease progression in 5xFAD mice with paternally inherited transgenes, chosen for their Aβ aggregation and human-typical tau phosphorylation (Ser202/Thr205) despite lacking tau mutations, alongside BBB deterioration, oxidative stress, DNA damage, neuroinflammation, impaired hippocampal neurogenesis, synaptic deficits, neurodegeneration, and cognitive decline.[57–62] Normal brain NAD^+/NADH was observed in 2-month-old (presymptomatic) 5xFAD mice (Figure S1A). By 6 months, however, when pathology and cognitive deficits are apparent, 5xFAD mice exhibited a 30% reduction in brain NAD^+/NADH (Figure S1A), progressing to 45% by 12 months (Figure 1A).

To evaluate normalization of NAD^+ homeostasis, we treated mice with P7C3-A20, a neuroprotective compound that restores NAD^+ homeostasis without raising NAD^+ to supraphysiologic levels.[51–56,63–95] Steady-state plasma (Figure S1B) and brain (Figure S1C) P7C3-A20 levels were achieved by daily intraperitoneal (i.p.) P7C3-A20 (10 mg/kg/day) injections. There were no sex-specific differences, and P7C3-A20 did not elevate brain

CellPress
OPEN ACCESS

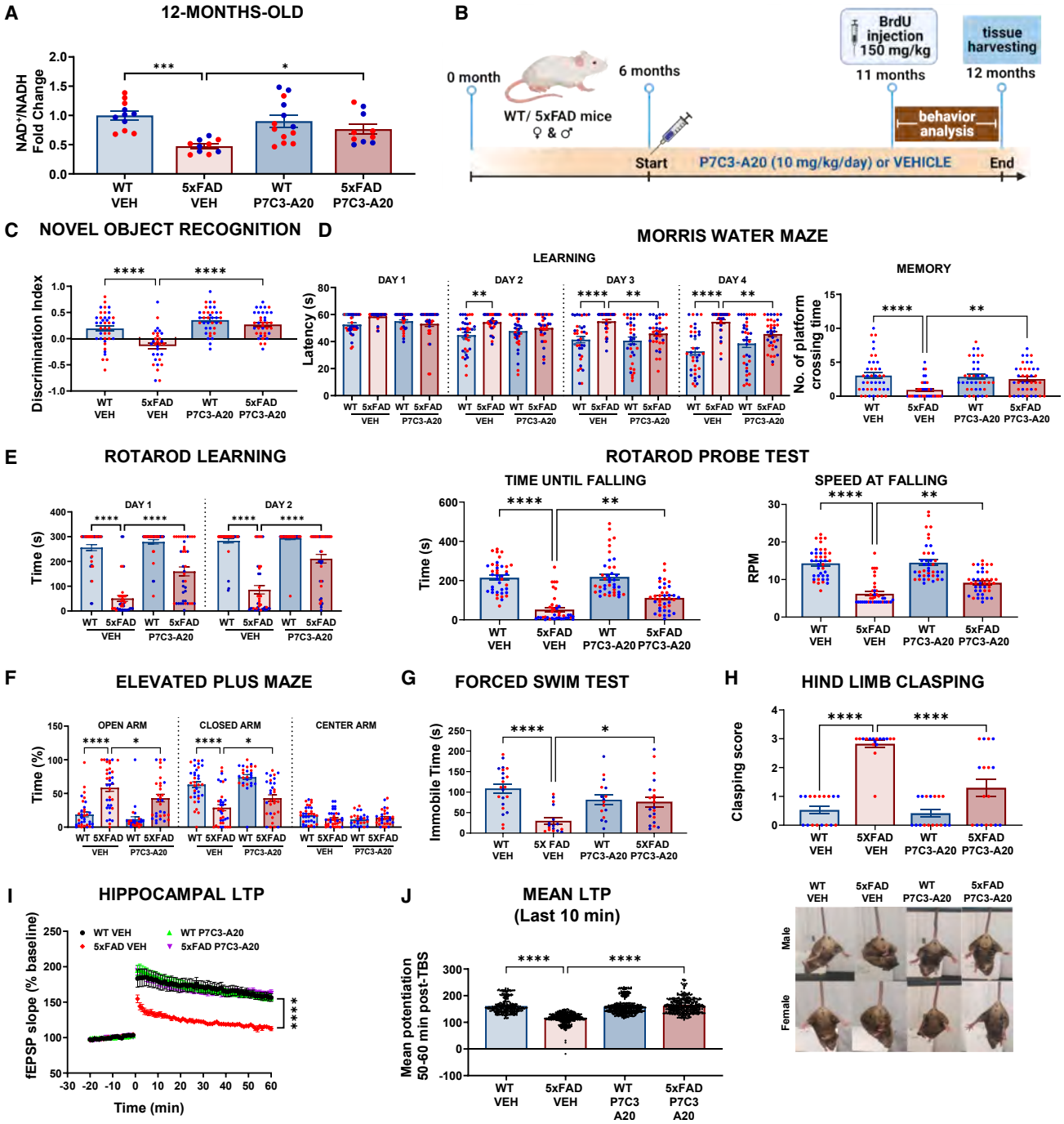

Figure 1. P7C3-A20 restores brain NAD$^+$ homeostasis, cognitive function, and synaptic plasticity in aged symptomatic 5xFAD mice

(A) Daily P7C3-A20 from 6 to 12 months of age normalizes brain NAD$^+$/NADH in 12-month-old 5xFAD mice without affecting WT littermates. (n = 5 females, 5–8 males).

(B) Schematic of Alzheimer's disease reversal study.

(C) Impaired discrimination index (memory) in NOR is reversed in 12-month-old 5xFAD mice. (n = 16–20 females, 15–21 males).

(D) Learning (latency to find the platform) and memory (number of platform crossings in probe test) in the Morris water maze are impaired in 12-month-old 5xFAD mice and reversed by P7C3-A20. (n = 17–22 females, 16–20 males).

(E) Learning in the accelerating rotarod test is impaired in 12-month-old 5xFAD mice and reversed by P7C3-A20. Motor performance is impaired in 12-month-old 5xFAD mice (time until falling and speed at falling) and reversed by P7C3-A20. (n = 20 females, 20 males).

(F) Twelve-month-old 5xFAD mice display abnormal anxiolytic-like activity in the elevated plus maze, spending more time in open arms and less in closed arms. (n = 15–18 females, 12–18 males).

(legend continued on next page)

NAD^+/NADH above normal (Figure S1D). Administration from 2 to 6 months prevented NAD^+ homeostasis disruption (Figure S1A), and administration from 6 to 12 months restored NAD^+ homeostasis (Figure 1A).

Experimental design for AD prevention and reversal

For evaluating AD prevention, a mouse cohort designated "mid-disease stage" received daily P7C3-A20 (10 mg/kg, i.p.) from 2 to 6 months of age, throughout the window when cognitive impairment typically emerges (Figure S1E). For AD reversal, a separate cohort designated "advanced-disease stage" received the same dose from 6 to 12 months, spanning established pathology and cognitive decline (Figure 1B). One month before endpoint, mice underwent behavioral analysis and received bromodeoxyuridine (BrdU) to label dividing cells for assessing hippocampal neurogenesis. Brains were analyzed via immunohistochemistry, biochemical assays, and transmission electron microscopy (TEM).

Prevention and reversal of symptoms in amyloid-driven 5xFAD mice by P7C3-A20

In the novel object recognition (NOR) test, which measures the preference for exploring a novel vs. a familiar object (discrimination index),[96] vehicle (VEH)-treated 5xFAD mice showed impaired memory at mid and advanced stages of disease, which P7C3-A20 prevented and reversed, respectively (Figures S1F and 1C). P7C3-A20 also prevented and reversed deficits in spatial learning and memory in the Morris water maze (Figures S1G and 1D).[97] Deficient motor learning and coordination on the accelerating rotarod[98] in advanced-disease was prevented by P7C3-A20, with no change at mid-disease (Figures 1E and S1H).

Psychiatric symptoms are common in AD.[99] In the elevated plus maze,[100] 5xFAD mice display anxiolytic-like greater time in the open arms,[101] which P7C3-A20 prevented and reversed at mid and advanced stages (Figures S1I and 1F). In the forced swim test,[102] advanced-disease, but not mid-disease, 5xFAD mice showed increased mobility, which was blocked by P7C3-A20 (Figures 1G and S1J). Hindlimb clasping, characteristic of neurodegeneration models,[103] in advanced-disease 5xFAD mice was prevented by P7C3-A20 (Figure 1H).

Prevention and reversal of impaired hippocampal synaptic plasticity in amyloid-driven 5xFAD mice by P7C3-A20

To assess synaptic function, we measured hippocampal long-term potentiation (LTP) (Figure S1K). Baseline synaptic transmission (field excitatory postsynaptic potential input/output curves) did not differ across groups (Figures S1L and S1M). LTP was reduced in mid-disease (Figure S1N), more severely in advanced-disease (Figure 1I), and preserved (Figures S1N and S1O) and restored (Figures 1I and 1J), respectively, by P7C3-A20.

Prevention and reversal of amyloid and tau pathology in amyloid-driven 5xFAD mice by P7C3-A20

Thioflavin-S staining, which detects unbranched protein fibers with secondary β-sheets forming protease-resistant amyloid, revealed P7C3-A20-mediated diminished amyloid accumulation in mid- (Figure S2A) and advanced-disease (Figure 2A), without altering genetically driven Aβ production (6E10 monoclonal antibody against amino acids 1–16 of Aβ[104]; Figures 2B and S2B). Levels of amyloid precursor protein (APP) and both soluble and insoluble Aβ peptides (1–40 and 1–42) in 5xFAD mice were unchanged by P7C3-A20 at both stages (Figures 2C–2E and S2C–S2E), consistent with β-site APP-cleaving enzyme 1 and γ-secretase enzymes being NAD^+ independent. However, amyloid protein clearance, which was affected, relies on NAD^+ homeostasis.[30,105,106]

There were no changes in total tau or tau phosphorylation in mid-disease (Figures S2C and S2F). Advanced-disease mice showed tau phosphorylation at Ser202/Thr205 that was prevented by P7C3-A20 (Figures 2C and 2F), with no changes in total tau and no effect of P7C3-A20 on amyloid or tau in wild-type (WT) mice (Figures 2A–2F and S2A–S2F).

Aβ brain pathology begins more than 20 years before clinical symptoms,[107–110] coinciding with the emergence of tau pathology.[111] Phospho-tau Thr217 (p-tau217) is the most sensitive plasma biomarker of cerebral Aβ burden prior to AD tau pathology,[112–117] and we observed elevated plasma p-tau 217 in advanced, but not mid, stages of disease, which was reduced by P7C3-A20 (Figures 2G, 2H, and S2G).

Prevention and reversal of BBB deterioration in amyloid-driven 5xFAD mice by P7C3-A20

The BBB is compromised early in mouse and human AD.[118–121] TEM revealed disrupted astrocytic endfeet and open perivascular gaps in mid-disease (Figure S2H), which P7C3-A20 prevented (Figure S2H). More extensive BBB deterioration in advanced-disease was reversed by P7C3-A20 (Figure 2I). Structural loss correlated with abnormal infiltration of peripheral immunoglobulin (IgG) into brain parenchyma that was prevented and reversed by P7C3-A20 (Figures 2J and S2I).

BBB pericytes, critical for vascular stability, capillary flow, and toxin clearance, degenerate in AD.[122,123] We observed reduced pericyte coverage of BBB microvascular endothelial cells at both mid (Figure S2J) and advanced (Figure 2K) stages of disease, which P7C3-A20 prevented and reversed (Figures S2J

(G) Twelve-month-old 5xFAD mice display reduced immobility time in the forced swim test, which is prevented by P7C3-A20. (n = 9–11 females, 6–12 males).
(H) Twelve-month-old 5xFAD mice show abnormal hindlimb clasping, which is prevented by P7C3-A20. (n = 8 females, 9 males).
(I) Hippocampal LTP is impaired in 12-month-old 5xFAD mice and prevented by P7C3-A20. (n = 27 slices from 5 WT VEH females; 40 slices from 7 5xFAD VEH females; 38 slices from 5 WT P7C3-A20 females; 35 slices from 5 5xFAD P7C3-A20 females).
(J) Mean potentiation during the last 10 min of recording is impaired in 12-month-old 5xFAD mice and prevented by P7C3-A20. (values of n are same as in I).
There are no sex-specific differences in any groups. Each dot represents an individual sample. For mice, females are blue and males are red. Error bars are standard error of the mean. $^*p < 0.05$, $^{**}p < 0.01$, $^{***}p < 0.001$, $^{****}p < 0.0001$, one-way ANOVA and Dunnett multiple comparisons against 5xFAD VEH group, with two-way ANOVA for learning phase in (D) and for (I). See also Figure S1.

CellPress
OPEN ACCESS

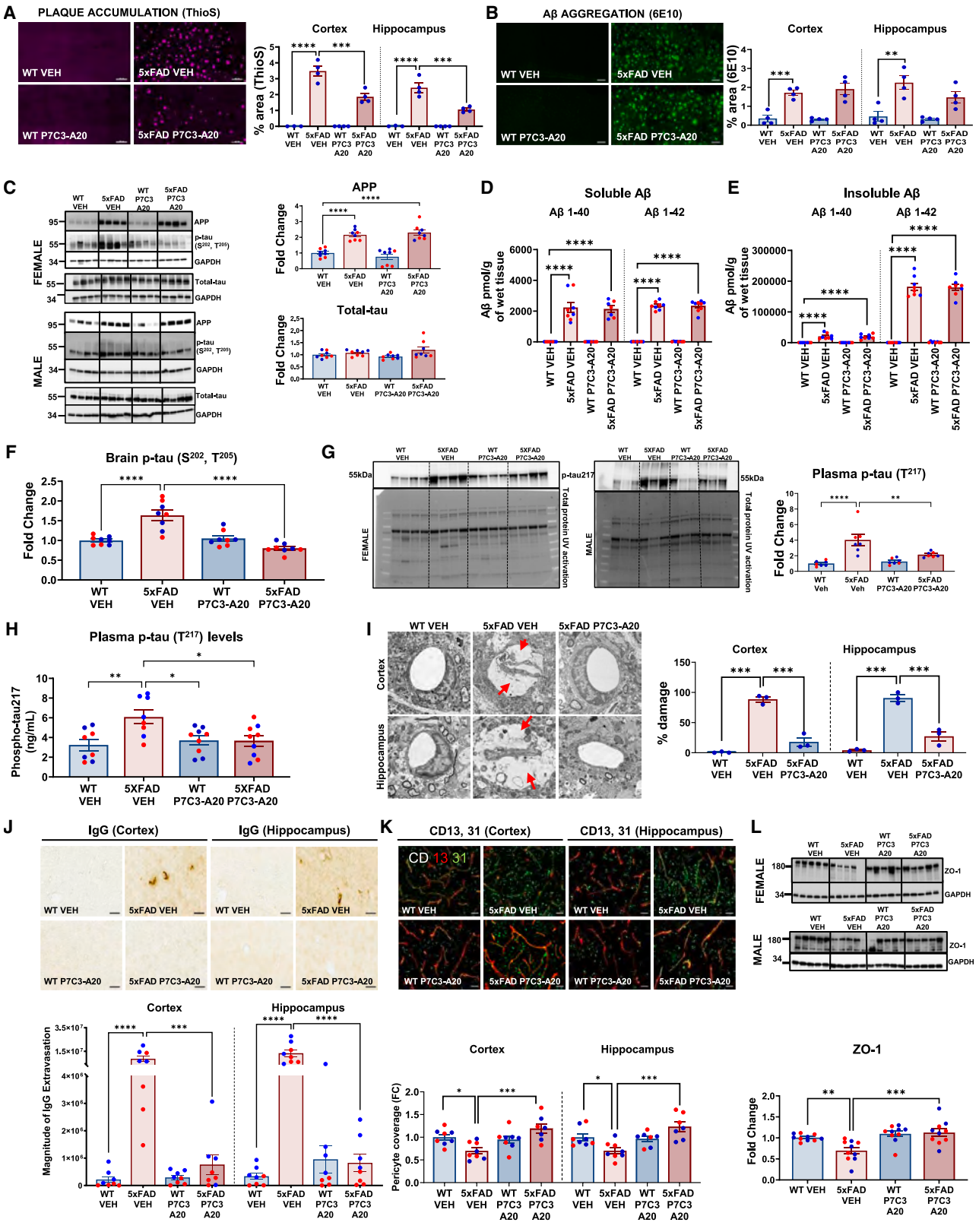

(legend on next page)

and 2K). Microvascular endothelial cell tight junction protein zonula occludens 1 (ZO-1), which declines in AD,[124] was reduced in advanced, but not mid, stages of disease and prevented by P7C3-A20 (Figures 2L and S2K).

Prevention and reversal of DNA damage and neuroinflammation in amyloid-driven 5xFAD mice by P7C3-A20

Brain DNA damage is exacerbated in AD and linked to neuroinflammation.[125,126] Using terminal deoxynucleotidyl transferase dUTP nick end labeling (TUNEL), we detected DNA strand breaks in 5xFAD mice at mid and advanced stages of disease (Figures S3A and 3A), which was prevented and reversed by P7C3-A20 (Figures S3A and 3A). Astrocytic glial fibrillary acidic protein (GFAP), indicating reactive, proinflammatory astrocytes,[127,128] was elevated in mid and advanced stages of disease and reduced by P7C3-A20 (Figures S3B and 3B). Microglial activation, assessed by ionized calcium-binding adaptor molecule 1 (IBA1),[129] was elevated at both stages and reduced by P7C3-A20 (Figures S3C and 3C). Microglia and astrocytes release inflammatory cytokines, and we measured interleukin-2 (IL-2), IL-13, tumor necrosis factor alpha (TNF-α), and interferon gamma (IFN-γ). IL-2 and IL-13, essential for cognition,[130–132] were unchanged at mid-disease, decreased in advanced-disease, and normalized by P7C3-A20 (Figures S3D and 3D). TNF-α and IFN-γ did not differ between groups (Figures S3D and 3D).

Protection from neurodegeneration in amyloid-driven 5xFAD mice by P7C3-A20

Neuronal loss in AD is measurable by reduced neuronal marker NeuN.[133] Mid-disease mice showed normal NeuN (Figure S3E), indicating that neuronal death is not required for AD-like symptoms. Advanced-disease mice exhibited reduced NeuN, which P7C3-A20 prevented (Figure 3E).

Impaired survival of young hippocampal neurons, another feature of AD,[134–136] showed a non-significant trend at mid-disease (Figure S3F) and significant reduction in advanced-disease, which was prevented by P7C3-A20 (Figure 3F).

Restoration of NAD^+ homeostasis and protection against oxidative damage in 5xFAD mouse brain and human brain microvascular endothelial cells by P7C3-A20

Oxidative and nitrosative stress in AD[137] can be monitored with 4-hydroxynonenal (4-HNE),[138] 3-nitrotyrosine (3-N-Tyr),[138,139] and protein carbonylation.[140,141] 4-HNE from polyunsaturated fatty acid peroxidation injures mitochondria[142–145] and was elevated in mid and advanced disease and prevented and reversed by P7C3-A20 (Figures S4A and 4A). Tyrosine nitration and protein carbonylation were also increased at both stages and prevented and reversed by P7C3-A20 (Figures S4B–S4D and 4B).

Because oxidative stress compromises the BBB, we tested P7C3-A20 in cultured HBMVECs, the predominant BBB cellular component. Exposure of HBMVECs to hydrogen peroxide (H_2O_2)-induced oxidative stress disrupted NAD^+ homeostasis, which P7C3-A20 dose-dependently mitigated (Figure 4C). This required NAD^+ homeostasis restoration, as it was blocked by FK866 (Figure 4C), a nicotinamide phosphoribosyltransferase inhibitor.[146] P7C3-A20 did not affect NAD^+ homeostasis in unstressed HBMVECs (Figure 4D). Oxidative stress in HBMVECs was also completely prevented by P7C3-A20, as shown by CellROX green assay (Figure 4E). Mitochondrial superoxide levels, measured by MitoSOX Red analysis, were also increased by H_2O_2 and suppressed by P7C3-A20 (Figure 4F).

Because oxidative stress impairs mitochondrial function,[147] we assessed HBMVEC mitochondrial respiration using Seahorse mitochondrial stress tests. Basal oxygen consumption was unchanged by H_2O_2 or P7C3-A20 (Figure 4G). Mitochondrial respiration, mitochondrial spare reserve capacity, and maximal mitochondrial respiration rate were reduced in HBMVECs by H_2O_2 exposure and preserved by P7C3-A20, with FK866

Figure 2. P7C3-A20 treatment of aged symptomatic 5xFAD mice reverses amyloid plaque accumulation and BBB deterioration

(A) Accumulation of pathological amyloid structure plaques in 12-month-old 5xFAD mice is reduced by P7C3-A20 in cerebral cortex and hippocampus, as shown by Thioflavin-S-positive % area. (n = 3–4 females; scale bars, 200 μm).

(B) Aβ aggregation in 12-month-old 5xFAD mice is not affected by P7C3-A20, as shown by quantification of 6E10-postive % area, which was stained in the same sections as used for This staining in (A). (Representative images of 6E10 staining in cerebral cortex; *n* = 4 females; scale bars, 200 μm).

(C) Western blot shows APP, total-tau, and p-tau (Ser^{202}/Thr^{205}) in cerebral cortex of 12-month-old mice (GAPDH protein used as loading control). While p-tau in 5xFAD mice is reduced by P7C3-A20, increased brain APP and total-tau were not affected. (*n* = 4 females, 4 males).

(D) Soluble brain Aβ1–40 and Aβ1–42 levels are elevated in 12-month-old 5xFAD mice and not affected by P7C3-A20. (n = 4–5 females, 3–4 males).

(E) Insoluble brain Aβ1–40 and Aβ1–42 levels are elevated in 12-month-old 5xFAD mice and not affected by P7C3-A20. (*n* = 4 females, 4 males).

(F) Pathologically elevated brain p-tau (Ser^{202}, Thr^{205}) in 12-month-old 5xFAD mice is prevented by P7C3-A20. (*n* = 4 females, 4 males).

(G) Western blot shows elevated plasma p-tau217 in 12-month-old 5xFAD VEH mice, reduced toward normal by P7C3-A20 for 6 months (*n* = 4 females, 3 males).

(H) ELISA shows elevated plasma p-tau217 in 12-month-old 5xFAD VEH mice, reduced by P7C3-A20. (n = 4–5 females, 3–5 males).

(I) Increased open space around blood vessels due to astrocytic endfeet disruption (red arrows) in the cerebral cortex and hippocampus BBB of 12-month-old 5xFAD mice is reversed by P7C3-A20. (*n* = 3 females; scale bars, 1 μm).

(J) Increased infiltration of IgG into brain parenchyma of cerebral cortex and hippocampus in 12-month-old 5xFAD mice is reversed by P7C3-A20. (*n* = 4 females, 4 males; scale bars, 20 μm).

(K) Reduced pericyte coverage (CD 13, red) of blood vessel endothelial cells (CD 31, green) in cortex and hippocampus of 12-month-old 5xFAD mice is reversed by P7C3-A20 treatment. (*n* = 4 females, 3–4 males; scale bars, 20 μm).

(L) Reduced ZO-1 expression in 12-month-old 5xFAD mice is prevented by P7C3-A20. (*n* = 5 females, 5 males).

There are no sex-specific differences in any group. Each dot represents an individual sample. For mouse samples, females are blue and males are red. Error bars are standard error of the mean. $^*p < 0.05$, $^{**}p < 0.01$, $^{***}p < 0.001$, $^{****}p < 0.0001$, one-way ANOVA and Dunnett multiple comparisons against 5xFAD VEH group. See also Figure S2.

CellPress
OPEN ACCESS

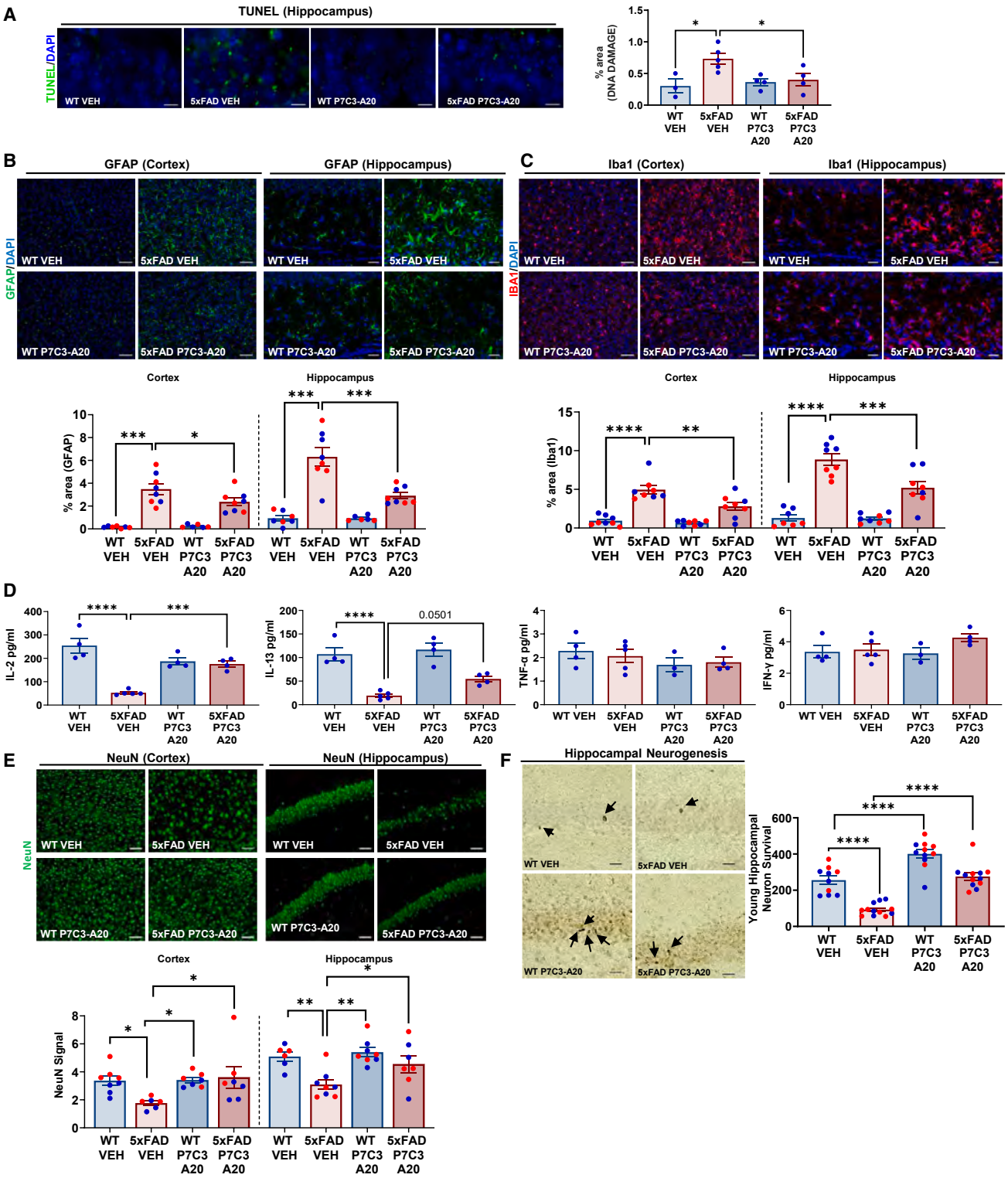

Figure 3. P7C3-A20 treatment of aged symptomatic 5xFAD mice reverses DNA damage, reverses neuroinflammation, and prevents young and mature neuronal cell death

(A) DNA damage in the hippocampus, as measured by TUNEL staining (green signal), is elevated in 12-month-old 5xFAD mice and reversed by P7C3-A20. (Representative CA1 regions; n = 3–5 females; scale bars, 200 μm).

(legend continued on next page)

sensitivity establishing requirement for restoration of NAD^+ homeostasis (Figures 4H–4J).

Disrupted brain NAD^+ homeostasis correlates with disease severity in human and mouse AD

Previous studies reported altered brain NAD^+ homeostasis in aging human brain,[148] but never examined NAD^+ in AD brain. In human AD brain samples (Table S1) exhibiting ~2-fold increases in AD-specific phosphorylated tau at Ser202 and Thr205[149] (Figure S5A), we found 30% reduction in NAD^+/NADH (Figure 5A). In human AD, brain NAD^+ homeostasis disruption correlated with tau pathology (Figures 5B and S5A), protein carbonylation (Figures 5C and S5B), GFAP (Figures 5D and S5C), ZO-1 (Figures 5E and S5D), and NeuN (Figures 5F and S5E). We also observed a strong relationship between human brain NAD^+ homeostasis disruption and PSD-95 (Figures 5G and S5F), which was recapitulated in 5xFAD mice. In advanced-disease 5xFAD mice, brain NAD^+ homeostasis disruption correlated with tau pathology (Figure 5H) and protein carbonylation (Figure 5I), with mid-disease 5xFAD mice showing a similar trend for protein carbonylation (Figure 5J). Advanced-disease 5xFAD mice also showed correlation of brain NAD^+ homeostasis disruption and IL-2 (Figure 5K), IL-13 (Figure 5L), and ZO-1 (Figure 5M). In 5xFAD mice at both stages, disruption of brain NAD^+ homeostasis correlated with impaired cognitive and motor outcomes (Figures 5N–5S).

We further profiled the expression of mRNA for NAD^+-synthesizing and NAD^+-consuming enzymes in human AD and NDAN brains, relative to controls. AD brains showed decreased levels of NAD^+-synthesizing enzymes glutamine-dependent NAD^+ synthetase (*NADSYN1*) and nicotinamide mononucleotide adenylyltransferase 2 (*NMNAT2*), with NDAN levels unchanged (Figure 5T). We observed a trend toward reduced nicotinamide riboside kinase 1 (*NMRK1*) in AD but not NDAN (Figure S5G). Among NAD^+-consuming enzymes, AD brains exhibited increased expression of NAD kinase 2 (*NADK2*), poly (ADP-ribose) polymerase 4 (*PARP4*), and sirtuin 1 (*SIRT1*), with NDAN similar to controls (Figure 5U). Trends toward increased expression of NAD^+-consuming enzymes 5′-nucleotidase cytosolic II (*NT5C2*) and sirtuin 4 (*SIRT4*) were seen in AD but not NDAN (Figure S5G).

P7C3-A20 restores NAD^+ homeostasis and reverses pathology in late-stage mutant tau-driven PS19 mice

To evaluate whether restoring NAD^+ homeostasis could reverse AD-like disease in another model, we tested P7C3-A20 in PS19 mice. PS19 animals overexpress P301S mutant human tau and accumulate hyperphosphorylated, insoluble tau tangles resembling human neurofibrillary tangles, leading to cognitive deficits and neurodegeneration.[150] Treatment with P7C3-A20 began at 11 months of age, a terminal disease stage as these mice typically live only 12 months (Figure S5H). PS19 mice showed significant cognitive impairment in the NOR test (Figure S5I). Animals were randomized to VEH or P7C3-A20, with the designated P7C3-A20 treatment group exhibiting a trend toward greater cognitive impairment before initiation of treatment (Figure S5J). After 15 days, P7C3-A20-treated PS19 mice showed cognitive improvement in the NOR test, reaching discrimination indices comparable to WT VEH controls (Figure S5K). After 30 days, P7C3-A20-treated PS19 mice exhibited significantly higher discrimination index than PS19 VEH mice (Figure S5L), indicating recovery from cognitive impairment.

NAD^+ homeostasis, ZO-1 expression, and protein carbonylation were normalized in PS19 mice by P7C3-A20 (Figures S5M–S5O), and P7C3-A20 produced a trend toward reduced IBA-1 immunoreactivity (Figure S5P), without changing expression of the mutant human tau transgene (Figure S5Q). Phosphorylated tau Ser202/Thr205 was also more abundant in PS19 brain than WT and reduced by P7C3-A20 (Figure S5R). Thus, consistent with findings in amyloid-driven 5xFAD mice, P7C3-A20 reversed functional and molecular disease markers in late-stage, tau-driven PS19 mice without altering genetically driven tau pathology.

Proteomic signatures of P7C3-A20-mediated AD reversal

Proteomic analysis of hippocampi from 12-month-old male and female 5xFAD mice treated daily with P7C3-20 or VEH from 6 to 12 months of age detected 4,483 proteins in females and 4,324 proteins in males (Data S1, tabs 1 and 2). Differentially expressed proteins ([DEPs] defined as proteins with fold change of $\geq \pm 1.25$ and $p \leq 0.05$) are summarized in Data S1, tabs 3–8. Raw and processed data are in Data S1.

Figure 6 shows combined results for sexes, while Figures S6 and S7 show sex-specific results. DEPs were grouped into three comparisons: (1) 5xFAD-VEH vs. WT-VEH (red, upregulated in 5xFAD-VEH; blue, downregulated in 5xFAD-VEH [Figures 6A, S6A, and S7A]), (2) 5xFAD-P7C3-A20 vs. 5xFAD-VEH (red, upregulated in 5xFAD-P7C3-A20; blue, downregulated in 5xFAD-P7C3-A20 [Figures 6B, S6B, and S7B]), and (3) WT-P7C3-A20 vs. WT-VEH (red, upregulated in WT P7C3A20;

(B) GFAP (green signal) in cerebral cortex and hippocampus is elevated in 12-month-old 5xFAD mice and partially reversed by P7C3-A20. (n = 3–4 females, 3–4 males; scale bars, 50 μm).
(C) IBA1 (red signal) in cerebral cortex and hippocampus is elevated in 12-month-old 5xFAD mice and partially reversed by P7C3-A20. (n = 3–4 females, 4 males per group; scale bars, 50 μm).
(D) IL-2 and IL-13 cytokine levels in hippocampus are reduced in 12-month-old 5xFAD mice and reversed toward normal by P7C3-A20. TNF-α and IFN-γ cytokine levels in hippocampus are not altered. (n = 3–5 females).
(E) Mature neuronal survival (NeuN staining) in cerebral cortex and hippocampus is reduced in 12-month-old 5xFAD mice and prevented by P7C3-A20. (n = 3–4 females, 3–4 males; scale bars, 50 μm).
(F) Survival of young BrdU-labeled hippocampal neurons is reduced in 12-month-old 5xFAD mice and restored to normal by P7C3-A20. (n = 5–6 females, 4–6 males; scale bars, 50 μm).
There are no sex-specific differences in any group. Each dot represents an individual sample. For mouse samples, females are blue and males are red. Error bars are standard error of the mean. $^*p < 0.05$, $^{**}p < 0.01$, $^{***}p < 0.001$, $^{****}p < 0.0001$, one-way ANOVA and Dunnett multiple comparisons against 5xFAD VEH group. See also Figure S3.

CellPress
OPEN ACCESS

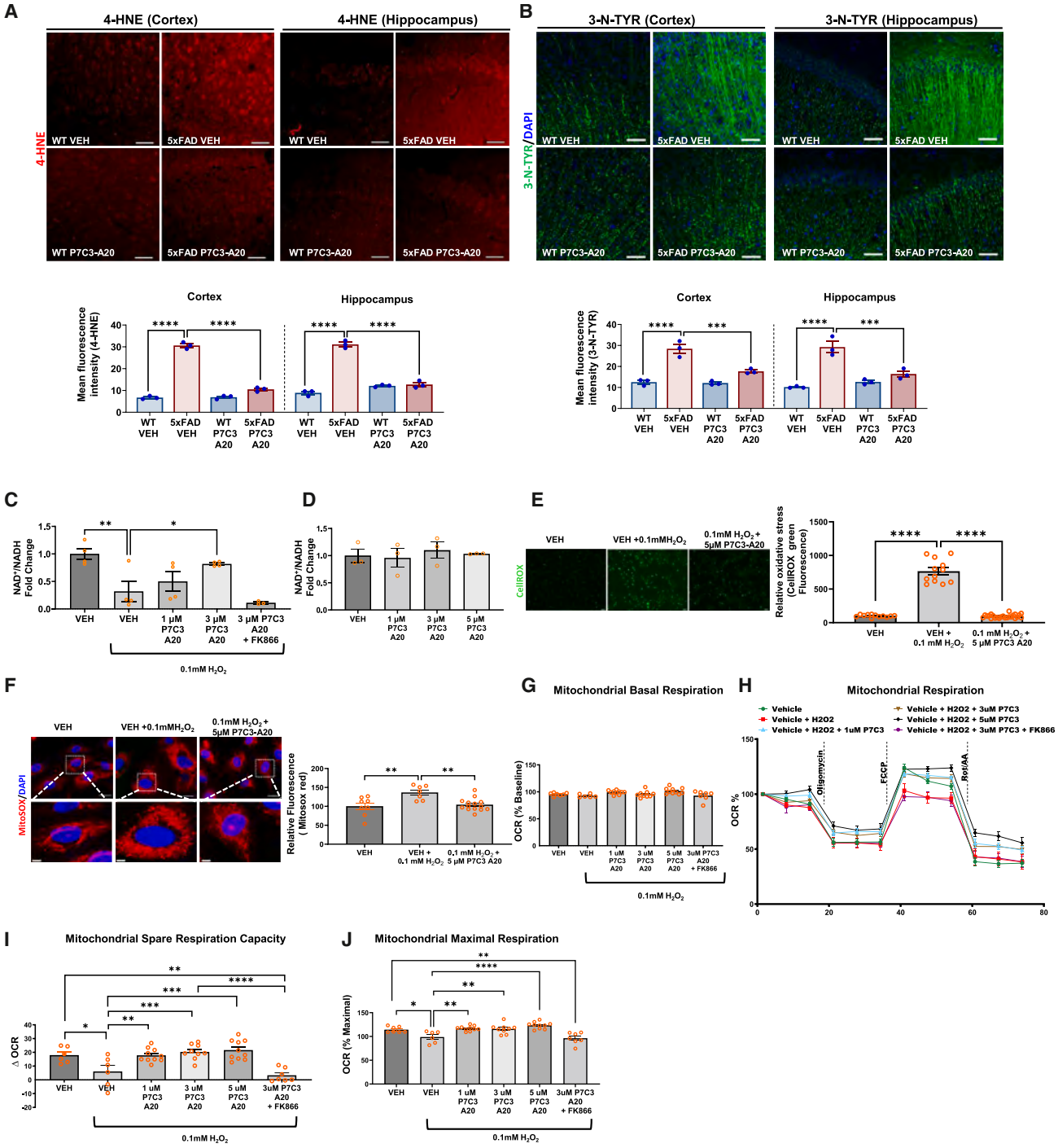

Figure 4. Oxidative stress is reversed by P7C3-A20 in aged symptomatic 5xFAD mice and oxidatively stressed HBMVECs

(A) Elevated lipid peroxidation (4-HNE) in cerebral cortex and hippocampus of 12-month-old 5xFAD mice is reversed by P7C3-A20. (*n* = 3 females; scale bars, 50 μm).

(B) Elevated protein nitration (3-N-Tyr) in cerebral cortex and hippocampus of 12-month-old 5xFAD mice is reversed by P7C3-A20. (*n* = 3 females; scale bars, 50 μm).

(C) Disrupted NAD^+ homeostasis in HBMVECs following exposure to hydrogen peroxide (H_2O_2) is prevented by P7C3-A20, which is blocked by FK866 (n = 3–4 cell culture wells per group).

(D) NAD^+ homeostasis is not altered in naive HBMVECs by P7C3-A20. (*n* = 3 cell culture wells per group).

(legend continued on next page)

blue, downregulated in WT-P7C3-A20 [Figures 6C, S6C, and S7C]).

From comparison 1 (5xFAD-VEH vs. WT-VEH), 174 DEPs (107 in females and 67 in males) were no longer differentially expressed after P7C3-A230 treatment (comparison 2) (Figures S6D and S7D). Combined Gene Ontology (GO) enrichment for the 174 DEPs are in Figure 6D, with sex-specific GO results in Figures S6E and S7E. Kyoto Encyclopedia of Genes and Genomes (KEGG) pathway analysis is in Figure 6E and Reactome pathway analysis is in Figure 6F. Although GO, KEGG, and Reactome analyses showed substantial overlap between sexes, there were also sex-specific representations (Figures S6E–S6G and S7E–S7G) that may reflect sex-specific vulnerabilities to disrupted brain NAD^+ homeostasis.

Brain proteins aberrantly expressed in both human AD and 5xFAD mice and restored to normal in 5xFAD mice by P7C3-A20

To identify brain proteins altered in the same direction in human AD and 5xFAD mice that were also normalized following AD reversal in mice, we compared the 174 DEPs with published human AD brain proteomic databases. We reasoned that such proteins may identify conserved pathways with potential complementary targets for therapeutic AD reversal. Utilizing a composite analysis of 38 published human AD proteomic studies,[151] we found 46 mouse DEPs changing in the same direction in human AD brain (Figure 6G) (29 female [Figure S6L], 17 male [Figure S7L]). Figure 6H displays a heatmap of NeuroPro scores from the composite human analysis, with positive scores indicating proteins elevated across AD stages and negative scores indicating a decrease. These proteins converge on processes central to proteostasis, RNA metabolism, translation, mitochondrial function, lipid and membrane biology, and immune/axon guidance signaling.

Key proteins elevated in human and mouse AD and normalized by AD reversal include bcl-2-associated transcription factor 1 (BCLAF1),[152] complement C1q subcomponent subunit A (C1QA),[153] APP, heterogeneous nuclear ribonucleoprotein U (HNRNPU),[154–156] and FMR2 autosomal homolog 1 (FXR1).[157] Ubiquitin-specific peptidase 10 (USP10), which contributes to early stress granule formation with tau pathology and interacts with sequestome 1 (SQSTM1/p62) to form protective aggresomes,[158–160] was decreased in both human and mouse AD and normalized by AD reversal, while SQSTM1/p62[161] showed the opposite.

With respect to chaperone and aggregation-related proteins, prefoldin subunit 5 (PFDN5), which prevents Aβ fibrillation,[162–164] was decreased in human and mouse AD and normalized by AD reversal. Proteins associated with nucleic acid processing that were increased in human and mouse AD and normalized by AD reversal included peptidylprolyl *cis/trans*-isomerase NIMA-interacting 4 (PIN4),[165–167] 60S ribosomal protein L7A (RPL7A),[168] PSMA6,[169,170] and proteasome 26S subunit non-ATPase 3 (PSMD3).[171]

Related to metabolism, glucose-6-phosphate isomerase 1 (GNPDA1), which catalyzes uridine 5′-diphosphate-N-acetylglucosamine (UDP-GlcNAC) synthesis,[172] a process disrupted in AD,[173–177] was elevated in human and mouse AD and normalized by AD reversal. Related to lipid and peroxisomal metabolism, levels of ATP-binding cassette subfamily D member 3 (ABCD3), which transports fatty acyl-CoAs into peroxisomes for β-oxidation,[178–182] were decreased in human and mouse AD and normalized by AD reversal.

Several proteins associated with mitochondrial function and integrity were decreased in human and mouse AD and normalized by AD reversal, including mitochondrial ribosomal protein S5 (MRPS5),[183,184] Ts translation elongation factor mitochondrial (TSFM),[185–187] fibronectin type 3 and SPRY domain-containing protein 1 (FSD1),[188] AU RNA-binding methylglutaconyl-CoA hydratase (AUH),[189–191] BolA like protein 1 (BOLA1),[192–194] armadillo repeat-containing protein 1 (ARMC1),[195] outer mitochondrial membrane lipid metabolism regulator (OPA3),[196–200] solute carrier family 25 member 42 (SLC25A42),[201] and protein tyrosine phosphatase localized to the mitochondrion 1 (PTPMT1).[202–204]

GO term analyses of these 46 proteins are shown in Figure 6I. Sex-specific GO analyses are displayed in Figures S6J and S7J. Reactome pathway analysis, including upregulated signaling by ROBO receptors,[205–207] are shown in Figure 6J. Sex-specific Reactome analyses are shown in Figures S6K and S7K.

Differentially expressed proteins normalized by AD reversal that reflect concordant transcriptional changes

Proteomic changes do not always parallel transcriptional alterations[208] and instances of concordance can reflect disease-specific regulation at the transcriptional level that could help prioritize biomarkers and therapeutic targets. Thus, we

(E) Increased CellROX Green in HBMVECs following H_2O_2 exposure is prevented by P7C3-A20. (n = 12 cell culture wells per group for VEH and H_2O_2; n = 24 cell culture wells per group for H_2O_2 + P7C3-A20; scale bars, 100 μm).

(F) Increased MitoSOX Red signal in HBMVECs following H_2O_2 exposure is prevented by P7C3-A20 (scale bars, 5 μm). Mitochondrial fragmentation caused by H_2O_2 exposure is also prevented by P7C3-A20 treatment. Area shown in dotted box indicates a higher-magnification image of the indicated region (scale bars, 20 μm). (n = 8 cell culture wells per group for VEH; n = 7 cell culture wells per group for H_2O_2; n = 14 cell culture wells per group for H_2O_2 + P7C3-A20).

(G) Basal mitochondrial respiration rate in HBMVECs is constant across all groups. (n = 6–10 cell culture wells per group).

(H) Mitochondrial respiratory suppression in HBMVECs following H_2O_2 exposure is prevented by P7C3-A20, which is blocked by FK866. (n = 6–10 cell culture wells per group).

(I) Reduced mitochondrial spare reserve capacity in HBMVECs following H_2O_2 exposure is prevented by P7C3-A20, which is blocked by FK866. (n = 6–10 cell culture wells per group).

(J) Reduced maximal mitochondrial respiration rate in HBMVECs following H_2O_2 exposure is prevented by P7C3-A20 treatment, which is blocked by FK866. (n = 6–10 cell culture wells per group).

Each dot represents an individual set of experiments. $^*p < 0.05$, $^{**}p < 0.01$, $^{***}p < 0.001$, $^{****}p < 0.0001$, data were analyzed by one-way ANOVA and Dunnett multiple comparisons against 5xFAD VEH group for mice and H_2O_2 VEH for cells. See also Figure S4.

CellPress
OPEN ACCESS

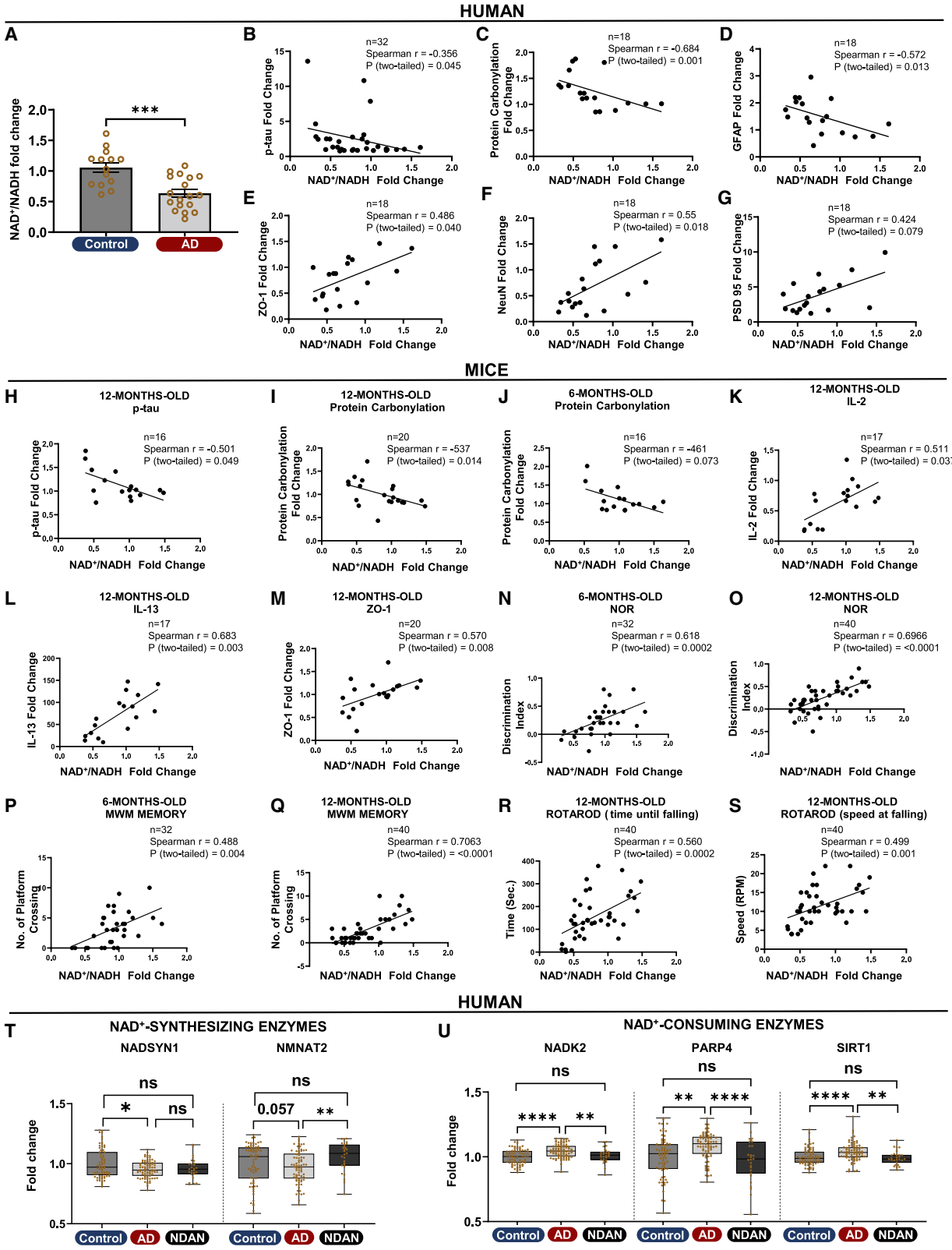

(legend on next page)

examined whether any brain proteins aberrant in both human and mouse AD and normalized by AD reversal showed comparable mRNA changes in human AD brain. We queried the Seattle Alzheimer's Disease Brain Cell Atlas transcriptomic resource, focusing on male and female datasets from the middle temporal gyrus and dorsolateral prefrontal cortex. Seventeen of the 174 DEPs showed concordant proteomic and transcriptomic change in human AD (Figure 6K) (11 in females [Figure S6L] and 6 in males [Figure S7L]). These 17 proteins are enriched in processes governing translation, synaptic structure and vesicle trafficking, endocytosis, and axon guidance. The transcriptional-proteomic concordance strengthens their candidacy as biomarkers and mechanistic mediators for therapeutic strategies aimed at reversing AD.

With respect to the directionality of the concordant changes, across sexes 7 of the 17 proteins were upregulated in both human and mouse AD and normalized by AD reversal: BUB3 mitotic checkpoint protein (BUB3), DExH-box helicase 9 (DHX9), potassium channel tetramerization domain containing 12 (KCTD12), serine/threonine-protein kinase PAK 2 (PAK2), PEST proteolytic signal containing nuclear protein (PCNP), protein tyrosine kinase 2 beta (PTK2B), and ribosomal protein L7a (RPL7A). The remaining 10 were downregulated in both species and normalized by AD reversal: RAN-binding protein 1 (RANBP1), amphiphysin (AMPH), ankyrin-3 (ANK3, also known as ankyrinG), contactin-associated protein 1 (CNTNAP1), cytochrome *c* oxidase subunit B1 (COX6B1), GDNF family receptor alpha 2 (GFRA2), leucyl-tRNA synthetase 2, mitochondrial (LARS2), Ras-like without CAAX 2 (RIT2), secretory carrier membrane protein 5 (SCAMP5), and synaptosome-associated protein 91 (SNAP91). Several of these genes have been previously implicated in AD-related mechanisms, including DHX9,[209–212] PTK2B,[213–216] RPL7A,[217] AMPH,[218] ANK3,[219–222] CNTNAP1,[223] LARS2,[224] and SCAMP5.[225] GO term analyses for the 17 concordant proteomic and transcriptomic changes are in Figure 6L and Reactome analysis is in Figure 6M.

DISCUSSION

AD features a prolonged preclinical phase during which brain resilience is partially preserved, and we identify dysregulation of brain NAD^+ homeostasis as a central mechanism driving loss of that resilience in both human and mouse AD. We also show that NAD^+ dysregulation correlates with disease severity, NDAN individuals exhibit gene expression patterns compatible with preserved brain NAD^+ homeostasis, and pharmacologically

Figure 5. Magnitude of brain NAD^+ homeostatic disruption correlates with the severity of human and mouse AD

(A) NAD^+ homeostasis is disrupted in human AD cerebral cortex, relative to control subjects (n = 14–18 per group, ***$p < 0.001$, unpaired t test). Also see Table S1.

(B) Greater disruption in human brain NAD^+ homeostasis is associated with more p-Tau pathology. Also see Figure S5A and Tables S1 and S2.

(C) Greater disruption in human brain NAD^+ homeostasis is associated with more oxidative damage, as evidenced by protein carbonylation levels. Also see Figure S5B and Table S2.

(D) Greater disruption in human brain NAD^+ homeostasis is associated with more neuroinflammation, as evidenced by GFAP levels. Also see Figure S5C and Table S2.

(E) Greater disruption in human brain NAD^+ homeostasis is associated with more BBB deterioration, as evidenced by ZO-1 levels. Also see Figure S5D and Table S2.

(F) Greater disruption in human brain NAD^+ homeostasis is associated with more neuronal cell loss, as evidenced by NeuN levels. Also see Figure S5E and Table S2.

(G) Greater disruption in human brain NAD^+ homeostasis shows a trend of association with more synaptic loss, as evidenced by PSD-95 levels. Also see Figure S5F and Table S2.

(H) Greater disruption in 12-month-old 5xFAD brain NAD^+ homeostasis is associated with more p-tau pathology.

(I) Greater disruption in 12-month-old 5xFAD brain NAD^+ homeostasis is associated with more oxidative damage, as evidenced by protein carbonylation levels.

(J) Greater disruption in 6-month-old 5xFAD brain NAD^+ homeostasis is associated with more oxidative damage, as evidenced by protein carbonylation levels.

(K) Greater disruption in 12-month-old 5xFAD brain NAD^+ homeostasis is associated with more neuroinflammation, as evidenced by IL-2 levels.

(L) Greater disruption in 12-month-old 5xFAD brain NAD^+ homeostasis is associated with more neuroinflammation, as evidenced by IL-13 levels.

(M) Greater disruption in 12-month-old 5xFAD brain NAD^+ homeostasis is associated with more BBB deterioration, as evidenced by ZO-1 levels.

(N) Greater disruption in 6-month-old 5xFAD brain NAD^+ homeostasis is associated with more greatly impaired memory, as evidence by discrimination index in the NOR test.

(O) Greater disruption in 12-month-old 5xFAD brain NAD^+ homeostasis is associated with more greatly impaired memory, as evidence by discrimination index in the NOR test.

(P) Greater disruption in 6-month-old 5xFAD brain NAD^+ homeostasis is associated with more greatly impaired memory, as evidence by the number of platform crossings in the probe memory test of the Morris water maze.

(Q) Greater disruption in 12-month-old 5xFAD brain NAD^+ homeostasis is associated with more greatly impaired memory, as evidence by the number of platform crossings in the probe memory test of the Morris water maze.

(R) Greater disruption in 12-month-old 5xFAD brain NAD^+ homeostasis is associated with decreased ability to stay on the accelerating rotating rod, as evidenced by time until falling.

(S) Greater disruption in 12-month-old 5xFAD brain NAD^+ homeostasis is associated with decreased ability to stay on the accelerating rotating rod, as evidenced by rotation speed of the rod at falling.

(T) Levels of the NAD^+-synthesizing enzymes glutamine-dependent NAD^+ synthetase (NADSYN1) and nicotinamide mononucleotide adenylyltransferase 2 (NMNAT2) are reduced in human AD cerebral cortex, relative to control subjects, and present at normal levels in NDAN subjects (n = 73 for control, 80 for AD, and 27 for NDAN; *$p < 0.05$, **$p < 0.01$, limma linear regression).

(U) Levels of NAD^+-consuming enzymes NAD kinase 2 (NADK2), poly (ADP-ribose) polymerase 4 (PARP4), and sirtuin 1 (SIRT1) are increased in human AD cerebral cortex, relative to control subjects, and present at normal levels in NDAN subjects (n = 73 for control, 80 for AD, and 27 for NDAN, **$p < 0.01$, ****$p < 0.0001$, limma linear regression).

See also Figure S5.

CellPress
OPEN ACCESS

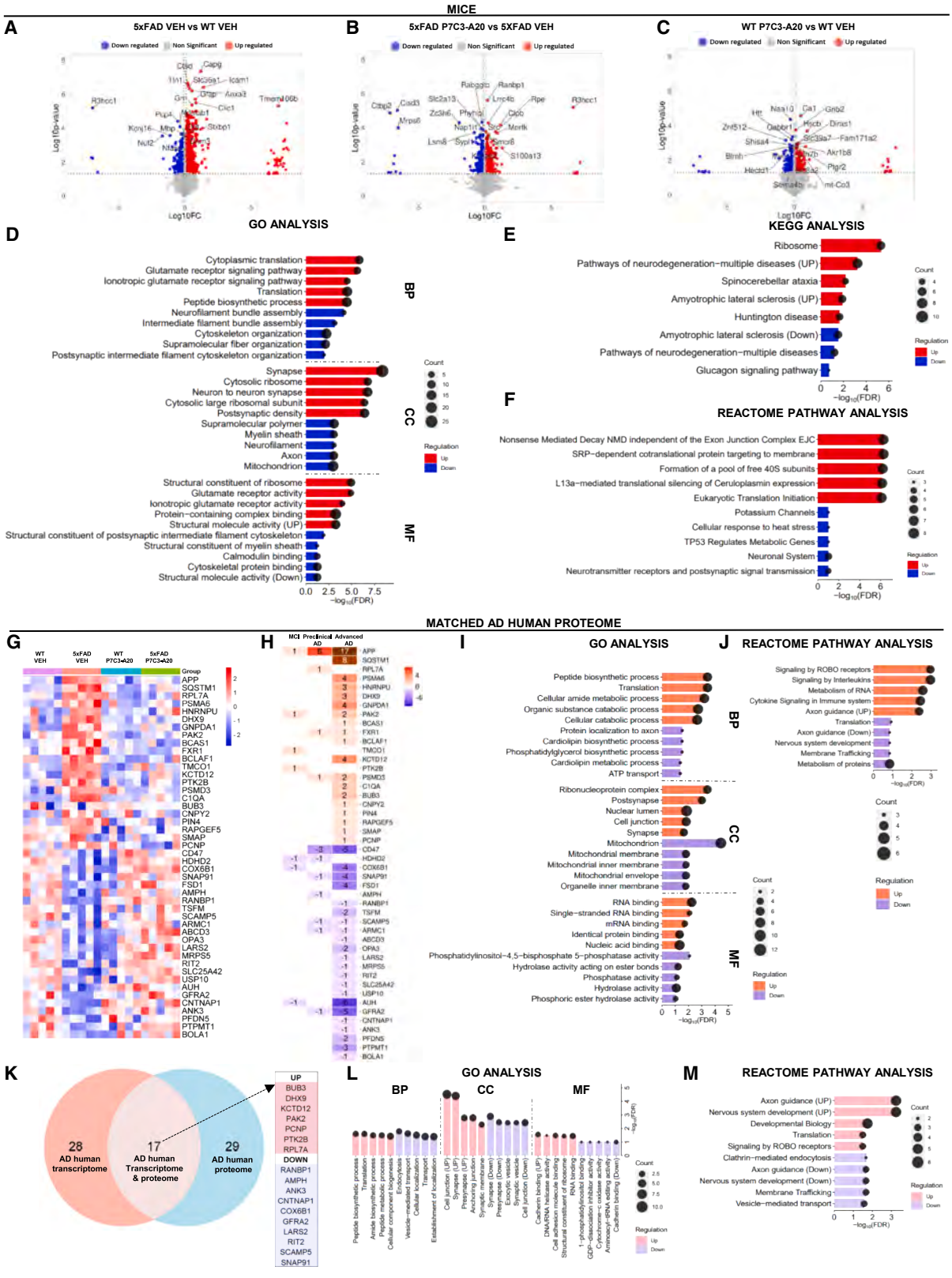

(legend on next page)

normalizing NAD^+ homeostasis with P7C3-A20 restores brain resilience and enables recovery from advanced disease across diverse mouse AD models. Although aging diminishes NAD^+ homeostasis, we found substantially greater NAD^+ dysregulation in mouse and human AD, indicating that the pathophysiological processes of AD amplify this metabolic crisis.

To test the therapeutic implications of restoring NAD^+ homeostasis, we evaluated P7C3-A20 in two complementary rodent AD models: amyloid-driven 5xFAD mice and mutant tau-driven PS19 mice. Prophylactic treatment with P7C3-A20 prevented disease onset in 5xFAD animals. More compellingly, initiating treatment at 6 months of age, when 5xFAD mice already manifest advanced pathology and cognitive deficits, comprehensively restored brain health and function by 12 months. We observed parallel recovery in near-terminal severely symptomatic PS19 mice. Notably, there were no sex-specific differences in treatment response in these models. Together with our previous report of P7C3-A20-mediated reversal of chronic neurodegeneration after traumatic brain injury (TBI),[89] a major risk factor for AD,[226] our results support an emerging paradigm in which diverse forms of advanced neurodegeneration may be amenable to pathological reversal and functional recovery through restoration of brain NAD^+ homeostasis.

Our results challenge the long-held view that AD is intrinsically irreversible and position restoration of brain NAD^+ homeostasis as a potentially transformative therapeutic approach. Restoring NAD^+ homeostasis replenishes a systemic metabolic currency required for multiple interconnected reparative pathways, rather than targeting any single downstream effector. By breaking the escalating energy demand imposed by ongoing cellular damage, restoring NAD^+ homeostasis bolsters resilience against proximate disease drivers like Aβ and tau. Importantly, P7C3-A20 restores physiological NAD^+ homeostasis without exceeding normal ranges, supporting a favorable safety profile.

The emergence of severe neuropsychiatric and cognitive deficits in mid-disease 5xFAD mice before mature neuronal loss indicates that secondary pathologies, such as impaired proteostasis, BBB dysfunction, oxidative stress, neuroinflammation, and reduced neurogenesis, can drive functional decline independently of neuronal cell death. Thus, neuronal loss should be viewed as a late-stage marker of failing brain health rather than the primary proximate cause of early cognitive impairment. Future studies will assess whether P7C3-A20 can also fully restore cognitive function following extensive neuronal cell loss in even more advanced disease stages, building on our previous demonstration of full cognitive recovery after irreversible neuron loss from chronic TBI.[89]

Our demonstration of restoring NAD^+ homeostasis-dependent brain resilience also provides a platform to discover disease-relevant molecular nodes. Through hippocampal proteomic analysis, we identified 46 proteins that were dysregulated concordantly in human and mouse AD and normalized by AD reversal, with many showing matching transcriptional changes. These proteins implicate processes central to proteostasis,

Figure 6. Molecular signature of AD reversal and correlation with human data

(A) Volcano plot of significant DEPs in male and female 5xFAD VEH mice compared to WT VEH (red upregulated, blue downregulated). Top 10 (based on most significant log10 *p* value) are labeled. (n = 5 females, 5 males). Proteins with fold change ± ≥1.25 and *p* value ≤0.05 were considered significant. See also data file Supplementary data 3 & 6.

(B) Volcano plot of significant DEPs in male and female 5xFAD mice treated with P7C3-A20 compared to 5xFAD VEH mice (red upregulated, blue downregulated). Top 10 (based on most significant log10 *p* value) are labeled. (n = 5 females, 5 males). Proteins with fold change ± ≥1.25 and *p* value ≤0.05 were considered significant. See also data file Supplementary data 4 & 7.

(C) Volcano plot of significant DEPs in male and female WT P7C3-A20 mice compared to WT VEH (red upregulated, blue downregulated). Top 10 (based on most significant log10 *p* value) are labeled. (n = 5 females, 5 males). Proteins with fold change ± ≥1.25 and *p* value ≤0.05 were considered significant. See also data file Supplementary data 5 & 8.

(D) Gene Ontology analysis for significant DEPs in 5xFAD VEH mice that were restored to WT VEH levels by P7C3-A20. *y* axis shows enrichment term. *x* axis shows enrichment false discovery rate ([FDR] threshold of ≤0.05). Top five enrichment terms are shown. Terms are categorized as biological processes (BP), cellular components (CC), and molecular functions (MF). Bubble size indicates number of candidates in each pathway (red upregulated, blue downregulated).

(E) KEGG pathway analysis for significant DEPs in 5xFAD VEH mice that were restored to WT VEH levels by P7C3-A20. Top five enriched pathways are shown. Only three pathways were enriched for downregulated proteins, with an FDR of ≤0.1. *y* axis shows pathway term. *x* axis shows enrichment FDR. Bubble size indicates number of candidates in each pathway (red upregulated, blue downregulated).

(F) Top five Reactome pathway analyses of significant DEPs in 5xFAD VEH mice that were restored to WT VEH levels by P7C3-A20. *y* axis shows pathway term. *x* axis shows enrichment FDR (≤0.1). Bubble size indicates number of candidates in each pathway (red upregulated, blue downregulated).

(G) Heatmap shows significant DEPs in male and female 5xFAD VEH mice changing in the same direction as human AD brain that were restored to WT VEH levels in 5xFAD mice by P7C3-A20.

(H) Heatmap shows NeuroPro score. Proteins consistently increased in an AD stage vs. controls have positive score. Proteins consistently decreased in an AD stage vs. controls have negative score.

(I) Gene ontology analysis is shown for significant DEPs in human AD, as represented in Figure 6H. *y* axis shows enrichment term. *x* axis shows enrichment FDR (threshold ≤0.1). Top five enrichment terms are shown. Terms are categorized as BP, CC, and MF. Bubble size indicates number of candidates in each pathway (red upregulated, purple downregulated).

(J) Reactome pathway analysis for significant DEPs in human AD, as represented in Figure 6H. *y* axis shows pathway term. *x* axis shows enrichment FDR (threshold ≤0.1). Top five enrichment terms are shown. Bubble size indicates number of candidates in each pathway (red upregulated, purple downregulated).

(K) Venn diagram showing candidates changing in the same direction in human AD transcriptome, human AD proteome, and 5xFAD VEH mice that were restored to WT VEH levels by P7C3-A20. The 17 proteins changing in the same direction in human AD transcriptome and proteome are marked in the figure.

(L) Gene ontology analysis of the 17 proteins marked in Figure 6K. *y* axis shows enrichment term. *x* axis shows enrichment FDR (threshold ≤0.1). Top five enrichment terms are shown. Terms are categorized BP, CC, and MF. Bubble size indicates number of candidates in each pathway (red upregulated, purple downregulated).

(M) Reactome pathway analysis of the 17 proteins marked in Figure 6K. *y* axis shows pathway term. *x* axis shows enrichment FDR (threshold ≤0.05). Top five enrichment terms are shown. Bubble size indicates number of candidates in each pathway (red upregulated, purple downregulated). See also Figures S6 and S7.

CellPress
OPEN ACCESS

RNA metabolism, translation, mitochondrial function, lipid biology, and immune/axon-guidance signaling. Their concordant dysregulation and restoration nominate them as candidate mediators, biomarkers, or targets for interventions aimed at promoting recovery from advanced AD.

In conclusion, pharmacologic restoration of brain NAD^+ homeostasis reinstated brain resilience, reversed advanced AD pathology, and restored cognitive function across diverse preclinical models, arguing against the deterministic view of AD irreversibility and providing a mechanistic foundation for developing therapies targeting functional recovery from AD.

Limitations of the study

Postmortem human samples reflect end-stage disease and not causality. Though concordant signals across NDAN (human), AD (human), and P7C3-A20-rescue (mice) suggest that impaired NAD^+ homeostasis contributes to AD, we note reliance on genetic mouse models, while most AD is sporadic. We propose that multiple forms of escalating cellular damage synergistically drive chronic, unsustainable demand for repair that dysregulated NAD^+ homeostasis and acknowledge that a single specific driver of NAD^+ homeostasis disruption has not been resolved.

RESOURCE AVAILABILITY

Lead contact

Further information and requests for resources and reagents should be directed to and will be fulfilled by the lead contact, Andrew A. Pieper (andrew.pieper@case.edu).

Materials availability

This study did not generate new unique reagents.

Data and code availability

- All data are available upon reasonable request to the lead contact, Andrew A. Pieper (andrew.pieper@case.edu).
- No custom code was generated in this study.
- Full datasets referred to in the manuscript are available at https://zenodo.org/records/17455622.
- Any additional information required to reanalyze the data reported in this work paper is available from the lead contact upon request.

ACKNOWLEDGMENTS

A.A.P. was supported by The Valour Foundation, the Wichita Foundation, and Department of Veterans Affairs Merit Award I01BX005976 and is the Rebecca E. Barchas, MD, DLFAPA, Professor in Translational Psychiatry of Case Western Reserve University and the Morley-Mather Chair in Neuropsychiatry of University Hospitals. We also acknowledge support from the American Heart Association and Paul Allen Foundation Initiative in Brain Health and Cognitive Impairment (19PABH134580006; A.A.P. and B.D.P.), NIH/NIA R01AG071512 (A.A.P. and B.D.P.), NIH/NIA RO1AG066707 (A.A.P. and F.C.), NIH/NIA 1U01AG073323 (A.A.P.), the Louis Stokes VA Medical Center resources and facilities (A.A.P. and D.E.K.), an anonymous donor (A.A.P.), NIH/NIA 1R21AG073684-01 (B.D.P.), the Catalyst Award from Johns Hopkins University (B.D.P.). NIH/NINDS KO8NS105916 (J.E.R.), NIH/NIA 1RO1AGO75802 (J.E.R.), the Alzheimer's Association (J.E.R.), the Rainwater Charitable Foundation (J.E.R.), resources and expertise of the institutionally supported UTSW Preclinical Pharmacology Core in evaluating P7C3-A20 levels, NIH AGO83811 (X.Z.), NIH AG056363 (X.Z.), NIH AG049479 (X.Z.), NIA/NIH UO1AG073323 (F.C.), NIA/NIH R21AGO83003 (F.C.), NIA/NIH RO1AGO76448 (F.C.), NIA/NIH RO1AGO84250 (F.C.), NIA/NIH RF1AGO82211 (F.C.), NIH/NINDS RF1NS133812 (F.C.), Alzheimer's Association (ALZDISCOVERY-1051936 [F.C.]), NIH P30AG072977 (T.G.), NIH R01AG062566 (T.G.), NIH R56AG075600 (T.G.), Seoul National University New Faculty Startup Fund (370C-20220110 [M.-K.S.]), Seoul National University Creative-Pioneering Researchers Program (M.-K.S.), National Research Foundation of Korea (RS-2023-00209597 [M.-K.S.]), donors of Alzheimer's Disease Research, a program of BrightFocus Foundation (A2019551F [M.-K.S.]), NIH/NIA 1R01AG067741-01 (D.E.K. and J.-A.W.), NIH/NINDS 1R01NS122218-A1 (D.E.K. and J.-A.W.), Alzheimer's Disease Translational Data Science Training Program NIH T32AG071474 (S.B. and E.M.), DOD Peer-Reviewed Alzheimer's Research Program (PRARP) Award AZ210092 (W81XWH-22-1-0129 [E.V.-R.]), NIH/NIA F30AG076183 (P.S.S.), NIH/NINDS T32NS077888 (P.S.S.), Case Western Medical Scientist Training program NIH T32 GM007250 (P.S.S. and S.B.), NIH/NIA F99AG083111 (Y.K.), Translational Research Shared Resource of the Case Comprehensive Cancer Center (NIH/NCI P30 CA43703) for Seahorse analyzer, CWRU Youth Engaged in Science (YES)/Scientific Enrichment Opportunity (SEO) Program via NCI R25 CA221718 (S.R. and H.F.), and biorender.com to design schematic figures and graphical abstract. Views expressed are those of the authors and do not reflect the position or policy of the Department of Veterans Affairs of the United States government.

AUTHOR CONTRIBUTIONS

K.C., E.V.-R., N.S.W., J.E.R., J.-A.W., D.E.K., B.D.P., and A.A.P designed the experiments and wrote the manuscript with input from authors. All authors reviewed the manuscript. K.C., E.V.-R., S.J.T., M-K.S., Y.Y., M.D., S.C., M.Y., X.W., P.S.S., E.M., Z.B., S.G. Corella, S.B., S.G. Caradonna, Y.K., K.F., C.J.C-P., S.R., H. Fang, A.A.C.-P., T.T., H. Fujioka., N.S.W., J.E.R., J-A.A.W., D.E.K., B.D.P., and A.A.P conducted experimental work. S.C., S.J.T., and B.D.P. collaborated on oxidative damage and PS19 disease reversal studies. M.Y. and J.E.R. analyzed NDAN brain tissue. X.Q., J-A.W., and D.E.K. conducted electrophysiology. Human brain samples were provided by T.G. and M.F. (Northwestern University) and X.Z. (Cleveland Alzheimer's Disease Research Center P30AG072959). H. Fujioka collaborated on electron microscopy. N.S.W. collaborated on pharmacokinetic studies of P7C3 compounds. B.M.W. directed statistical data analysis. A.A.P. is guarantor of this work, has full access to all data, and takes responsibility for data integrity and accuracy of data analysis.

DECLARATION OF INTERESTS

A.A.P., K.C., E.V.-R., M.-K.S., and M.D. hold related patents. A.A.P. is a cofounder of Glengary Brain Health, Inc.

STAR★METHODS

Detailed methods are provided in the online version of this paper and include the following:

- KEY RESOURCES TABLE
- EXPERIMENTAL ANIMALS, CELLS, AND HUMAN SUBJECTS DETAILS
  - Cell culture
  - Animals
  - Human samples
- METHOD DETAILS
  - P7C3-A20 pharmacokinetics and binding analysis
  - *In vivo* animal treatment
  - Behavioral analysis
  - Sample harvesting
  - NAD^+/NADH measurement
  - Brain homogenate preparation for soluble/insoluble Aβ and p-tau measurement
  - Soluble insoluble Aβ 1–40/1-42 analysis
  - Western blotting
  - Immunohistochemistry
  - Cytokine analysis

- Hippocampal neuronal survival
- Blood brain barrier integrity analysis
- Reactive oxygen species detection through CellROX green and MitoSOX red
- Image acquisition and quantification of immunohistochemistry
- Measurement of mitochondrial respiration
- Protein carbonylation
- *Ex vivo* electrophysiology study
- Label-free quantitative proteomic analysis

- QUANTIFICATION AND STATISTICAL ANALYSIS

SUPPLEMENTAL INFORMATION

Supplemental information can be found online at https://doi.org/10.1016/j.xcrm.2025.102535.

Received: June 23, 2025
Revised: September 22, 2025
Accepted: November 26, 2025
Published: December 22, 2025

REFERENCES

1. Alzheimer's Disease International Dementia Statistics. https://www.alzint.org/about/dementia-facts-figures.
2. (2023). 2023 Alzheimer's disease facts and figures. Alz. & Dement *19*, 1598–1695. https://doi.org/10.1002/alz.13016.
3. Prados, M.J., Liu, Y., Jun, H., Lam, J., and Mattke, S. (2022). Projecting the long-term societal value of a disease-modifying treatment for Alzheimer's disease in the United States. Alzheimer's Dement. *18*, 142–151. https://doi.org/10.1002/alz.12578.
4. Haass, C., and Selkoe, D.J. (2007). Soluble protein oligomers in neurodegeneration: lessons from the Alzheimer's amyloid β-peptide. Nat. Rev. Mol. Cell Biol. *8*, 101–112. https://doi.org/10.1038/nrm2101.
5. Mucke, L., and Selkoe, D.J. (2012). Neurotoxicity of amyloid-protein: synaptic and network dysfunction. Cold Spring Harb. Perspect. Med. *2*, a006338. https://doi.org/10.1101/cshperspect.a006338.
6. Ackley, S.F., Zimmerman, S.C., Brenowitz, W.D., Tchetgen Tchetgen, E.J., Gold, A.L., Manly, J.J., Mayeda, E.R., Filshtein, T.J., Power, M.C., Elahi, F.M., et al. (2021). Effect of reductions in amyloid levels on cognitive change in randomized trials: instrumental variable meta-analysis. BMJ *372*, n156. https://doi.org/10.1136/bmj.n156.
7. Rabinovici, G.D. (2021). Controversy and progress in Alzheimer's disease — FDA approval of aducanumab. N. Engl. J. Med. *385*, 771–774. https://doi.org/10.1056/NEJMp2111320.
8. Sims, J.R., Zimmer, J.A., Evans, C.D., Lu, M., Ardayfio, P., Sparks, J., Wessels, A.M., Shcherbinin, S., Wang, H., Monkul Nery, E.S., et al. (2023). Donanemab in early symptomatic Alzheimer disease. JAMA *330*, 512–527. https://doi.org/10.1001/jama.2023.13239.
9. Van Dyck, C.H., Swanson, C.J., Aisen, P., Bateman, R.J., Chen, C., Gee, M., Kanekiyo, M., Li, D., Reyderman, L., Cohen, S., et al. (2023). Lecanemab in early Alzheimer's disease. N. Engl. J. Med. *388*, 9–21. https://doi.org/10.1056/NEJMoa2212948.
10. Gilman, S., Koller, M., Black, R.S., Jenkins, L., Griffith, S.G., Fox, N.C., Eisner, L., Kirby, L., Rovira, M.B., Forette, F., et al. (2005). Clinical effects of Aβ immunization (AN1792) in patients with AD in an interrupted trial. Neurology *64*, 1553–1562. https://doi.org/10.1212/01.Wnl.0000159740.16984.3c.
11. Sperling, R.A., Jack, C.R., Black, S.E., Frosch, M.P., Greenberg, S.M., Hyman, B.T., Scheltens, P., Carrillo, M.C., Thies, W., Bednar, M.M., et al. (2011). Amyloid-related imaging abnormalities in amyloid-modifying therapeutic trials: Recommendations from the Alzheimer's Association Research Roundtable Workgroup. Alzheimer's Dement. *7*, 367–385. https://doi.org/10.1016/j.jalz.2011.05.2351.
12. Carlson, C., Siemers, E., Hake, A., Case, M., Hayduk, R., Suhy, J., Oh, J., and Barakos, J. (2016). Amyloid-related imaging abnormalities from trials of solanezumab for Alzheimer's disease. Alzheimer's Dement. *2*, 75–85. https://doi.org/10.1016/j.dadm.2016.02.004.
13. Knopman, D.S., Jones, D.T., and Greicius, M.D. (2021). Failure to demonstrate efficacy of aducanumab: An analysis of the EMERGE and ENGAGE trials as reported by Biogen, December 2019. Alzheimer's Dement. *17*, 696–701. https://doi.org/10.1002/alz.12213.
14. Salloway, S., Chalkias, S., Barkhof, F., Burkett, P., Barakos, J., Purcell, D., Suhy, J., Forrestal, F., Tian, Y., Umans, K., et al. (2022). Amyloid-Related imaging abnormalities in 2 phase 3 studies evaluating aducanumab in patients with early Alzheimer disease. JAMA Neurol. *79*, 13–21. https://doi.org/10.1001/jamaneurol.2021.4161.
15. Ebell, M.H., and Barry, H.C. (2022). Why physicians should not prescribe aducanumab for Alzheimer disease. Am. Fam. Phys. *105*, 353–354.
16. Travis, J. (2023). Latest Alzheimer's antibody is 'not a miracle drug. Science *380*, 571. https://doi.org/10.1126/science.adi6515.
17. Bateman, R.J., Smith, J., Donohue, M.C., Delmar, P., Abbas, R., Salloway, S., Wojtowicz, J., Blennow, K., Bittner, T., Black, S.E., et al. (2023). Two phase 3 trials of gantenerumab in early Alzheimer's disease. N. Engl. J. Med. *389*, 1862–1876. https://doi.org/10.1056/NEJMoa2304430.
18. Kepp, K.P., Sensi, S.L., Johnsen, K.B., Barrio, J.R., Høilund-Carlsen, P.F., Neve, R.L., Alavi, A., Herrup, K., Perry, G., Robakis, N.K., et al. (2023). The anti-amyloid monoclonal antibody Lecanemab: 16 cautionary notes. J. Alzheimer's Dis. *94*, 497–507. https://doi.org/10.3233/JAD-230099.
19. Daly, T., Herrup, K., and Espay, A.J. (2024). An ethical argument for ending human trials of amyloid-lowering therapies in Alzheimer's disease. AJOB Neurosci. *15*, 80–81. https://doi.org/10.1080/21507740.2022.2129858.
20. Herrup, K. (2022). Fallacies in neuroscience: the Alzheimer's edition. eNeuro *9*, ENEURO.0530-21.2021. https://doi.org/10.1523/ENEURO.0530-21.2021.
21. Sloane, J.A., Pietropaolo, M.F., Rosene, D.L., Moss, M.B., Peters, A., Kemper, T., and Abraham, C.R. (1997). Lack of correlation between plaque burden and cognition in the aged monkey. Acta Neuropathol. *94*, 471–478. https://doi.org/10.1007/s004010050735.
22. Schmitt, F.A., Davis, D.G., Wekstein, D.R., Smith, C.D., Ashford, J.W., and Markesbery, W.R. (2000). "Preclinical" AD revisited: neuropathology of cognitively normal older adults. Neurology *55*, 370–376. https://doi.org/10.1212/wnl.55.3.370.
23. Bennett, D.A., Schneider, J.A., Arvanitakis, Z., Kelly, J.F., Aggarwal, N.T., Shah, R.C., and Wilson, R.S. (2006). Neuropathology of older persons without cognitive impairment from two community-based studies. Neurology *66*, 1837–1844. https://doi.org/10.1212/01.wnl.0000219668.47116.e6.
24. Price, J.L., McKeel, D.W., Buckles, V.D., Roe, C.M., Xiong, C., Grundman, M., Hansen, L.A., Petersen, R.C., Parisi, J.E., Dickson, D.W., et al. (2009). Neuropathology of nondemented aging: Presumptive evidence for preclinical Alzheimer disease. Neurobiol. Aging *30*, 1026–1036. https://doi.org/10.1016/j.neurobiolaging.2009.04.002.
25. Moore, B.D., Chakrabarty, P., Levites, Y., Kukar, T.L., Baine, A.-M., Moroni, T., Ladd, T.B., Das, P., Dickson, D.W., and Golde, T.E. (2012). Overlapping profiles of Abeta peptides in the Alzheimer's disease and pathological aging brains. Alzheimers Res. Ther. *4*, 18. https://doi.org/10.1186/alzrt121.
26. Erten-Lyons, D., Woltjer, R.L., Dodge, H., Nixon, R., Vorobik, R., Calvert, J.F., Leahy, M., Montine, T., and Kaye, J. (2009). Factors associated with resistance to dementia despite high Alzheimer disease pathology. Neurology *72*, 354–360. https://doi.org/10.1212/01.wnl.0000341273.18141.64.

27. Briley, D., Ghirardi, V., Woltjer, R., Renck, A., Zolochevska, O., Taglialatela, G., and Micci, M.-A. (2016). Preserved neurogenesis in non-demented individuals with AD neuropathology. Sci. Rep. *6*, 27812. https://doi.org/10.1038/srep27812.

28. Green, K.N., Steffan, J.S., Martinez-Coria, H., Sun, X., Schreiber, S.S., Thompson, L.M., and LaFerla, F.M. (2008). Nicotinamide restores cognition in Alzheimer's disease transgenic mice via a mechanism involving sirtuin inhibition and selective reduction of THR231-Phosphotau. J. Neurosci. *28*, 11500–11510. https://doi.org/10.1523/JNEUROSCI.3203-08.2008.

29. Gong, B., Pan, Y., Vempati, P., Zhao, W., Knable, L., Ho, L., Sauve, A.A., Pasinetti, G.M., Wang, J., Sastre, M., and Ono, K. (2013). Nicotinamide riboside restores cognition through an upregulation of proliferator-activated receptor-γ coactivator 1α regulated β-secretase 1 degradation and mitochondrial gene expression in Alzheimer's mouse models. Neurobiol. Aging *34*, 1581–1588. https://doi.org/10.1016/j.neurobiolaging.2012.12.005.

30. Liu, D., Pitta, M., Jiang, H., Lee, J.-H., Zhang, G., Chen, X., Kawamoto, E.M., and Mattson, M.P. (2013). Nicotinamide forestalls pathology and cognitive decline in Alzheimer mice: evidence for improved neuronal bioenergetics and autophagy procession. Neurobiol. Aging *34*, 1564–1580. https://doi.org/10.1016/j.neurobiolaging.2012.11.020.

31. Bayrakdar, E.T., Uyanikgil, Y., Kanit, L., Koylu, E., and Yalcin, A. (2013). Nicotinamide treatment reduces the levels of oxidative stress, apoptosis, and PARP-1 activity in Aβ(1–42)-induced rat model of Alzheimer's disease. Free Rad. Res. *48*, 146–158. https://doi.org/10.3109/10715762.2013.857018.

32. Long, A.N., Owens, K., Schlappal, A.E., Kristian, T., Fishman, P.S., and Schuh, R.A. (2015). Effect of nicotinamide mononucleotide on brain mitochondrial respiratory deficits in an Alzheimer's disease-relevant murine model. BMC Neurol. *15*, 19. https://doi.org/10.1186/s12883-015-0272-x.

33. Wang, X., Hu, X., Yang, Y., Takata, T., and Sakurai, T. (2016). Nicotinamide mononucleotide protects against β-amyloid oligomer-induced cognitive impairment and neuronal death. Brain Res. *1643*, 1–9. https://doi.org/10.1016/j.brainres.2016.04.060.

34. Hou, Y., Wei, Y., Lautrup, S., Yang, B., Wang, Y., Cordonnier, S., Mattson, M.P., Croteau, D.L., and Bohr, V.A. (2021). NAD^+ supplementation reduces neuroinflammation and cell senescence in a transgenic mouse model of Alzheimer's disease via cGAS–STING. Proc. Natl. Acad. Sci. USA *118*, e2011226118. https://doi.org/10.1073/pnas.2011226118.

35. Hou, Y., Lautrup, S., Cordonnier, S., Wang, Y., Croteau, D.L., Zavala, E., Zhang, Y., Moritoh, K., O'Connell, J.F., Baptiste, B.A., et al. (2018). NAD^+ supplementation normalizes key Alzheimer's features and DNA damage responses in a new AD mouse model with introduced DNA repair deficiency. Proc. Natl. Acad. Sci. USA *115*, E1876–E1885. https://doi.org/10.1073/pnas.1718819115.

36. Vakilinezhad, M.A., Amini, A., Akbari Javar, H., Baha'addini Beigi Zarandi, B.F., Montaseri, H., and Dinarvand, R. (2018). Nicotinamide loaded functionalized solid lipid nanoparticles improves cognition in Alzheimer's disease animal model by reducing Tau hyperphosphorylation. Daru *26*, 165–177. https://doi.org/10.1007/s40199-018-0221-5.

37. Xie, X., Gao, Y., Zeng, M., Wang, Y., Wei, T.-F., Lu, Y.-B., and Zhang, W.-P. (2019). Nicotinamide ribose ameliorates cognitive impairment of aged and Alzheimer's disease model mice. Metab. Brain Dis. *34*, 353–366. https://doi.org/10.1007/s11011-018-0346-8.

38. Dong, Y., and Brewer, G.J. (2019). Global metabolic shifts in age and Alzheimer's disease mouse brains pivot at NAD^+/NADH redox sites. J. Alz. Dis. *71*, 119–140. https://doi.org/10.3233/JAD-190408.

39. Xiong, X., Hou, J., Zheng, Y., Jiang, T., Zhao, X., Cai, J., Huang, J., He, H., Xu, J., Qian, S., et al. (2024). NAD+-boosting agent nicotinamide mononucleotide potently improves mitochondrial stress response in Alzheimer's disease via ATF4-dependent mitochondrial UPR. Cell Death Dis. *15*, 744. https://doi.org/10.1038/s41419-024-07062-1.

40. Olesen, U.H., Hastrup, N., and Sehested, M. (2011). Expression patterns of nicotinamide phosphoribosyltransferase and nicotinic acid phosphoribosyltransferase in human malignant lymphomas. APMIS *119*, 296–303. https://doi.org/10.1111/j.1600-0463.2011.02733.x.

41. Li, D., Chen, N.-N., Cao, J.-M., Sun, W.-P., Zhou, Y.-M., Li, C.-Y., and Wang, X.-X. (2014). BRCA1 as a nicotinamide adenine dinucleotide (NAD)-dependent metabolic switch in ovarian cancer. Cell Cycle *13*, 2564–2571. https://doi.org/10.4161/15384101.2015.942208.

42. Chini, C.C.S., Guerrico, A.M.G., Nin, V., Camacho-Pereira, J., Escande, C., Barbosa, M.T., and Chini, E.N. (2014). Targeting of NAD metabolism in pancreatic cancer cells: Potential novel therapy for pancreatic tumors. Clin. Cancer Res. *20*, 120–130. https://doi.org/10.1158/1078-0432.CCR-13-0150.

43. Vora, M., Ansari, J., Shanti, R.M., Veillon, D., Cotelingam, J., Coppola, D., and Shackelford, R.E. (2016). Increased nicotinamide phosphoribosyltransferase in rhabdomyosarcomas and leiomyosarcomas compared to skeletal and smooth muscle tissue. Anticancer Res. *36*, 503–507. https://doi.org/10.21873/anticanres.13282.

44. Neubauer, K., Misa, I.B., Diakowska, D., Kapturkiewicz, B., Gamian, A., and Krzystek-Korpacka, M. (2015). Nampt/PBEF/visfatin upregulation in colorectal tumors, mirrored in normal tissue and whole blood of colorectal cancer patients, is associated with metastasis, hypoxia, IL1β, and anemia. BioMed Res. Int. *2015*, 523930. https://doi.org/10.1155/2015/523930.

45. H, Q., Zhuang, Z.-N., Li, H., Tian, T., Lu, Y.-X., Fan, Z.-Q., Zhou, H.-J., Mo, H.-Y., Sheng, H., Chiao, P.J., and Xu, R.X. (2016). Regulation of the Nampt-mediated NAD salvage pathway and its therapeutic implications in pancreatic cancer. Cancer Lett. *379*, 1–11. https://doi.org/10.1016/j.canlet.2016.05.024.

46. Gujar, A.D., Le, S., Mao, D.D., Dadey, D.Y.A., Turski, A., Sasaki, Y., Aum, D., Luo, J., Dahiya, S., Yuan, L., et al. (2016). An NAD^+ -dependent transcriptional program governs self-renewal and radiation resistance in glioblastoma. Proc. Natl. Acad. Sci. USA *113*, E8247–E8256. https://doi.org/10.1073/pnas.1610921114.

47. Shackelford, R.E., Abdulsattar, J., Wei, E.X., Cotelingam, J., Coppola, D., and Herrera, G.A. (2017). Increased nicotinamide phosphoribosyltransferase and Cystathionine-B-Synthase in renal oncocytomas, renal urothelial carcinoma, and renal clear cell carcinoma. Anticancer Res. *37*, 3423–3427. https://doi.org/10.21873/anticanres.11709.

48. Yaku, K., Okabe, K., Hikosaka, K., and Nakagawa, T. (2018). NAD Metabolism in Cancer Therapeutics. Front. Oncol. *8*, 622. https://doi.org/10.3389/fonc.2018.00622.

49. Nacarelli, T., Lau, L., Fukumoto, T., Zundell, J., Fatkhutdinov, N., Wu, S., Aird, K.M., Iwasaki, O., Kossenkov, A.V., Schultz, D., et al. (2019). NAD+ metabolism governs the proinflammatory senescence-associated secretome. Nat. Cell Biol. *21*, 397–407. https://doi.org/10.1038/s41556-019-0287-4.

50. Maric, T., Bazhin, A., Khodakivskyi, P., Mikhaylov, G., Solodnikova, E., Yevtodiyenko, A., Giordano Attianese, G.M.P., Coukos, G., Irving, M., Joffraud, M., et al. (2023). A bioluminescent-based probe for in vivo non-invasive monitoring of nicotinamide riboside uptake reveals a link between metastasis and NAD^+ metabolism. Biosens. Bioelectron. *220*, 114826. https://doi.org/10.1016/j.bios.2022.114826.

51. Shin, M.-K., Vázquez-Rosa, E., Koh, Y., Dhar, M., Chaubey, K., Cintrón-Pérez, C.J., Barker, S., Miller, E., Franke, K., Noterman, M.F., et al. (2021). Reducing acetylated tau is neuroprotective in brain injury. Cell *184*, 2715–2732.e23. https://doi.org/10.1016/j.cell.2021.03.032.

52. Wang, G., Han, T., Nijhawan, D., Theodoropoulos, P., Naidoo, J., Yadavalli, S., Mirzaei, H., Pieper, A.A., Ready, J.M., and McKnight, S.L. (2014). P7C3 neuroprotective chemicals function by activating the rate-limiting enzyme in NAD salvage. Cell *158*, 1324–1334. https://doi.org/10.1016/j.cell.2014.07.040.

53. Tur, J., Badole, S.L., Manickam, R., Chapalamadugu, K.C., Xuan, W., Guida, W., Crews, J.J., Bisht, K.S., and Tipparaju, S.M. (2022).

Cardioprotective effects of 1-(3,6-Dibromo-carbazol-9-yl)-3-Phenylamino-Propan-2-OL in diabetic hearts via nicotinamide phosphoribosyltransferase activation. J. Pharmacol. Exp. Ther. *382*, 233–245. https://doi.org/10.1124/jpet.122.001122.

54. Hua, X., Sun, D.Y., Zhang, W.J., Fu, J.T., Tong, J., Sun, S.J., Zeng, F.Y., Ouyang, S.X., Wang, S.N., , et al.Zhang, G.Y. (2021). P7C3-A20 alleviates fatty liver by shaping gut microbiota and inducing FGF21/FGF1, via the AMP-activated protein kinase/CREB regulated transcription coactivator 2 pathway. Br. J. Pharmacol. *178*, 2111–2130. https://doi.org/10.1111/bph.15008.

55. Duan, F.-X., Shi, Y.-J., Chen, J., Ding, S.-Q., Wang, F.-C., Tang, J., Wang, R., Shen, L., Xi, J., Qi, Q., et al. (2019). Neuroprotective effects of P7C3 against spinal cord injury in rats. Exp. Biol. Med. *244*, 1680–1687. https://doi.org/10.1177/1535370219888620.

56. LoCoco, P.M., Risinger, A.L., Smith, H.R., Chavera, T.S., Berg, K.A., and Clarke, W.P. (2017). Pharmacological augmentation of nicotinamide phosphoribosyltransferase (NAMPT) protects against paclitaxel-induced peripheral neuropathy. eLife *6*, e29626. https://doi.org/10.7554/eLife.29626.

57. Sasmita, A.O., Ong, E.C., Nazarenko, T., Mao, S., Komarek, L., Thalmann, M., Hantakova, V., Spieth, L., Berghoff, S.A., Barr, H.J., et al. (2025). Parental origin of transgene modulates amyloid-β plaque burden in the 5xFAD mouse model of Alzheimer's disease. Neuron *113*, 838–846.e4. https://doi.org/10.1016/J.NEURON.2024.12.025.

58. Oakley, H., Cole, S.L., Logan, S., Maus, E., Shao, P., Craft, J., Guillozet-Bongaarts, A., Ohno, M., Disterhoft, J., Van Eldik, L., et al. (2006). Intraneuronal β-amyloid aggregates, neurodegeneration, and neuron loss in transgenic mice with five familial Alzheimer's disease mutations: potential factors in amyloid plaque formation. J. Neurosci. *26*, 10129–10140. https://doi.org/10.1523/JNEUROSCI.1202-06.2006.

59. Kanno, T., Tsuchiya, A., and Nishizaki, T. (2014). Hyperphosphorylation of Tau at Ser396 occurs in the much earlier stage than appearance of learning and memory disorders in 5XFAD mice. Behav. Brain Res. *274*, 302–306. https://doi.org/10.1016/j.bbr.2014.08.034.

60. Melone, M.A.B., Dato, C., Paladino, S., Coppola, C., Trebini, C., Giordana, M.T., and Perrone, L. (2018). Verapamil Inhibits Ser202/Thr205 Phosphorylation of Tau by blocking TXNIP/ROS/p38 MAPK pathway. Pharm. Res. *35*, 44. https://doi.org/10.1007/s11095-017-2276-2.

61. Shen, Y., Zhang, T., Zhang, Y., Wang, Y., and Yao, J. (2021). Stress granules modulate SYK to cause TAU-Associated neurocognitive deterioration in 5XFAD mouse after anesthesia and surgery. Front. Aging Neurosci. *13*, 718701. https://doi.org/10.3389/fnagi.2021.718701.

62. Shin, J., Park, S., Lee, H., and Kim, Y. (2021). Thioflavin-positive tau aggregates complicating quantification of amyloid plaques in the brain of 5XFAD transgenic mouse model. Sci. Rep. *11*, 1617. https://doi.org/10.1038/s41598-021-81304-6.

63. Manickam, R., Tur, J., Badole, S.L., Chapalamadugu, K.C., Sinha, P., Wang, Z., Russ, D.W., Brotto, M., and Tipparaju, S.M. (2022). Nampt activator P7C3 ameliorates diabetes and improves skeletal muscle function modulating cell metabolism and lipid mediators. J. Cachexia, Sarc. Mus. *13*, 1177–1196. https://doi.org/10.1002/jcsm.12887.

64. Gardell, S.J., Hopf, M., Khan, A., Dispagna, M., Hampton Sessions, E., Falter, R., Kapoor, N., Brooks, J., Culver, J., Petucci, C., et al. (2019). Boosting NAD^+ with a small molecule that activates NAMPT. Nat. Commun. *10*, 3241. https://doi.org/10.1038/s41467-019-11078-z.

65. Ratia, K.M., Shen, Z., Gordon-Blake, J., Lee, H., Laham, M.S., Krider, I.S., Christie, N., Ackerman-Berrier, M., Penton, C., Knowles, N.G., et al. (2023). Mechanism of allosteric modulation of nicotinamide phosphoribosyltransferase to elevate cellular NAD^+. Biochem. *62*, 923–933. https://doi.org/10.1021/acs.biochem.2c00655.

66. Shen, Z., Ratia, K., Krider, I., Ackerman-Berrier, M., Penton, C., Musku, S.R., Gordon-Blake, J.M., Laham, M.S., Christie, N., Ma, N., et al. (2023). Synthesis, optimization, and structure–activity relationships of nicotinamide phosphoribosyltransferase (NAMPT) positive allosteric modulators (N-PAMs). J. Med. Chem. *66*, 16704–16727. https://doi.org/10.1021/acs.jmedchem.3c01406.

67. Sridharan, P.S., Miller, E., and Pieper, A.A. (2023). Application of P7C3 compounds to investigating and treating acute and chronic traumatic brain injury. Neurotherapeutics *20*, 1616–1628. https://doi.org/10.1007/s13311-023-01427-8.

68. Bauman, M.D., Schumann, C.M., Carlson, E.L., Taylor, S.L., Vázquez-Rosa, E., Cintrón-Pérez, C.J., Shin, M.-K., Williams, N.S., and Pieper, A.A. (2018). Neuroprotective efficacy of P7C3 compounds in primate hippocampus. Trans. Psych *8*, 202. https://doi.org/10.1038/s41398-018-0244-1.

69. Pieper, A.A., Xie, S., Capota, E., Estill, S.J., Zhong, J., Long, J.M., Becker, G.L., Huntington, P., Goldman, S.E., Shen, C.-H., et al. (2010). Discovery of a proneurogenic, neuroprotective chemical. Cell *142*, 39–51. https://doi.org/10.1016/j.cell.2010.06.018.

70. MacMillan, K.S., Naidoo, J., Liang, J., Melito, L., Williams, N.S., Morlock, L., Huntington, P.J., Estill, S.J., Longgood, J., Becker, G.L., et al. (2011). Development of proneurogenic, neuroprotective small molecules. J. Am. Chem. Soc. *133*, 1428–1437. https://doi.org/10.1021/ja108211m.

71. Tesla, R., Wolf, H.P., Xu, P., Drawbridge, J., Estill, S.J., Huntington, P., McDaniel, L., Knobbe, W., Burket, A., Tran, S., et al. (2012). Neuroprotective efficacy of aminopropyl carbazoles in a mouse model of amyotrophic lateral sclerosis. Proc. Natl. Acad. Sci. USA *109*, 17016–17021. https://doi.org/10.1073/pnas.1213960109.

72. De Jesús-Cortés, H., Xu, P., Drawbridge, J., Estill, S.J., Huntington, P., Tran, S., Britt, J., Tesla, R., Morlock, L., Naidoo, J., et al. (2012). Neuroprotective efficacy of aminopropyl carbazoles in a mouse model of Parkinson's disease. Proc. Nat. Acad. Sci. USA *109*, 17010–17015. https://doi.org/10.1073/pnas.1213956109.

73. Naidoo, J., Bemben, C.J., Allwein, S.R., Liang, J., Pieper, A.A., and Ready, J.M. (2013). Development of a scalable synthesis of P7C3-A20, a potent neuroprotective compound. Tet. Lett. *54*, 4429–4431. https://doi.org/10.1016/j.tetlet.2013.06.024.

74. Blaya, M.O., Bramlett, H.M., Naidoo, J., Pieper, A.A., and Dietrich, W.D. (2014). Neuroprotective efficacy of a proneurogenic compound after traumatic brain injury. J. Neurotrauma *31*, 476–486. https://doi.org/10.1089/neu.2013.3135.

75. Pieper, A.A., McKnight, S.L., and Ready, J.M. (2014). P7C3 and an unbiased approach to drug discovery for neurodegenerative diseases. Chem. Soc. Rev. *43*, 6716–6726. https://doi.org/10.1039/c3cs60448a.

76. Walker, A.K., Qian, W., Chuang, J.-C., Tran, S., Lawrence, S.O., Morlock, L., Naidoo, J., Eisch, A., Williams, N.S., Pieper, A.A., et al. (2015). The P7C3 class of neuroprotective compounds exerts antidepressant efficacy in mice by increasing hippocampal neurogenesis. Mol. Psych *20*, 500–508. https://doi.org/10.1038/mp.2014.34.

77. Kemp, S.W.P., Szynkaruk, M., Stanoulis, K.N., Wood, M.D., Liu, E.H., Willand, M.P., Morlock, L., Naidoo, J., Williams, N.S., Ready, J.M., et al. (2015). Pharmacologic rescue of motor and sensory function by the neuroprotective compound P7C3 following neonatal nerve injury. Neuroscience *284*, 202–216. https://doi.org/10.1016/j.neuroscience.2014.10.005.

78. Naidoo, J., De Jesús-Cortés, H., Huntington, P., Estill, S., Morlock, L.K., Starwalt, R., Mangano, T.J., Williams, N.S., Pieper, A.A., and Ready, J.M. (2014). Discovery of a neuroprotective chemical, (S)- N -(3-(3,6-Dibromo-9 H -carbazol-9-yl)-2-fluoropropyl)-6-methoxypyridin-2-amine [(-)-P7C3-S243], with improved druglike properties. J. Med. Chem. *57*, 3746–3754. https://doi.org/10.1021/jm401919s.

79. Yin, T.C., Britt, J.K., De Jesús-Cortés, H., Lu, Y., Genova, R.M., Khan, M.Z., Voorhees, J.R., Shao, J., Katzman, A.C., Huntington, P.J., et al. (2014). P7C3 neuroprotective chemicals block axonal degeneration and preserve function after traumatic brain injury. Cell Rep. *8*, 1731–1740. https://doi.org/10.1016/j.celrep.2014.08.030.

80. Dutca, L.M., Stasheff, S.F., Heberg-Buenz, A., Rudd, D., Batra, N., Blodi, F.R., Yorek, M., Yin, T.C., Shankar, M., Herlein, J.A., et al. (2014). Early

detection of subclinical visual damage after blast-mediated TBI enables prevention of chronic visual deficit by treatment with P7C3-S243. IOVS (Investig. Ophthalmol. Vis. Sci.) *55*, 8330–8341. https://doi.org/10.1167/iovs.14-15468.

81. De Jesús-Cortés, H., Miller, A.D., Britt, J.K., De Marco, A.J., De Jesús-Cortés, M., Stuebing, E., Naidoo, J., Vázquez-Rosa, E., Morlock, L., Williams, N.S., et al. (2015). Protective efficacy of P7C3-S243 in the 6-hydroxydopamine model of Parkinson's disease. npj Parkinson's Dis. *1*, 15010. https://doi.org/10.1038/npjparkd.2015.10.
82. Lee, A.S., De Jesús-Cortés, H., Kabir, Z.D., Knobbe, W., Orr, M., Burgdorf, C., Huntington, P., McDaniel, L., Britt, J.K., Hoffman, F., et al. (2016). The neuropsychiatric disease associated gene cacna1c mediates survival of young hippocampal neurons. eNeuro *31*, ENEURO.0006-16.2015. https://doi.org/10.1523/ENEURO.0006-16.2016.
83. Loris, Z.B., Pieper, A.A., and Dietrich, W.D. (2017). The neuroprotective compound P7C3-A20 promotes neurogenesis and improves cognitive function after ischemic stroke. Exp. Neurol. *290*, 63–73. https://doi.org/10.1016/j.expneurol.2017.01.00.
84. Loris, Z.B., Hynton, J.R., Pieper, A.A., and Dietrich, W.D. (2018). Beneficial effects of delayed P7C3-A20 treatment after transient MCAO in rats. Transl. Stroke Res *9*, 146–156. https://doi.org/10.1007/s12975-017-0565-z.
85. Voorhees, J.R., Remy, M.T., McDaniel, L., El Rassi, E., Yin, T., Dutca, L.M., Cintrón-Pérez, C.J., Williams, N.S., Kahn, M., Brat, D.J., et al. (2018). (-)-P7C3-S243 protects a rat model of Alzheimer's disease from neuropsychiatric deficits and neurodegeneration without altering amyloid deposition or reactive glia. Biol. Psych. *84*, 488–498. https://doi.org/10.1016/j.biopsych.2017.10.023.
86. Bai, C.W., Tian, B., Zhang, M.C., Qin, Q., Shi, X., Yang, X., Gao, X., Zhou, X.Z., Shan, H.J., and Bai, J.Y. (2024). Targeting NAMPT-OPA1 for treatment of senile osteoporosis. Aging Cell Nove *14*, e14400. https://doi.org/10.1111/acel.14400.
87. Pieper, A.A., and McKnight, S.L. (2018). Evidence of benefit of enhancing nicotinamide adenine dinucleotide levels in damaged or diseased nerve cells. Cold Sprg. Harb. Symp. Quant. Biol. *83*, 207–217. https://doi.org/10.1101/sqb.2018.83.037622.
88. Bavley, C.C., Kabir, Z.D., Walsh, A.P., Kosovsky, M., Hackett, J., Sun, H., Vázquez-Rosa, E., Cintrón-Pérez, C.J., Miller, E., Koh, Y., et al. (2021). Dopamine D1R-neuron cacna1c deficiency: a new model of extinction therapy-resistant post-traumatic stress. Mol. Psych. *26*, 2286–2298. https://doi.org/10.1038/s41380-020-0730-8.
89. Vázquez-Rosa, E., Shin, M.K., Dhar, M., Chaubey, K., Cintrón-Pérez, C.J., Tang, X., Liao, X., Miller, E., Koh, Y., Barker, S., et al. (2020). P7C3-A20 treatment one year after TBI in mice repairs the blood-brain barrier, arrests chronic neurodegeneration, and restores cognition. Proc. Natl. Acad. Sci. USA *117*, 27667–27675. https://doi.org/10.1073/pnas.2010430117.
90. Schroeder, R., Sridharan, P., Nguyen, L., Loren, A., Williams, N.S., Cintrón-Pérez, C.J., Cintrón-Pérez, C.J., Vázquez-Rosa, E., Pieper, A.A., and Stevens, H.E. (2021). Maternal P7C3-A20 treatment protects offspring from neuropsychiatric sequelae of prenatal stress. Antiox.Redox Signal *35*, 511–530. https://doi.org/10.1089/ars.2020.8227.
91. Schroeder, R., Nguyen, L., Pieper, A.A., and Stevens, H.E. (2022). Maternal treatment with P7C3-A20 protects from impaired maternal care after chronic gestational stress. Behav. Brain Res. *416*, 113558. https://doi.org/10.1016/j.bbr.2021.113558.
92. Rahman, M.T., Bailey, E.M., Gansemer, B.M., Pieper, A.A., Manak, J.R., and Green, S.H. (2023). Anti-inflammatory therapy protects spiral ganglion neurons after aminoglycoside antibiotic-induced hair loss. Neurotherapeutics *20*, 578–601. https://doi.org/10.1007/s13311-022-01336-2.
93. Chorny, S., Borovicka, J., Patel, D., Shin, M.K., Vázquez-Rosa, E., Miller, E., Wilson, B.M., Pieper, A.A., and Hod, D. (2023). Longitudinal in vivo monitoring of axonal integrity after brain injury. Cell Rep. Methods *3*, 100481. https://doi.org/10.1016/j.crmeth.2023.100481.
94. Chen, Y., Zhu, Z., Yan, Y., Sun, H., Wang, G., Du, X., Li, F., Yuan, S., Wang, W., Wang, M., and Gu, C. (2024). P7C3 suppresses astrocytic senescence to protect dopaminergic neurons: implications in the mouse model of Parkinson's disease. CNS Neurosci. Ther. *30*, e14819. https://doi.org/10.1111/cns.14819.
95. Nishiguchi, T., Yamanishi, K., Patel, S., Malicoat, J.R., Phuong, N.J., Seki, T., Ishii, T., Aoyama, B., Shimura, A., Gorantla, N., et al. (2024). Discovery of novel neuroprotective agents for infection-related delirium through bispectral encephalography. Transl. Psych *14*, 413. https://doi.org/10.1038/s41398-024-03130-4.
96. Denninger, J.K., Smith, B.M., and Kirby, E.D. (2018). Novel object recognition and object location behavioral testing in mice on a budget. J. Vis. Exp. *20*, 14. https://doi.org/10.3791/58593.
97. Morris, R.G.M. (1981). Spatial localization does not require the presence of local cues. Learn. Motiv. *12*, 239–260. https://doi.org/10.1016/0023-9690(81)90020-5.
98. Dunham, N.W., and Miya, T.S. (1957). A note on a simple apparatus for Detecting Neurological Deficit in Rats and Mice. J. Am. Pharm. Assoc. *46*, 208–209. https://doi.org/10.1002/jps.3030460322.
99. Lyketsos, C.G., Lopez, O., Jones, B., Fitzpatrick, A.L., Breitner, J., and DeKosky, S. (2002). Prevalence of neuropsychiatric symptoms in dementia and mild cognitive impairment. JAMA *288*, 147. https://doi.org/10.1001/jama.288.12.1475.
100. Pellow, S., and File, S.E. (1986). Anxiolytic and anxiogenic drug effects on exploratory activity in an elevated plus-maze: A novel test of anxiety in the rat. Pharmacol. Biochem. Behav. *24*, 525–529. https://doi.org/10.1016/0091-3057(86)90552-6.
101. Forner, S., Kawauchi, S., Balderrama-Gutierrez, G., Kramár, E.A., Matheos, D.P., Phan, J., Javonillo, D.I., Tran, K.M., Hingco, E., Da Cunha, C., et al. (2021). Systematic phenotyping and characterization of the 5xFAD mouse model of Alzheimer's disease. Sci. Data *8*, 270. https://doi.org/10.1038/s41597-021-01054-y.
102. Porsolt, R.D., Bertin, A., and Jalfre, M. (1977). Behavioral despair in mice: a primary screening test for antidepressants. Arch. Int. Pharmacodyn. Ther. *229*, 327–336.
103. Guyenet, S.J., Furrer, S.A., Damian, V.M., Baughan, T.D., La Spada, A.R., and Garden, G.A. (2010). A simple composite phenotype scoring system for evaluating mouse models of cerebellar ataxia. J. Vis. Exp. *21*, 1787. https://doi.org/10.3791/1787.
104. Pirttilä, T., Kim, K.S., Mehta, P.D., Frey, H., and Wisniewski, H.M. (1994). Soluble amyloid β-protein in the cerebrospinal fluid from patients with Alzheimer's disease, vascular dementia and controls. J. Neurol. Sci. *127*, 90–95. https://doi.org/10.1016/0022-510x(94)90140-6.
105. Wilson, N., Kataura, T., Korsgen, M.E., Sun, C., Sarkar, S., and Korolchuk, V.I. (2023). The autophagy–NAD axis in longevity and disease. Trends Cell Biol. *33*, 788–802. https://doi.org/10.1016/j.tcb.2023.02.004.
106. Mputhia, Z., Hone, E., Tripathi, T., Sargeant, T., Martins, R., and Bharadwaj, P. (2019). Autophagy modulation as a treatment for amyloid diseases. Molecules *24*, 3372. https://doi.org/10.3390/molecules24183372.
107. Baterman, R.J., Xiong, C., Benzinger, T.L.S., Fagan, A.M., Goate, A., Fox, N.C., Marcus, D.S., Cairns, N.J., Xie, X., Blazwey, T.M., et al. (2012). Clinical and biomarker changes in dominantly inherited Alzheimer's disease. N. Engl. J. Med. *367*, 795–804. https://doi.org/10.1056/NEJMoa1202753.
108. Gordon, B.A., Blazey, T.M., Su, Y., Hari-Raj, A., Dincer, A., Flores, S., Christensen, J., McDade, E., Wang, G., Xiong, C., et al. (2018). Spatial patterns of neuroimaging biomarker change in individuals from families with autosomal dominant Alzheimer's disease: a longitudinal study. Lancet Neurol. *17*, 241–250. https://doi.org/10.1016/s1474-4422(18)30028-0.
109. McDade, E., Wang, G., Gordon, B.A., Hassenstab, J., Benzinger, T.L.S., Buckles, V., Fagan, A.M., Holtzman, D.M., Cairns, N.J., Goate, A.M., et al. (2018). Longitudinal cognitive and biomarker changes in dominantly inherited Alzheimer disease. Neurology *91*, e1295–e1306. https://doi.org/10.1012/WNL.0000000000006277.

110. Villemagne, V.L., Burnham, S., Bourgeat, P., Brown, B., Ellis, K.A., Salvado, O., Szoeke, C., Macaulay, S.L., Martins, R., Maruff, P., et al. (2013). Amyloid b deposition, neurodegeneration, and cognitive decline in sporadic Alzheimer's disease: a prospective cohort study. Lancet Neurol. *12*, 357–2367. https://doi.org/10.1016/S1474-4422(13)70044-9.

111. Scholl, M., Maass, A., Mattson, N., Ashton, N.J., Blennow, K., Zetterberg, H., and Jagust, W. (2019). Biomarkers for tau pathology. Mol. Cell. Neurosci. *97*, 18–33. https://doi.org/10.1212/01.wnl.0000046581.81650.d0.

112. Palmqvist, S., Janelidze, S., Quiroz, Y.T., Zetterberg, H., Lopera, F., Stomrud, E., Su, Y., Chen, Y., Serrano, G.E., Leuzy, A., et al. (2020). Discriminative accuracy of plasma phospho-tau217 for Alzheimer disease vs other neurodegenerative disorders. JAMA *324*, 772–781. https://doi.org/10.1001/jama.2020.12134.

113. Thijssen, E.H., La Joie, R., Strom, A., Fonseca, C., Iaccarino, L., Wolf, A., Spina, S., Allen, I.E., Cobigo, Y., Heuer, H., et al. (2021). Plasma phosphorylated tau 217 and phosphorylated tau 181 as biomarkers in Alzheimer's disease and frontotemporal lobar degeneration: a retrospective diagnostic performance study. Lancet Neurol. *20*, 739–752. https://doi.org/10.1016/S1474-4422(21)00214-3.

114. Hanes, J., Kovac, A., Kvartsberg, H., Kontsekova, E., Fialova, L., Katina, S., Kovacech, B., Stevens, E., Hort, J., Vyhnalek, M., et al. (2020). Evaluation of a novel immunoassay to detect p-tau Thr217 in the CWSF to distinguish Alzheimer's disease from other dementias. Neurology *95*, e3026–e3035. https://doi.org/10.1212/WNL.0000000000010814.

115. Mendes, A.J., Ribaldi, F., Lathuiliere, A., Ashton, N.J., Janelidze, S., Zetterberg, H., Scheffler, M., Assal, F., Garibotto, V., Blennow, K., et al. (2024). Head-to-head study of diagnostic accuracy of plasma and cerebrospinal fluid p-tau217 versus p-tau181 and p-tau231 in a memory clinic cohort. J. Neurol. *271*, 2053–2066. https://doi.org/10.1007/s00415-023-12148-5.

116. Ashton, N.J., Puig-Pijoan, A., Milà-Alomà, M., Fernández-Lebrero, A., García-Escobar, G., González-Ortiz, F., Kac, P.R., Brum, W.S., Benedet, A.L., Lantero-Rodriguez, J., et al. (2023). Plasma and CSF biomarkers in a memory clinic: head-to-head comparison of phosphorylated tau immunoassays. Alzheimer's Dement. *19*, 1913–1924. https://doi.org/10.1002/alz.12841.

117. Barthelemy, N.R., Salvado, G., Schindler, S.E., He, Y., Janelidze, S., Collij, L.E., Saef, B., Henson, R.L., Chen, C.D., Gordon, B.A., et al. (2024). Highly accurate blood test for Alzheimer's disease is similar or superior to clinical cerebrospinal fluid tests. Nat. Med. *30*, 1085–1095. https://doi.org/10.1038/s41591-024-02869-z.

118. Daneman, R. (2012). The blood–brain barrier in health and disease. Ann. Neurol. *72*, 648–672. https://doi.org/10.1022/ana.23648.

119. Shlosberg, D., Benifla, M., Kaufer, D., and Friedman, A. (2010). Blood–brain barrier breakdown as a therapeutic target in traumatic brain injury. Nat. Rev. Neurol. *6*, 393–403. https://doi.org/10.1038/nrneurol.2010.74.

120. Montagne, A., Zhao, Z., and Zlokovic, B.V. (2017). Alzheimer's disease: A matter of blood–brain barrier dysfunction? J. Exp. Med. *214*, 3151–3169. https://doi.org/10.1084/jem.20171406.

121. Vesković, A., Nakarada, Đ., Pavićević, A., Prokić, B., Perović, M., Kanazir, S., Popović-Bijelić, A., and Mojović, M. (2021). In Vivo/Ex vivo EPR investigation of the brain redox status and Blood-Brain barrier integrity in the 5xFAD mouse model of Alzheimer's disease. Curr. Alzheimer Res. *18*, 25–34. https://doi.org/10.2174/1567205018666210324121156.

122. Smyth, L.C.D., Highet, B., Jansson, D., Wu, J., Rustenhoven, J., Aalderink, M., Tan, A., Li, S., Johnson, R., Coppieters, N., et al. (2022). Characterisation of PDGF-BB:PDGFRβ signaling pathways in human brain pericytes: evidence of disruption in Alzheimer's disease. Commun. Biol. *5*, 235. https://doi.org/10.1038/s42003-022-03180-8.

123. Ding, R., Hase, Y., Ameen-Ali, K.E., Ndung'u, M., Stevenson, W., Barsby, J., Gourlay, R., Akinyemi, T., Akinyemi, R., Uemura, M.T., et al. (2020). Loss of capillary pericytes and the blood–brain barrier in white matter in poststroke and vascular dementias and Alzheimer's disease. Brain Pathol. *30*, 1087–1110. https://doi.org/10.1111/bpa.12888.

124. Shi, H., Koronyo, Y., Fuchs, D.T., Sheyn, J., Jallow, O., Mandalia, K., Graham, S.L., Gupta, V.K., Mirzaei, M., Kramerov, A.A., et al. (2023). Retinal arterial Aβ40 deposition is linked with tight junction loss and cerebral amyloid angiopathy in MCI and AD patients. Alzheimer's Dement. *19*, 5185–5197. https://doi.org/10.1002/alz.13086.

125. Thadathil, N., Delotterie, D.F., Xiao, J., Hori, R., McDonald, M.P., and Khan, M.M. (2021). DNA double-strand break accumulation in Alzheimer's disease: evidence from experimental models and postmortem human brains. Mol. Neurobiol. *58*, 118–131. https://doi.org/10.1007/s12035-020-02109-8.

126. Delint-Ramirez, I., and Madabhushi, R. (2025). DNA damage and its links to neuronal aging and degeneration. Neuron *113*, 7–28. https://doi.org/10.1016/j.neuron.2024.12.001.

127. Simpson, J.E., Ince, P.G., Lace, G., Forster, G., Shaw, P.J., Matthews, F., Savva, G., Brayne, C., and Wharton, S.B.; MRC Cognitive Function and Ageing Neuropathology Study Group (2010). Astrocyte phenotype in relation to Alzheimer-type pathology in the ageing brain. Neurobiol. Aging *31*, 578–590. https://doi.org/10.1016/j.neurobiolaging.2008.05.015.

128. Heneka, M.T., Rodríguez, J.J., and Verkhratsky, A. (2010). Neuroglia in neurodegeneration. Brain Res. Rev. *63*, 189–211. https://doi.org/10.1016/j.brainresrev.2009.11.004.

129. Lull, M.E., and Block, M.L. (2010). Microglial activation and chronic neurodegeneration. Neurotherapeutics *7*, 354–365. https://doi.org/10.1016/j.nurt.2010.05.014.

130. Petitto, J.M., McNamara, R.K., Gendreau, P.L., Huang, Z., and Jackson, A.J. (1999). Impaired learning and memory and altered hippocampal neurodevelopment resulting from interleukin-2 gene deletion. J. Neurosci. Res. *56*, 441–446. https://doi.org/10.1002/(SICI)1097-4547(19990515)56:4<441::AID-JNR11>3.0.CO;2-G.

131. Alves, S., Churlaud, G., Audrain, M., Michaelsen-Preusse, K., Fol, R., Souchet, B., Braudeau, J., Korte, M., Klatzmann, D., and Cartier, N. (2017). Interleukin-2 improves amyloid pathology, synaptic failure and memory in Alzheimer's disease mice. Brain *140*, 826–842. https://doi.org/10.1093/brain/aww330.

132. Brombacher, T.M., Nono, J.K., De Gouveia, K.S., Makena, N., Darby, M., Womersley, J., Tamgue, O., and Brombacher, F. (2017). IL-13–Mediated Regulation of Learning and Memory. J. Imunol. *198*, 2681–2688. https://doi.org/10.4049/jimmunol.1601546.

133. Gusel'nikova, V.V., and Korzhevskiy, D.E. (2015). NeuN as a neuronal nuclear antigen and neuron differentiation marker. Acta Naturae *7*, 42–47.

134. Spalding, K.L., Bergmann, O., Alkass, K., Bernard, S., Salehpour, M., Huttner, H.B., Boström, E., Westerlund, I., Vial, C., Buchholz, B.A., et al. (2013). Dynamics of hippocampal neurogenesis in adult humans. Cell *153*, 1219–1227. https://doi.org/10.1016/j.cell.2013.05.002.

135. Moreno-Jiménez, E.P., Flor-García, M., Terreros-Roncal, J., Rábano, A., Cafini, F., Pallas-Bazarra, N., Ávila, J., and Llorens-Martín, M. (2019). Adult hippocampal neurogenesis is abundant in neurologically healthy subjects and drops sharply in patients with Alzheimer's disease. Nat. Med. *25*, 554–560. https://doi.org/10.1038/s41591-019-0375-9.

136. Zaletel, I., Schwirtlich, M., Perović, M., Jovanović, M., Stevanović, M., Kanazir, S., and Puškaš, N. (2018). Early impairments of hippocampal neurogenesis in 5xFAD mouse model of Alzheimer's disease are associated with altered expression of SOXB transcription factors. J. Alzheimer's Dis. *65*, 963–976. https://doi.org/10.3233/JAD-180277.

137. Smith, M.A., Rudnicka-Nawrot, M., Richey, P.L., Praprotnik, D., Mulvihill, P., Miller, C.A., Sayre, L.M., and Perry, G. (1995). Carbonyl-Related post-translational modification of neurofilament protein in the neurofibrillary pathology of Alzheimer's disease. J. Neurochem. *64*, 2660–2666. https://doi.org/10.1046/j.1471-4159.1995.64062660.x.

138. Di Domenico, F., Tramutola, A., and Butterfield, D.A. (2017). Role of 4-hydroxy-2-nonenal (HNE) in the pathogenesis of Alzheimer disease and other selected age-related neurodegenerative disorders. Free Radic. Biol. Med. *111*, 253–261. https://doi.org/10.1016/j.freeradbiomed.2016.10.490.

139. Smith, M.A., Richey Harris, P.L., Sayre, L.M., Beckman, J.S., and Perry, G. (1997). Widespread peroxynitrite-mediated damage in Alzheimer's disease. J. Neurosci. *17*, 2653–2657. https://doi.org/10.1523/JNEUROSCI.17-08-02653.1997.

140. Wei, Y., Shin, M.R., and Sesti, F. (2018). Oxidation of KCNB1 channels in the human brain and in mouse model of Alzheimer's disease. Cell Death Dis. *9*, 820. https://doi.org/10.1038/s41419-018-0886-1.

141. Brigida, I., Zoccolillo, M., Cicalese, M.P., Pfajfer, L., Barzaghi, F., Scala, S., Oleaga-Quintas, C., Álvarez-Álvarez, J.A., Sereni, L., Giannelli, S., et al. (2018). T-cell defects in patients with *ARPC1B* germline mutations account for immunodeficiency. Blood *132*, 2362–2374. https://doi.org/10.1182/blood-2018-07-863431.

142. Yin, H., Xu, L., and Porter, N.A. (2011). Free radical lipid peroxidation: Mechanisms and analysis. Chem. Rev. *111*, 5944–5972. https://doi.org/10.1021/cr200084z.

143. Zhong, H., and Yin, H. (2015). Role of lipid peroxidation derived 4-hydroxynonenal (4-HNE) in cancer: Focusing on mitochondria. Redox Biol. *4*, 193–199. https://doi.org/10.1016/j.redox.2014.12.011.

144. Raza, H., John, A., Brown, E.M., Benedict, S., and Kambal, A. (2008). Alterations in mitochondrial respiratory functions, redox metabolism and apoptosis by oxidant 4-hydroxynonenal and antioxidants curcumin and melatonin in PC12 cells. Toxicol. Appl. Pharm. *226*, 161–168. https://doi.org/10.1016/j.taap.2007.09.002.

145. Dodson, M., Wani, W.Y., Redmann, M., Benavides, G.A., Johnson, M.S., Ouyang, X., Cofield, S.S., Mitra, K., Darley-Usmar, V., and Zhang, J. (2017). Regulation of autophagy, mitochondrial dynamics, and cellular bioenergetics by 4-hydroxynonenal in primary neurons. Autophagy *13*, 1828–1840. https://doi.org/10.1080/15548627.2017.1356948.

146. Preiss, J., and Handler, P. (1958). Biosynthesis of diphosphopyridine nucleotide. I. Identification of intermediates. J. Biol. Chem. *233*, 488–492.

147. Lin, M.T., and Beal, M.F. (2006). Mitochondrial dysfunction and oxidative stress in neurodegenerative diseases. Nature *443*, 787–795. https://doi.org/10.1038/nature05292.

148. Zhu, X.-H., Lu, M., Lee, B.-Y., Ugurbil, K., and Chen, W. (2015). In vivo NAD assay reveals the intracellular NAD contents and redox state in healthy human brain and their age dependences. Proc. Natl. Acad. Sci. USA *112*, 2876–2881. https://doi.org/10.1073/pnas.1417921112.

149. Goedert, M., Jakes, R., and Vanmechelen, E. (1995). Monoclonal antibody AT8 recognises tau protein phosphorylated at both serine 202 and threonine 205. Neurosci. Lett. *189*, 167–169. https://doi.org/10.1016/0304-3940(95)11484-E.

150. Takeuchi, H., Iba, M., Inoue, H., Higuchi, M., Takao, K., Tsukita, K., Karatsu, Y., Iwamoto, Y., Miyakawa, T., Suhara, T., et al. (2011). P301S mutant human Tau transgenic mice manifest early symptoms of human tauopathies with dementia and altered sensorimotor gating. PLoS One *6*, e21050. https://doi.org/10.1371/journal.pone.0021050.

151. Askenazi, M., Kavanagh, T., Pires, G., Ueberheide, B., Wisniewski, T., and Drummond, E. (2023). Compilation of reported protein changes in the brain in Alzheimer's disease. Nat. Commun. *14*, 4466. https://doi.org/10.1038/s41467-023-40208-x.

152. Zhou, X., Su, S., Li, S., Pang, X., Chen, C., Li, J., and Liu, J. (2016). MicroRNA-146a down-regulation correlates with neuroprotection and targets pro-apoptotic genes in cerebral ischemic injury in vitro. Brain Res. *1648*, 136–143. https://doi.org/10.1016/j.brainres.2016.07.034.

153. Zhang, C., Qi, H., Jia, D., Zhao, J., Xu, C., Liu, J., Cui, Y., Zhang, J., Wang, M., Chen, M., and Tang, B. (2024). Cognitive impairment in Alzheimer's disease FAD^{4T} mouse model: synaptic loss facilitated by activated microglia via C1qA. Life Sci. *340*, 122457. https://doi.org/10.1016/j.lfs.2024.122457.

154. Qu, J., Xiong, X., Hujie, G., Ren, J., Yan, L., and Ma, L. (2021). MicroRNA-132-3p alleviates neuron apoptosis and impairments of learning and memory abilities in Alzheimer's disease by downregulation of HNRNPU stabilized BACE1. Cell Cycle *20*, 2309–2320. https://doi.org/10.1080/15384101.2021.1982507.

155. Ye, J., Beetz, N., O'Keefe, S., Tapia, J.C., Macpherson, L., Chen, W.V., Bassel-Duby, R., Olson, E.N., and Maniatis, T. (2015). hnRNP U protein is required for normal pre-mRNA splicing and postnatal heart development and function. Proc. Natl. Acad. Sci. USA *112*, E3020–E3029. https://doi.org/10.1073/pnas.1508461112.

156. Vassar, R. (2004). BACE1: the beta-secretase enzyme in Alzheimer's disease. J. Mol. Neurosci. *23*, 105–114. https://doi.org/10.1385/JMN:23:1-2:105.

157. Zhou, G.-F., Tang, J., Ma, Y.-L., Fu, X., Liu, J.-Y., Yang, R.-Z., Zhang, H.-S., Cai, X.-H., Wang, J.-W., Xie, X.-Y., et al. (2023). ARL6IP1 mediates small-molecule-induced alleviation of Alzheimer pathology through FXR1-dependent BACE1 translation initiation. Proc. Natl. Acad. Sci. USA *120*, e2220148120. https://doi.org/10.1073/pnas.2220148120.

158. Bhattacharya, U., Neizer-Ashun, F., Mukherjee, P., and Bhattacharya, R. (2020). When the chains do not break: the role of USP10 in physiology and pathology. Cell Death Dis. *11*, 1033. https://doi.org/10.1038/s41419-020-03246-7.

159. Piatnitskaia, S., Takahashi, M., Kitaura, H., Katsuragi, Y., Kakihana, T., Zhang, L., Kakita, A., Iwakura, Y., Nawa, H., Miura, T., et al. (2019). USP10 is a critical factor for Tau-positive stress granule formation in neuronal cells. Sci. Rep. *9*, 10591. https://doi.org/10.1038/s41598-019-47033-7.

160. Wei, Z., Zeng, K., Hu, J., Li, X., Huang, F., Zhang, B., Wang, J.-Z., Liu, R., Li, H.-L., and Wang, X. (2022). USP10 deubiquitinates Tau, mediating its aggregation. Cell Death Dis. *13*, 726. https://doi.org/10.1038/s41419-022-05170-4.

161. Liu, W.J., Ye, L., Huang, W.F., Guo, L.J., Xu, Z.G., Wu, H.L., Yang, C., and Liu, H.F. (2016). p62 links the autophagy pathway and the ubiquitin-proteasome system upon ubiquitinated protein degradation. Cell. Mol. Biol. Lett. *21*, 29. https://doi.org/10.1186/s11658-016-0031-z.

162. Tashiro, E., Zako, T., Muto, H., Itoo, Y., Sörgjerd, K., Terada, N., Abe, A., Miyazawa, M., Kitamura, A., Kitaura, H., et al. (2013). Prefoldin protects neuronal cells from polyglutamine toxicity by preventing aggregation formation. J. Biol. Chem. *288*, 19958–19972. https://doi.org/10.1074/jbc.M113.477984.

163. Tao, Y., Han, Y., Yu, L., Wang, Q., Leng, S.X., and Zhang, H. (2020). The predicted key molecules, functions, and pathways that bridge mild cognitive impairment (MCI) and Alzheimer's disease (AD). Front. Neurol. *11*, 233. https://doi.org/10.3389/fneur.2020.00233.

164. Sorgjerd, K.M., Zako, T., Sakono, M., Stirling, P.C., Leroux, M.R., Saito, T., Nilsson, P., Sekimoto, M., Saido, T.C., and Maeda, M. (2013). Human prefoldin inhibits amyloid-β (Aβ) fibrillation and contributes to formation of nontoxic Aβ aggregates. Biochemistry *52*, 3532–3542. https://doi.org/10.1021/bi301705c.

165. Rulten, S., Thorpe, J., and Kay, J. (1999). Identification of eukaryotic parvulin homologues: a new subfamily of peptidylprolyl cis-trans isomerases. Biochem. Biophys. Res. Commun. *259*, 557–562. https://doi.org/10.1006/bbrc.1999.0828.

166. Uchida, T., Fujimori, F., Tradler, T., Fischer, G., and Rahfeld, J.U. (1999). Identification and characterization of a 14 kDa human protein as a novel parvulin-like peptidyl prolyl cis/trans isomerase. FEBS Lett. *446*, 278–282. https://doi.org/10.1016/s0014-5793(99)00239-2.

167. Surmacz, T.A., Bayer, E., Rahfeld, J.U., Fischer, G., and Bayer, P. (2002). The N-terminal basic domain of human parvulin hPar14 is responsible for the entry to the nucleus and high-affinity DNA-binding. J. Mol. Biol. *321*, 235–247. https://doi.org/10.1016/s0022-2836(02)00615-0.

168. Suzuki, M., Tezuka, K., Handa, T., Sato, R., Takeuchi, H., Takao, M., Tano, M., and Uchida, Y. (2022). Upregulation of ribosome complexes at the blood-brain barrier in Alzheimer's disease patients. J. Cereb. Blood Flow Metab. *42*, 2134–2150. https://doi.org/10.1177/0271678X221111602.

169. Pravata, P.M., Omelkova, M., Stavridis, M.P., Desbiens, C.M., Stephan, H.M., Lefeber, D.J., Gecz, J., Gundogdu, M., Ounap, K., Joss, S., et al. (2020). An intellectual disability syndrome with single-nucleotide variants in)-GlcNAc transferase. Eur. J. Hum. Genet. *28*, 706–714. https://doi.org/10.1038/s41431-020-0589-9.

170. Ji, W., An, K., Wang, C., and Wang, S. (2022). Bioinformatics analysis of diagnostic biomarkers for Alzheimer's disease in peripheral blood based on sex differences and support vector machine algorithm. Hereditas *159*, 38. https://doi.org/10.1186/s41065-022-00252-x.

171. Lee, T., and Lee, H. (2021). Shared blood transcriptomic signatures between Alzheimer's disease and diabetes mellitus. Biomedicines *9*, 34. https://doi.org/10.3390/biomedicines9010034.

172. Arreola, R., Valderrama, B., Morante, M.L., and Horjales, E. (2003). Two mammalian glucosamine-6-phosphate deaminases: a structural and genetic study. FEBS Lett. *551*, 63–70. https://doi.org/10.1016/s0014-5793(03)00896-2.

173. Yuzwa, S.A., and Vocadlo, D.J. (2014). O-GlcNac and neurodegeneration: biochemical mechanisms and potential roles in Alzheimer's disease and beyond. Chem. Soc. Rev. *43*, 6839–6858. https://doi.org/10.1039/c4cs00038b.

174. Oikari, S., Makkonen, K., Deen, A.J., Tyni, I., Kärnä, R., Tammi, R.H., and Tammi, M.I. (2016). Hexosamine biosynthesis in keratinocytes: roles of GFAT and GNPDA enzymes in the maintenance of UDP-GlcNAc content and hyaluronan synthesis. Glycobiology *26*, 710–722. https://doi.org/10.1093/glycob/cww019.

175. Dzyubenko, E., Gottschling, C., and Faissner, A. (2016). Neuron-glia interactions in neural plasticity: contributions of neural extracellular matrix and perineuronal nets. Neural Plast. *2016*, 5214961. https://doi.org/10.1155/2016/5214961.

176. Wilson, E., Knudson, W., and Newell-Litwa, K. (2020). Hyaluronan regulates synapse formation and function in developing neural networks. Sci. Rep. *10*, 16459. https://doi.org/10.1038/s41598-020-73177-y.

177. Dong, Y., Zhao, K., Qin, X., Du, G., and Gao, L. (2023). The mechanisms of perineuronal net abnormalities in contributing aging and neurological diseases. Ageing Res. Rev. *92*, 102092. https://doi.org/10.1016/j.arr.2023.102092.

178. Roerig, P., Mayerhofer, P., Holzinger, A., and Gärtner, J. (2001). Characterization and functional analysis of the nucleotide binding fold in human peroxisomal ATP binding cassette transporters. FEBS Lett. *492*, 66–72. https://doi.org/10.1016/s0014-5793(01)02235-9.

179. van Roermund, C.W.T., Ijlst, L., Wagemans, T., Wanders, R.J.A., and Waterham, H.R. (2014). A role for the human peroxisomal half-transporter ABCD3 in the oxidation of dicarboxylic acids. Biochim. Biophys. Acta *1841*, 563–568. https://doi.org/10.1016/j.bbalip.2013.12.001.

180. Jo, D.S., and Cho, D.-H. (2019). Peroxisomal dysfunction in neurodegenerative diseases. Arch Pharm. Res. (Seoul) *42*, 393–406. https://doi.org/10.1007/s12272-019-01131-2.

181. Uzor, N.-E., McCullough, L.D., and Tsvetkov, A.S. (2020). Peroxisomal dysfunction in neurological diseases and brain aging. Front. Cell. Neurosci. *14*, 44. https://doi.org/10.3389/fncel.2020.00044.

182. Semikasev, E., Ahlemeyer, B., Acker, T., Schänzer, A., and Baumgart-Vogt, E. (2023). Rise and fall of peroxisomes during Alzheimer's disease: a pilot study in human brains. Acta Neuropathol. Commun. *11*, 80. https://doi.org/10.1186/s40478-023-01567-0.

183. Bibb, M.J., Van Etten, R.A., Wright, C.T., Walberg, M.W., and Clayton, D.A. (1981). Sequence and gene organization of mouse mitochondrial DNA. Cell *26*, 167–180. https://doi.org/10.1016/0092-8674(81)90300-7.

184. Shcgerbakov, D., Juskeviciene, R., Sanchon, A.C., Brilkova, M., Rehrauer, H., Laczo, E., and Bottger, E.C. (2021). Mitochondrial mistranslation in brain provokes a metabolic response which mitigates the age-associated decline in mitochondrial gene expression. Int. J. Mol. Sci. *22*, 2746. https://doi.org/10.3390/ijms22052746.

185. Yuan, J., Xie, B.M., Ji, Y.M., Bao, H.J., Wang, J.L., Cheng, J.C., Huang, X.C., Zhao, Y., and Chen, S. (2025). piR-26441 inhibits mitochondrial oxidative phosphorylation and tumorigenesis in ovarian cancer through m6A modification by interacting with YTHDC1. Cell Death Dis. *16*, 25. https://doi.org/10.1038/s41419-025-07340-6.

186. Smeitink, J.A.M., Elpeleg, O., Antonicka, H., Diepstra, H., Saada, A., Smits, P., Sasarman, F., Vriend, G., Jacob-Hirsch, J., Shaag, A., et al. (2006). Distinct clinical phenotypes associated with a mutation in the mitochondrial translation elongation factor. Am. J. Hum. Genet. *79*, 869–877. https://doi.org/10.1086/508434.

187. Perli, E., Pisano, A., Glasgow, R.I.C., Carbo, M., Hardy, S.A., Falkous, G., He, L., Cerbelli, B., Pignataro, M.G., Zacara, E., et al. (2019). Novel compound mutations in the mitochondrial translation elongation factor (TSFM) gene cause severe cardiomyopathy with myocardial fibro-adipose replacement. Sci. Rep. *9*, 5108. https://doi.org/10.1038/s41598-019-41483-9.

188. Tu, H.-Q., Qin, X.H., Liu, Z.-B., Song, Z.-Q., Hu, H.-B., Zhang, Y.-C., Chang, Y., Wu, M., Huang, Y., Bai, Y.-F., et al. (2018). Microtubule asters anchored by FSD1 control axoneme assembly and ciliogenesis. Nat. Commun. *9*, 5277. https://doi.org/10.1038/s41467-018-07664-2.

189. Mack, M., Schniegler-Mattox, U., Peters, V., Hoffmann, G.F., Liesert, M., Buckel, W., and Zschocke, J. (2006). Biochemical characterization of human 3-methylglutaconyl-CoA hydratase and its role in leucine metabolism. FEBS J. *273*, 2012–2022. https://doi.org/10.1111/j.1742-4658.2006.05218.x.

190. Nakagawa, J., and Moroni, C. (1997). A 20-amino-acid autonomous RNA-binding domain contained in an enoyl-CoA hydratase. Eur. J. Biochem. *244*, 890–899. https://doi.org/10.1111/j.1432-1033.1997.00890.x.

191. Kurimoto, K., Fukai, S., Nureki, O., Muto, Y., and Yokoyama, S. (2001). Crystal structure of human AUH protein, a single stranded RNA binding homolog of enoyl-CoA hydratase. Structure *9*, 1253–1263. https://doi.org/10.1016/s0969-2126(01)00686-4.

192. Uzarska, M.A., Nasta, V., Weiler, B.D., Spantgar, F., Ciofi-Baffoni, S., Saviello, M.R., Gonnelli, L., Mühlenhoff, U., Banci, L., and Lill, R. (2016). Mitochondrial Bol1 and Bol3 function as assembly factors for specific iron-sulfur proteins. eLife *5*, e16673. https://doi.org/10.7554/eLife.16673.

193. Peters, D.G., Connor, J.R.,, and Meadowcroft, M.D. (2015). The relationship between iron dyshomeostasis and amyloidogenesis in Alzheimer's disease: two sides of the same coin. Neurobiol. Dis. *81*, 49–65. https://doi.org/10.1016/j.nbd.2015.08.007.

194. Isaya, G. (2014). Mitochondrial iron-sulfur cluster dysfunction in neurodegenerative disease. Front. Pharmacol. *5*, 29. https://doi.org/10.3389/fphar.2014.00029.

195. Wagner, F., Kunz, T.C., Chowdhury, S.R., Thiede, B., Fraunholz, M., Eger, D., and Kozjak-Pavlovic, V. (2019). Armadillo repeat-containing protein 1 is a dual localization protein associated with mitochondrial intermembrane space bridging complex. PLoS One *14*, e0218303. https://doi.org/10.1371/journal.pone.0218303.

196. Wells, T., Davies, J.R., Guschina, I.A., Ball, D.J., Davies, J.S., Davies, V.J., Evans, B.A.J., and Votruba, M. (2012). Opa3, a novel regulator of mitochondrial function, controls thermogenesis and abdominal fat mass in a mouse model for Costeff syndrome. Hum. Mol. Genet. *21*, 4836–4844. https://doi.org/10.1093/hmg/dds315.

197. Lenaers, G., Hamel, C., Delettre, C., Amati-Bonneau, P., Procaccio, V., Bonneau, D., Reynier, P., and Milea, D. (2012). Dominant optic atrophy. Orphanet J. Rare Dis. *7*, 46. https://doi.org/10.1186/1750-1172-7-46.

198. Reynier, P., Amati-Bonneau, P., Verny, C., Olichon, A., Simard, G., Guichet, A., Bonnemains, C., Malecaze, F., Malinge, M.C., Pelletier, J.B., et al. (2004). OPA3 gene mutations responsible for autosomal dominant atrophy and cataract. J. Med. Genet. *41*, e110. https://doi.org/10.1136/jmg.2003.016576.

199. Anikster, Y., Kleta, R., Shaag, A., Gahl, W.A., and Elpeleg, O. (2001). Type III 3-methylglutaconic aciduria (optic atrophy plus syndrome, or Costeff optic atrophy syndrome): identification of the OPA3 gene and its founder mutation in Iraqi Jews. Am. J. Hum. Genet. *69*, 1218–1224. https://doi.org/10.1086/324651.

200. Kleta, R., Skovby, F., Christensen, E., Rosenberg, T., Gahl, W.A., and Anikster, Y. (2002). 3-methylglutaconic aciduria type III in a non-Iraqi-Jewish kindred: clinical and molecular findings. Mol. Genet. Metab. *76*, 201–206. https://doi.org/10.1016/s1096-7192(02)00047-1.

201. Fiermonte, G., Paradies, E., Todisco, S., Marobbio, C.M.T., and Palmieri, F. (2009). A novel member of solute carrier family 25 (SLC25A42) is a transporter of coenzyme A and adenosine 3',5'-diphosphate in human mitochondria. J. Biol. Chem. *284*, 18152–18159. https://doi.org/10.1074/jbc.M109.014118.

202. Pagliarini, D.J., Wiley, S.E., Kimple, M.E., Dixon, J.R., Kelly, P., Worby, C.A., Casey, P.J., and Dixon, J.E. (2005). Involvement of a mitochondrial phosphatase in the regulation of ATP production and insulin secretion in pancreatic beta cells. Mol. Cell *19*, 197–207. https://doi.org/10.1016/j.molcel.2005.06.008.

203. Zhang, J., Guan, Z., Murphy, A.N., Wiley, S.E., Perkins, G.A., Worby, C.A., Engel, J.L., Heacock, P., Nguyen, O.K., Wang, J.H., et al. (2011). Mitochondrial phosphatase PTPMT1 is essential for cardiolipin biosynthesis. Cell Metab. *13*, 690–700. https://doi.org/10.1016/j.cmet.2011.04.007.

204. Falabella, M., Vernon, H.J., Hanna, M.G., Claypool, S.M., and Pitceathly, R.D.S. (2021). Cardiolipin, mitochondria, and neurological disease. Trends Endocrinol. Metab. *32*, 224–237. https://doi.org/10.1016/j.tem.2021.01.006.

205. Andrews, W., Barber, M., Hernadez-Miranda, L.R., Xian, J., Rakic, S., Sundaresan, V., Rabbitts, T.H., Pannell, R., Rabbitts, P., Thompson, H., et al. (2008). The role of Slit-Robo signaling in the generation, migration and morphological differentiation of cortical interneurons. Dev. Biol. *313*, 648–658. https://doi.org/10.1016/j.ydbio.2007.10.052.

206. Blockus, H., Rolotti, S.V., Szoboszlay, M., Peze-Heidsieck, E., Ming, T., Schroeder, A., Apostolo, N., Vennekens, K.M., Katsamba, P.S., Bahna, F., et al. (2021). Synaptogenic activity of the axon guidance molecule Robo2 underlies hippocampal circuit function. Cell Rep. *37*, 109828. https://doi.org/10.1016/j.celrep.2021.109828.

207. Sasaki, T., Komatsu, Y., and Yamamori, T. (2020). Expression patterns of SLIT/ROBO mRNAs reveal a characteristic feature in the entorhinal-hippocampal area of macaque monkeys. BMC Res. Notes *13*, 262. https://doi.org/10.1186/s13104-020-05100-7.

208. Johnson, E.C.B., Carter, E.K., Dammer, E.B., Duong, D.M., Gerasimov, E.S., Liu, Y., Liu, J., Betarbet, R., Ping, L., Yin, L., et al. (2022). Large-scale deep multi-layer analysis of Alzheimer's disease brain reveals strong proteomic disease-related changes not observed at the RNA level. Nat. Neurosci. *25*, 213–225. https://doi.org/10.1038/s41593-021-00999-y.

209. Fairman-Williams, M.E., Guenther, U.-P., and Jankowsky, E. (2010). SF1 and SF1 helicases: family matters. Curr. Opin. Struct. Biol. *20*, 313–324. https://doi.org/10.1016/j.sbi.2010.03.011.

210. Lee, T., and Pelletier, J. (2016). The biology of DHX9 and its potential as a therapeutic target. Oncotarget *7*, 42716–42739. https://doi.org/10.18632/oncotarget.8446.

211. Chakraborty, P., Huang, J.T.J., and Hiom, K. (2018). DHX9 helicase promotes R-loop formation in cells with impaired RNA splicing. Nat. Commun. *9*, 4346. https://doi.org/10.1038/s41467-018-06677-1.

212. Yang, L., Liu, Q., Zhao, Y., Lin, N., Huang, Y., Wang, Q., Yang, K., Wei, R., Li, X., Zhang, M., et al. (2024). DExH-box helicase 9 modulates hippocampal synapses and regulates neuropathic pain. iScience *27*, 109016. https://doi.org/10.1016/j.isci.2024.109016.

213. Guo, Y., Sun, C.K., Tang, L., and Tan, M.S. (2023). Microglia PTK2B/Pyk2 in the pathogenesis of Alzheimer's disease. Alzheimer Res *20*, 692–704. https://doi.org/10.2174/0115672050299004240129051655.

214. Brody, A.H., Nies, S.H., Guan, F., Smith, L.M., Mukherjee, B., Salazar, S.A., Lee, S., Lam, T.K.T., and Strittmatter, S.M. (2022). Alzheimer risk gene producto Pyk2 suppresses tau phosphorylation and phenotypic effects of tauopathy. Mol. Neurodegener. *17*, 32. https://doi.org/10.1186/s13024-022-00526-y.

215. Salazar, S.V., Cox, T.O., Lee, S., Brody, A.H., Chyung, A.S., Haas, L.T., and Strittmatter, S.M. (2019). Alzheimer's disease risk factor Pyk2 mediates amyloid-beta-induced synaptic dysfunction and loss. J. Neurosci. *39*, 758–772. https://doi.org/10.1523/JNEUROSCI.1873-18.2018.

216. Dourlen, P., Fernandez-Gomez, F.J., Dupont, C., Grenier-Boley, B., Bellenguez, C., Obriot, H., Caillierez, R., Sottejeau, Y., Chapuis, J., Bretteville, A., et al. (2017). Functional screening of Alzheimer risk loci identifies PTK2B as an in vivo modulator and early marker of Tau pathology. Psychiatry *22*, 874–883. https://doi.org/10.1038/mp.2016.59.

217. Suzuki, M., Tezuka, K., Handa, T., Sato, R., Takeuchi, H., Takao, M., Tano, M., and Uchida, Y. (2022). Upregulation of ribosome complexes at the blood-brain barrier in Alzheimer's disease patients. J. Cereb. Blood Flow Metab. *42*, 2134–2150. https://doi.org/10.1177/0271678X221111602.

218. Zhang, X., Zou, L., Meng, L., Xiong, M., Pan, L., Chen, G., Zheng, Y., Xiong, J., Wang, Z., Duong, D.M., et al. (2021). Amphiphysin I cleavage by asparagine endopeptidase leads to tau hyperphosphorylation and synaptic dysfunction. eLife *10*, e65301. https://doi.org/10.7554/eLife.65301.

219. Liu, C., Zhang, L., Wu, J., Sui, X., Xu, Y., Huang, L., Han, Y., Zhu, H., Li, Y., Sun, X., and Qin, C. (2017). AnkG hemizygous mice present cognitive impairment and elevated anxiety/depressive-like traits associated with decreased expression of GABA receptors and postsynaptic density protein. Exp. Brain Res. *235*, 3375–3390. https://doi.org/10.1007/s00221-017-5056-7.

220. Sun, X., Wu, Y., Gu, M., Liu, Z., Ma, Y., Li, J., and Zhang, Y. (2014). Selective filtering defect at the axon initial segment in Alzheimer's disease mouse models. Proc. Natl. Acad. Sci. USA *111*, 14271–14276. https://doi.org/10.1073/pnas.1411837111.

221. Sun, X., Wu, Y., Gu, M., and Zhang, Y. (2014). miR-342-5p decreases ankyrin G levels in Alzheimer's disease transgenic mouse models. Cell Rep. *6*, 264–270. https://doi.org/10.1016/j.celrep.2013.12.028.

222. Benitez, M.J., Retana, D., Ordoñez-Gutiérrez, L., Colmena, I., Goméz, M.J., Álvarez, R., Ciorraga, M., Dopazo, A., Wandosell, F., Garrido, J.J., et al. (2024). Transcriptomic alterations in APP/PS1 mice astrocytes lead to early postnatal axon initial segment structural changes. Cell. Mol. Life Sci. *81*, 444. https://doi.org/10.1007/s00018-024-05485-9.

223. Fan, L.-F., Xu, D.-E., Wang, W.-H., Yan, K., Wu, H., Yao, X.-Q., Xu, R.-X., Liu, C.-F., and Ma, Q.-H. (2013). Caspr interaction with amyloid precursor protein reduces amyloid-β generation in vitro. Neurosci. Lett. *548*, 255–260. https://doi.org/10.1016/j.neulet.2013.05.055.

224. Qian, W., Yuan, L., Zhuge, W., Gu, L., Chen, Y., Zhuge, Q., Ni, H., and Lv, X. (2024). Regulating Lars2 in mitochondria: a potential Alzheimer's therapy by inhibiting tau phosphorylation. Neurotherapeutics *21*, e00353. https://doi.org/10.1016/j.neurot.2024.e00353.

225. Zhao, H., Kim, Y., Park, J., Park, D., Lee, S.-E., Chang, I., and Chang, S. (2014). SCAMP5 plays a critical role in synaptic vesicle endocytosis during high neuronal activity. J. Neurosci. *34*, 10085–10095. https://doi.org/10.1523/JNEUROSCI.2156-14.2014.

226. Barker, S., Paul, B.D., and Pieper, A.A. (2023). Increased risk of aging-related neurodegenerative disease after traumatic brain injury. Biomedicines *11*, 1154. https://doi.org/10.3390/biomedicines11041154.

227. Allen, M., Carrasquillo, M.M., Funk, C., Heavner, B.D., Zou, F., Younkin, C.S., Burgess, J.D., Chai, H.S., Crook, J., Eddy, J.A., et al. (2016). Human whole genome genotype and transcriptome for Alzheimer's and other neurodegenerative diseases. Sci. Data *3*, 160089. https://doi.org/10.1038/sdata.2016.89.

228. Askenazi, E.M., Lazar, E.A., and Grinberg, I. (2023). Identification of high-reliability regions of machine learning predictions based on materials

chemistry. J. Chem. Inf. Model. *63*, 7350–7362. https://doi.org/10.1021/acs.jcim.3c01684.

229. Gabitto, M.I., Travaglini, K.J., Rachleff, V.M., Kaplan, E.S., Long, B., Ariza, J., Ding, Y., Mahoney, J.T., Dee, N., Goldy, J., et al. (2024). Integrated multimodal cell atlas of Alzheimer's disease. Nat. Neurosci. *27*, 2366–2383. https://doi.org/10.1038/s41593-024-01774-5.

230. Leroy, K., Ando, K., Laporte, V., Dedecker, R., Suain, V., Authelet, M., Héraud, C., Pierrot, N., Yilmaz, Z., Octave, J.N., and Brion, J.P. (2012). Lack of tau proteins rescues neuronal cell death and decreases amyloidogenic processing of APP in APP/PS1 mice. Am. J. Pathol. *181*, 1928–1940. https://doi.org/10.1016/j.ajpath.2012.08.012.

231. Min, S.-W., Cho, S.-H., Zhou, Y., Schroeder, S., Haroutunian, V., Seeley, W.W., Huang, E.J., Shen, Y., Masliah, E., Mukherjee, C., et al. (2010). Acetylation of tau inhibits its degradation and contributes to tauopathy. Neuron *67*, 953–966. https://doi.org/10.1016/j.neuron.2010.08.044.

232. Woo, J.A., Zhao, X., Khan, H., Penn, C., Wang, X., Joly-Amado, A., Weeber, E., Morgan, D., and Kang, D.E. (2015). Slingshot-cofilin activation mediates mitochondrial and synaptic dysfunction via Aβ ligation to β1-integrin conformers. Cell Death Diff *22*, 1069–1070. https://doi.org/10.1038/cdd.2015.41.

233. Yan, S., Conley, J.M., Reilly, A.M., Stull, N.D., Abhyankar, S.D., Ericsson, A.C., Kono, T., Molosh, A.I., Kubal, C.A., Evans-Molina, C., and Ren, H. (2022). Intestinal Gpr17 deficiency improves glucose metabolism by promoting GLP-1 secretion. Cell Rep. *38*, 110179. https://doi.org/10.1016/j.celrep.2021.110179.

234. Goedhart, J., and Luijsterburg, M.S. (2020). VolcaNoseR is a web app for creating, exploring, labeling and sharing volcano plots. Sci. Rep. *10*, 20560. https://doi.org/10.1038/s41598-020-76603-3.

235. Ge, S.X., Jung, D., and Yao, R. (2020). ShinyGO: a graphical gene-set enrichment tool for animals and plants. Bioinformatics *36*, 2628–2629. https://doi.org/10.1093/bioinformatics/btz931.

236. Tang, D., Chen, M., Huang, X., Zhang, G., Zeng, L., Zhang, G., Wu, S., and Wang, Y. (2023). SRplot: A free online platform for data visualization and graphing. PLoS One *18*, e0294236. https://doi.org/10.1371/journal.pone.0294236.

237. Crowell, H.L., Soneson, C., Germain, P.-L., Calini, D., Collin, L., Raposo, C., Malhotra, D., and Robinson, M.D. (2020). Muscat detects subpopulation-specific state transitions from multi-sample multi-condition single-cell transcriptomics data. Nat. Commun. *11*, 6077. https://doi.org/10.1038/s41467-020-19894-4.

CellPress
OPEN ACCESS

STAR★METHODS

KEY RESOURCES TABLE

REAGENT or RESOURCE	SOURCE	IDENTIFIER
Antibodies		
Mouse monoclonal anti-phosoho-Tau (S202, T205)	Thermo Fisher Scientific	Cat# MN1020; RRID:AB_223647
Mouse monoclonal anti-Tau (T46)	Thermo Fisher Scientific	Cat# 13–6400; RRID:AB_2533025
Rabbit monoclonal anti-phospho-Tau (Thr217)	Cell Signaling Technology	Cat# 51625S; RRID:AB_3068604
Mouse monoclonal anti-beta-Amyloid, 1-16	BioLegend	Cat# 803001; RRID:AB_2564653
Mouse monoclonal anti-GAPDH	Millipore	Cat# MAB374; RRID:AB_2107445
Rabbit polyclonal anti-Amyloid Precursor Protein, C-Terminal	Sigma	Cat# A8717; RRID:AB_258409
Horse anti-mouse/anti-rabbit IgG (H + L)	Vector Laboratories	Cat# BA-1400; RRID:AB_2336187
Goat polyclonal anti-mouse aminopeptidase n	R and D Systems	Cat# AF2335; RRID:AB_2227288
Rat monoclonal anti-mouse CD31	BD Biosciences	Cat# 550274; RRID:AB_393571
Mouse monoclonal anti-ZO-1	Thermo Fisher Scientific	Cat# 33–9100; RRID:AB_2533147
Mouse monoclonal anti-NeuN	Millipore	Cat# MAB377; RRID:AB_2298772
Mouse monoclonal anti-5-bromodeoxyuridine	Sigma-Aldrich	Cat# SAB4700630; RRID:AB_10896613
Rabbit monoclonal anti-GFAP (D1F4Q)	Cell Signaling Technology	Car#12389; RRID:AB_2631098
Mouse monoclonal anti-GFAP (ASTRO6)	Thermo Fisher Scientific	Cat# MA5-12023; RRID:AB_10984338
Rabbit polyclonal anti-Iba1	FUJIFILM Wako Shibayagi	Cat# 019–19741; RRID:AB_839504
Rabbit polyclonal anti-PSD95	Abcam	Cat# ab18258; RRID:AB_444362
Rabbit polyclonal anti-4 hydroxynonenal (HNE) antiserum	Alpha Diagnostic International	Cat# HNE11-S, RRID:AB_2629282
Rabbit polyclonal anti-Nitrotyrosine Antibody	Millipore Sigma	Cat# AB5411, RRID:AB_177459
Mouse monoclonal anti-β-Actin (C4)	Santa Cruz Biotechnology	Cat# sc-47778, RRID:AB_626632
Goat polyclonal anti-rabbit IgG, HRP-linked	Cell Signaling Technology	Cat# 7074; RRID:AB_2099233
Horse polyclonal anti-mouse IgG, HRP-linked	Cell Signaling Technology	Cat# 7076; RRID:AB_330924
Alexa Fluor 488 Goat anti-Mouse IgG (H + L)	Thermo Fisher Scientific	Cat# A32723; RRID:AB_2633275
Alexa Fluor 594 Goat anti-Rabbit IgG (H + L)	Thermo Fisher Scientific	Cat# A32740; RRID:AB_2762824
Alexa Fluor 488 Goa anti-Rabbit IgG (H + L)	Thermo Fisher Scientific	Cat# A32731; RRID:AB_2633280
Biological samples		
Human cortical brain tissue	Mesulam Center for Cognitive Neurology and Alzheimer's Disease, Northwestern University	https://www.brain.northwestern.edu/
Human cortical brain tissue	Case Western Reserve University/ University Hospital Memory and Aging Center Brain Bank	https://www.uhhospitals.org/uh-research/department-research/psychiatry-research/research-studies/cadrc-memory-aging-research-study
Chemicals, peptides, and recombinant proteins		
P7C3-A20	Andrew A. Pieper	N/A
FK866 hydrochloride hydrate	Sigma-Aldrich	F8557; CAS: 658084-64-1 (free base)
Hydrogen Peroxide	Fisher Scientific	H325-500; CAS: 7722-84-1, 7732-18-5

(*Continued on next page*)

Continued

REAGENT or RESOURCE	SOURCE	IDENTIFIER
Critical commercial assays		
NAD/NADH assay kit	BioVision	Cat# K337-100
Human/Rat β Amyloid(40)ELISA Kit Wako	FUJIFILM Wako Pure Chemical Corporation	Cat# 294-62501
Human/Rat β Amyloid(42) ELISA Kit Wako	FUJIFILM Wako Pure Chemical Corporation	Cat# 292-64501
FD NeuroSilver Kit	FD NeuroTechnologies, Inc	Cat# PK301
Seahorse XF cell Mito Stress Test kit	Agilent	Cat# 103015
TUNEL Assay Kit (Fluorescence, 488 nm)	Cell Signaling	Cat# 25879
OxyBlot™ Protein oxidation Detection Kit	Millipore Sigma	Cat# S7150
Aurum Serum Protein Mini Kit	Bio-Rad	Cat# 7326701
Human Tau (phospho T217) ELISA Kit	Abcam	Cat# ab318936
Experimental models: Cell lines		
Primary Human Brain Microvascular Endothelial Cells	Cell systems	Cat#ACBRI376
Experimental models: Organisms/strains		
Mouse: B6SJL-Tg	The Jackson Laboratory	RRID:MMRRC_034840-JAX
Mouse: B6SJLF1/J-WT	The Jackson Laboratory	RRID:IMSR_JAX:100012
Mouse: B6;C3-Tg(Prnp-MAPT*P301S)PS19Vle/J	The Jackson Laboratory	RRID:IMSR_JAX:008169
Software and algorithms		
Any-maze behavior tracking software	Stoelting	https://www.any-maze.com/
ImageJ/Fiji	National Institute of Health, Bethesda, MD	https://imagej.nih.gov/ij
Prism	GraphPad	https://www.graphpad.com/features
Image Lab 6.0.1 build 34	Bio-Rad	https://www.bio-rad.com/en-us/product/image-lab-software?ID=KRE6P5E8Z#fragment-6
ZEN	ZISS	https://www.zeiss.com/microscopy/en/products/software/zeiss-zen.html
Deposited Data		
All Omics Datasets	Generated by the Authors	https://zenodo.org/records/17455622e
Other		
Zeiss Axio Scan.Z1	Carl Zeiss	N/A
Zeiss AxioImager.M2	Carl Zeiss	N/A

EXPERIMENTAL ANIMALS, CELLS, AND HUMAN SUBJECTS DETAILS

Cell culture

Primary Human Brain Microvascular Endothelial cells (Cellsystems, ACBRI 376) were used for experiments. Cells were grown in complete classic Medium with serum and CultureBoost (Cellsystems, 4Z0-500) with 1% penicillin/streptomycin (Gibco, 15140-122). Cells were tested to ensure no mycoplasma contamination.

Animals

Heterozygous 5xFAD mice (B6SJL, #034840-JAX) and corresponding WT littermates (B6SjLF1/J, #100012), were purchased from the Jackson Laboratory and bred at our animal facility at Louis Stokes Cleveland VA Medical Center under specific protocol and guidance as approved by the IACUC (No. 18-050-MS-21-007), in accordance with the guidelines of the National Institutes of Health Guide for the Care and Use of Laboratory Animals. As paternal inheritance of the 5xFAD transgene causes mice to develop a higher amyloid plaque burden than when it is maternally inherited, independent of mouse age, sex, and colony,[57] we utilized experimental mice that were derived from a male 5xFAD HET × female WT breeding pair system. Animals were maintained in a temperature and humidity-controlled room with a 12 h light/dark cycle. They were housed in a pathogen-free cage and with normal chow and water *ad libitum* and were observed continuously during all experimental procedures by the designated veterinarian. If required, veterinarian care was performed for sick animals. PS19 mouse experiments were performed in accordance with protocols approved by the IACUC of the

CellPress
OPEN ACCESS

Johns Hopkins University School of Medicine (No. MO21M457), in accordance with the guidelines of the National Institutes of Health Guide for the Care and Use of Laboratory Animals. Animals were housed in a temperature-controlled room (22°C) with a 12 h light/dark cycle and had access to normal chow and water *ad libitum*. Non-carrier and hemizygous PS19 (strain no. #:008169) breeder pairs were procured from Jackson Laboratories and further bred to maintain the colony.

Human samples

Human samples used in this study were obtained from Northwestern University Alzheimer's Disease Research Center brain bank and Case Western Reserve University under approved study protocol. All samples were collected after providing written consent for the use of brain tissue. Specific age and other details for the human sample used are provided in Table S1 and S2. The Banner dataset from the human whole genome genotype and transcriptome data previously published[227] was used to generate the RNA sequencing data for NAD^+-synthesizing and degrading enzyme encoding genes. Human proteome database was analyzed by supplementary table 5 from the study by Askenazi et al. (2023).[228] Human transcriptome database for male and female middle temporal gyrus (MTG) and dorsolateral prefrontal cortex (DLPFC) was analyzed from The Seattle Alzheimer's Disease Brain Cell Atlas (SEA-AD) consortium (https://portal.brain-map.org/explore/seattle-alzheimers-disease/whatis and Gabitto et al.).[229]

METHOD DETAILS

P7C3-A20 pharmacokinetics and binding analysis

P7C3-A20 levels in mouse plasma and brain were monitored by LC-MS/MS using an AB Sciex (Framingham, MA) Triple Quad 4500 mass spectrometer coupled to a Shimadzu (Columbia, MD) Prominence LC. P7C3-A20 was detected with the mass spectrometer in positive MRM (multiple reaction monitoring) mode by following the precursor to fragment ion transitions 507.1 to 204.3 (quantifier ion) and 507.1 to 136.2 (qualifier ion). An Agilent C18 XDB column (5 micron, 50 × 4.6 mm) was used for chromatography for PK studies with the following conditions: Buffer A: dH20 + 0.1% formic acid, Buffer B: methanol +0.1% formic acid, 0–1.0 min 5% B, 1.0–1.5 min gradient to 100% B, 1.5–3.0 min 100% B, 3.0–3.15 min gradient to 5% B, 3.15–4.5 5% B. N-benzylbenzamide (transition 212.12 to 91.1) from Sigma (St. Louis, MO) was used as an internal standard (IS). Pharmacokinetic studies were performed by injecting 8 week old B6SJLF1/J male and female mice with 10 mg/kg P7C3-A20 IP formulated in 2.5% DMSO, 10% Kolliphor EL, 87.5% D5W (5% dextrose in water, pH 7.4) daily for four days. At various times following the fourth dose, animals were euthanized, blood was collected into K2EDTA tubes, mice were perfused with cold phosphate buffered saline (Fisher Scientific, BP399-20) and brains collected. Tissues were weighed before snap freezing and blood spun at 9600 x g to collect plasma which was stored frozen along with brain tissue at −80°C until analysis. Brain tissue was homogenized using a T25 Ultra Turrax Tissue Disperser (IKA, Wilmington, NC) in a 3-fold volume (weight by volume) of PBS to generate a homogenate. Fifty μL of plasma mixed with 50 μL PBS or 100 μL of tissue homogenate was added to a Phree Phospholipid Removal Tabbed 1 mL Tube (Phenomenex, Torrance, CA) mounted on a Vacuum Extraction Manifold (Waters, Milford, MA.) Three hundred μl of acetonitrile containing 0.116% formic acid and 29 ng/mL n-benzylbenzamide IS was added, mixed 3x by pipetting, and a vacuum was applied. The flow through was collected and an additional 300 μL of acetonitrile containing formic acid and IS was passed over the tabbed tube and also collected. The flow through was transferred to an HPLC vial and analyzed as described above. Standard curves were generated using blank K2EDTA CD1 mixed gender mouse plasma (Bioreclamation, Westbury, NY) or blank CD1 brain tissue homogenate spiked with known concentrations of P7C3-A20 (Lot CR416FFS-7657-32-A-P) DMSO standards and processed as described above. The concentration of drug in each time-point sample was quantified using Analyst software (Sciex). A value of 3-fold above the signal obtained from blank plasma or tissue homogenate was designated the limit of detection (LOD). The limit of quantitation (LOQ) was defined as the lowest concentration at which back calculation yielded a concentration within 20% of theoretical. Concentrations for male and female mice were plotted separately but were nearly identical.

Protein binding of P7C3-A20 in mouse plasma or brain homogenate was determined by rapid equilibrium dialysis using RED chambers (Thermo Scientific, Waltham, MA). On the day of the RED experiment, frozen mouse plasma and 3x homogenized blank brain was thawed in a water bath at 37°C. Then it was equilibrated for 45 min at 37°C in an atmosphere of 5% CO2. The pH of PBS was confirmed within 7.4 ± 0.1. The pH of plasma and brain was measured and adjusted to 7.4 ± 0.1 using concentrated acid or base. Plasma was diluted at 1:10 and brain diluted at 1:20 (final) with PBS and used for all subsequent steps. An aliquot of plasma or brain was spiked with compound to a compound concentration of 5 μM and vortex mixed. Enough non-spiked matrix remained to enable matrix matching of dialysate at the end of the binding assessment. This matrix was stored at 37°C in an atmosphere of 5% CO2. For each matrix, dialysis was performed using $n = 4$ individual RED units with 200 μL of compound spiked plasma at 5 μM in the donor chamber and 400 μL of PBS in the dialysate chamber. The plate containing the RED units was sealed with a gas-permeable seal and incubated at 37°C for 6 h under a 5% CO2 atmosphere in an orbital shaker set to 100 rpm. At the end of the dialysis period, aliquots were taken from the donor and dialysate chambers of each RED unit to obtain post-dialysis measures of bound and unbound compound concentration. Donor, dialysate, and plasma or brain stability samples were analyzed by using a matrix matching approach whereby each sample was mixed in a 1:1 ratio with the opposite medium (blank matrix or PBS). The matrix matched samples were then processed as described above for PK samples. P7C3-A20 levels in both chambers were measured by LC-MS/MS as described above and the ratio of analyte/IS used in place of an absolute concentration as shown below to determine the % bound. For each matrix, stability was assessed by maintaining individual aliquots of compound-spiked matrix at 37°C and 5% CO2 for 0 and 6 h. At

each time point, $n = 2$ 50 μL aliquots were matrix matched and crashed. Stability of P7C3-A20 in plasma and brain was 95% or greater over 6 h as assessed by LC-MS/MS. Fraction unbound (fu) was determined based on the following equations:

$$f_u = \frac{C_{dialysate}}{C_{donor}}$$

$$DF = \frac{Total\ volume\ of\ solution}{Volume\ of\ aliquot}$$

$$Undiluted\ f_u = \frac{{}^{1}/DF}{\left(\left({}^{1}/fu_{\ diluted}\right) - 1\right) + {}^{1}/DF}$$

f_u-fraction unbound,
$C_{dialysate}$-concentration of compound in dialysate chamber after dialysis,
C_{donor}-concentration of compound in donor chamber after dialysis,
DF - dilution factor for plasma dilution,
$f_{uundiluted}$-fraction unbound after correcting for plasma dilution,
$fu_{diluted}$-fraction unbound of diluted plasma; calculated using the fu equation above if using diluted plasma.

In vivo animal treatment

Two-month-old (for mid-disease cohort) and 6-month-old (for advanced-disease cohort) WT and 5xFAD mice were randomly divided into treatment groups and co-housed during the entire experiment. Intraperitoneal injections of vehicle (2.5% DMSO, 10% Kolliphor, and 5% Dextrose, pH 7.4) or P7C3-A20 (10 mg/kg) dissolved in vehicle were conducted every day in both cohorts. Animals were divided into 2 cohorts. Cohort 1 was designated as the mid-disease group and received injections every day from 2 months to 6 months. Cohort 2 was designated as the advanced-disease group and received injections every day 6–12 months. In each cohort, animals were divided into four treatment groups: WT VEH, 5xFAD VEH, WT P7C3-A20 and 5xFAD P7C3-A20. Each treatment group consisted of 20–25 males and 20–25 females. For PS19 mice experiments, 11-month-old PS19 male and female mice and corresponding WT animals were injected with P7C3-A20 or Vehicle for one month, with behavioral analysis after 15 and 30 days of treatment.

Behavioral analysis

Object recognition test

This 3-day task uses an open-topped box (50 × 50 × 30 cm) in which animals were habituated for 5 min on day one without any objects. On day two, animals were allowed to explore two similar objects for a total of 20 s. Each session had a maximum time of 10 min. On day three, the familiar object was replaced by a triplicate copy of the same object (to ensure there are no olfactory cues) and a novel object. Discrimination index was calculated by subtracting the exploration time for the new object from the exploration time for the old object divided by total exploration time (20 s). Boxes and objects were cleaned between each testing session using Clidox. Animals were brought to the experimental testing room 30 min prior to the experiment for habituation.

Elevated plus maze

This 5-min test was performed only once per animal. To measure anxiety-like behavior, animals were placed in the center of a cross-shaped maze elevated 38 cm above the floor consisting of two open and two closed arms (50 cm). The behavior of the rodents was then monitored for 5 min by a video tracking system. Time spent in the open, closed, and center arms was automatically recorded using Anymaze software.

Accelerating rotarod motor coordination test

In this three-day test, Rotamex 5 by Columbus Instruments was used to evaluate each animal's performance. On the first two days (learning phase), animals were trained on a rotarod that moved at a constant speed of 4 rpm for 600s, with three trials conducted for each animal with a one-hour gap between each trial. The graph was prepared based on the average of all three trials. On the third day, a probe test was conducted. The animals were placed on the rotarod, which started at 4 rpm and accelerated at 1.2 rpm every 20 s until it reached 40 rpm. The time and acceleration speed were recorded for each animal when it fell from the rod. Three repeated tests were conducted for each animal, with an interval of one hour between each test.

Porsolt forced swim test (FST)

Depression-like features in the animals were analyzed by FST. Animals were brought to the experimental testing room in their home cages on the day of each testing session and remained in the experimental room for 30 min prior to testing to habituate. Cylindrical swim tanks measuring 20 cm in diameter and 45 cm tall were filled with 24°C–25°C water to a height of 30 cm. Animals were placed in the tank for 6 min and the time spent immobile, defined as no detectable movement for ≥2 s, was recorded. Animals were removed with paper towels, gently blotted dry, and exposed to a warming pad to be sure they were observably dry before being returned to the room.

CellPress
OPEN ACCESS

Hindlimb clasping

Hindlimb clasping score was recorded for each animal by tail suspension for 30 s. Animals were assigned a clasping score of zero if both hindlimbs were apart, a score of one if one hindlimb was touching the abdomen, and a score of two if both hind limbs were touching the abdomen. A score of three was allotted to animals that clasped all four limbs toward the abdomen.

Morris Water maze

Learning and memory were analyzed by the 5 days Morris water maze (MWM) test in which animals were motivated/trained to reach a hidden submerged platform. Animals were brought to the experimental testing room in their home cages on the day of each testing session and remained in the experimental room for 30 min prior to testing. The Morris water maze is a silver, circular water tank, measuring 167 cm in diameter filled with 24°C–25°C water to approximately 60 cm. A clear, plastic escape platform is submerged below the surface of the water, and the animals learn to locate this escape platform by utilizing four high contrast equally spaced spatial cues located around the maze. During each test, the animal was subjected to training comprised of four trials per day, and the time spent to find the platform was recorded, up to a maximum of 60 s. If the animal did not reach the platform by 60 s, it was gently manually guided to the platform and then removed from the maze. On day five, a probe trial was conducted, during which the platform was removed and the animal's memory of the escape location based on spatial cues was analyzed. Anymaze video tracking software (Stoelting Co.) was used to measure the latency to cross the previous platform location.

Sample harvesting

Animals were anesthetized with ketamine (100 mg/kg) and xylazine (10 mg/kg) and blood was isolated. Brain was dissected, collected in liquid nitrogen, and stored immediately at −80°C for further biochemical analysis. For the histopathological study, tissue was prepared as described previously.[51] Briefly, mice were transcardially perfused with cold 1x phosphate buffer saline (PBS) followed by 4% paraformaldehyde in PBS (pH 7.4). Brains were collected and post-fixed in 4% paraformaldehyde in PBS (pH 7.4) overnight at 4°C. On the next day, brains were transferred to 30% sucrose in PBS for 72 h at 4°C and then rapidly frozen in 2-methylbutane chilled at −20°C. Next, 40 μm thick brain sections were prepared and preserved in cryoprotectant (150 mM Ethylene glycol, 100 mM glycerol, 250 mM PBS) at −20°C for further use.

NAD^+/NADH measurement

Brain tissue NAD^+/NADH measurement was performed as per manufacture protocol (BioVision, K337-100). Briefly, 20 mg of cortical brain tissue was washed with cold PBS, homogenized in NADH/NAD extraction buffer, and centrifuged at 14000 rpm for 5 min. The supernatant was filtered through a 10 kDa molecular weight cutoff filter to remove NADH-consuming enzymes. Fifty μL of diluted filtrate were used to assay NAD total (NADt) in a 96 well plate. Another 200 μL of the filtrate was heated to 60°C for 30 min to decompose NAD^+, and 50 μL of diluted solution was added to the same 96 well plate to measure NADH. Ten μL of 1 nmol/mL NADH standard was diluted with 990 μL of NADH/NAD extraction buffer and 0, 20,40, 60, 80, and 100 pmol/well standard was added to the same 96 well plate as above with a final volume of 50 μL. An additional 100 μL of NAD cycling enzyme mix was added, mixed, and incubated at room temperature for 5 min. After this, 10 μL of NADH developer was added and absorbance was measured at 450 nm as defined by manufacture protocol. For measuring NAD^+/NADH in cell culture, HBMVECs were grown in 6 well plates (~2 x 10^6 cells/well) and treated with each treatment condition. Then, cell pellets were washed in cold PBS and centrifuged at 900 g for 10 min. The pellet was further lysed with NADH/NAD extraction buffer, vortexed for 10 s, and then centrifuged at 14000 rpm for 5 min before NAD^+/NADH measurement as described above for tissue.

Brain homogenate preparation for soluble/insoluble Aβ and p-tau measurement

Cortical brain tissue was homogenized with 500 μL of ice-cold radioimmunoprecipitation assay (RIPA) buffer (Sigma-Aldrich, R0278) supplemented with 1x phosphatase and protease inhibitors (Thermo Scientific, 1861284). Samples were allowed to stand for 15 min at 4°C and separated into three aliquots for Aβ, p-tau, and biochemical analysis and stored immediately at −80°C until further use. From one aliquot, 100 μL samples were taken and processed for Aβ analysis as previously described.[230] Briefly, homogenate was centrifuged at 20,000 x g for 20 min at 4°C. The supernatant was used for Aβ 1–40/Aβ 1–42 analysis in the soluble fraction. The pellet was then resuspended in 3-fold volume of 100% formic acid (Sigma-Aldrich, F0507) and dissolved by vortexing and pipetting, followed by overnight incubation at 4°C on a rotator. The next day, this solution was centrifuged at 20,000 x g at 4°C for 20 min and supernatant was neutralized by 19 volumes of 2 mol/L Tris buffer. This fraction was used for analysis of Aβ 1–40/Aβ 1–42 in insoluble fraction. Another aliquot of 100 μL was processed for p-tau analysis as previously described.[231] Briefly, 1 mM of phenylmethyl sulfonyl fluoride (Sigma Aldrich, P7626), 5 mM nicotinamide (Sigma-Aldrich, 72340), and 1 mM trichostatin A (Sigma-Aldrich, T8552) were added to the sample, followed by sonication and then centrifugation at 43,000 rpm for 15 min at 4°C. The supernatant was removed and centrifuged at 18,000 x g for 10 min at 4°C, and the resultant supernatant was used for p-tau and total tau analysis. For plasma phospho-tau217 western blot analysis high abundant proteins were depleted by Aurum Serum Protein mini kit as described by manufacture protocol (Bio-Rad, 7326701). For measuring plasma phospho-tau217 levels Human Tau (phospho T217) ELISA kit-Extracellular (abcam, ab318936) was used. Plasma samples were diluted in 1:4 ratios and were run exactly same way as defined by manufacture.

Soluble insoluble Aβ 1–40/1-42 analysis

Soluble insoluble Aβ 1-40/1-42 analysis was done by using Human/Rat β Amyloid (42) or (40) ELISA Kit (Wako, High Sensitive (code no. 292–64501, 294–64701)). Briefly, different dilutions of Aβ 40 (100, 50, 10, 5, 2.5, and 1 pmol/L) and Aβ 42 (20, 10,5, 2, 1,0.5, and 0.1 pmol/L) were prepared in the standard diluent. Both kits provided the antibody-coated microplate for analysis of Aβ 40 and Aβ 42. For Aβ 40 analysis, the antibody-coated microplate was brought to room temperature. Then, 100 μL of standard diluent was added to a well as the blank. Other wells of the plate were coated with 100 μL of standard or sample for Aβ 40 analysis. For Aβ 42 analysis, the antibody-coated microplate was also brought to room temperature. Then, 100 μL of standard diluent was added to a well as the blank. Other wells of the plate were coated with 100 μL of standard or sample for Aβ 42 analysis. Both plates were sealed with plate seal and refrigerated overnight. On the next day, each well was washed 5 times with wash solution and 100 μL of HRP conjugated antibody solution was added into each well. Plates were sealed again and incubated in refrigeration for 1 h. After 1 h, solution was removed from each well and wells were washed 5 times. Then, TMB solution (100 μL) was added to each well and both plates were incubated in the dark at room temperature for 30 min. To terminate the reaction, stop solution (100 μL) was added to each well. Absorbance was recorded by a microplate reader (Spectra Max) at 450 nm.

Western blotting

Briefly, brain tissue homogenate in RIPA buffer with 1x protease and phosphatase inhibitors was sonicated and centrifuged at 18,000 x g at 4°C for 30 min. Supernatant was collected and protein concentration was measured by bicinchonic (BCA) protein assay kit (Thermo Scientific, A53225). An equal amount of protein sample for each analysis was mixed with Laemmli Sample buffer (Bio Rad Laboratories, Inc.#1610737) with beta-mercaptoethanol (Bio-Rad Laboratories, Inc., #1610710) and heated for 5 min. Proteins were resolved in 4–20% Criterion TGX Stain free gels (Bio-Rad Laboratories, Inc. #5678095) and transferred onto 0.2 μm polyvinylidene fluoride membranes (Bio-Rad Laboratories, Inc., #1704157) with the condition of mixed, high, or low molecular weight transfer (depending upon molecular weight of protein of interest) by Trans-Blot Turbo system (Bio-Rad Laboratories, Inc.). Membrane was blocked with 5% nonfat dry milk in tris-buffered saline-tween 20 (TBST) for 1 h at room temperature and then incubated with respective primary antibody at 4°C overnight. The following antibodies were used to probe the proteins of interest: rabbit-anti APP (Sigma, A8717, 1:5000), mouse anti-phospho-tau (Ser 202, Thr 205) (Invitrogen, MN1020B, 1: 1000), mouse anti-total-tau (T46) (Thermo-Fisher Scientific, #13–6400, 1:2000), rabbit anti-phospho-tau (Thr 217) (Cell Signaling Technology, #51625, 1: 2000), mouse anti-ZO1 (Thermo-Fisher Scientific, #33–9100, 1:500), rabbit anti-DNP (Millipore Sigma, kit #S7150, #90451, 1: 500), mouse anti-β-Actin (Santa Cruz Biotechnology, sc-47778,1:1000), mouse anti- NeuN (Millipore, MAB377, 1:1000), rabbit anti-GFAP (Cell Signaling Technology, #12389, 1:1000), rabbit anti-PSD95 (abcam, ab18258, 1:1000), mouse anti-GAPDH (EMD Millipore Cor., MAB374, 1:5000). The next day, the membrane was washed with TBST (3 × 5 min) and incubated with horseradish peroxidase-conjugated secondary antibodies for 1 h. After washing of secondary antibodies (TBST, 3 × 5 min), the membrane was developed by Super Signal West Femto Maximum Sensitivity Substrate (Thermo Scientific, #34096) and the band was visualized by ChemiDoc Imaging System (Bio-Rad) and in most cases auto optimal condition of the instrument was used. Exposure was set manually in some instances when bands were supersaturated or too faint. Image Lab version 6.0.1 (Bio-Rad) was used to analyze the bands.

Immunohistochemistry

For immunofluorescent staining of 6E10 and 500 μM ThioS, 40 μm brain sections were washed with PBS (3 × 3 min) and permeabilized with 0.25% Triton X-100 and blocked with 5% bovine serum albumin (BSA) and 5% normal horse serum (NHS) for 1 h at room temperature. Sections were incubated overnight with mouse anti-6E10 (Biolegend, 803001, 1:200) at 4°C and then with Alexa flour 594 donkey anti-mouse (Thermo-Fisher Scientific, A32744, 1:1000). Sections were then washed with PBS and incubated with 500 μM ThioS (Sigma, T1892) in 50% ethanol for 7 min. Sections were washed with 80% ethanol (2 × 3 min) then 95% ethanol (1 × 3 min) followed by one wash with distilled water and floated on the slide and mounted by VESTASHIELD mounting media (Vector Laboratories, H-1000). For NeuN, GFAP, Iba1, CD13, and CD31 staining, sections were washed with PBS and permeabilized with 0.25% Triton X-100 and blocked with 5% BSA and 5% NHS (5% BSA and 5% Normal donkey serum (NDS) for CD13, CD31) for 1 h at room temperature. Sections were incubated overnight with primary antibodies (mouse anti-NeuN; EMD Millipore Cor, #MAB377, 1:500; mouse anti-GFAP, Thermo-Fisher Scientific, MA5-12023, 1:1500; rabbit anti-Iba1, Fujifilm, 019–19741, 1:500, goat anti-CD13, R & D system, # AF2335, 1:100; rat anti-CD31, BD Biosciences, # 550274, 1:100) at 4°C. The next day, sections were washed three times with PBS and incubated with secondary antibodies (Alexa Fluor 488 goat anti-mouse, Thermo Fisher Scientific, A32723, 1:200; Alexa Fluor 594 goat anti-rabbit, Thermo Fischer Scientific, A32740, 1:200) in 1% BSA for 1 h (1% NDS +1% BSA for 2 h for CD13, CD31) at room temperature. Sections were mounted onto microscope slides (Fisher Scientific # 12-550-15) and then coverslipped with Prolong diamond antifade mountant (Invitrogen, P36961). DNA damage was analyzed using the TUNEL assay kit from Cell Signaling (# 25879), following the exact method described in the kit. Briefly, the free-floating sections were washed three times with PBS and then permeabilized for 30 min. After equilibration for 5 min, sections were incubated with TUNEL reaction buffer for 2 h at 37°C. Finally, the sections were co-labeled with DAPI, mounted onto slides, and coverslipped for further analysis. Reactive oxygen species were analyzed by anti 4-hydroxynonenal (4-HNE) or anti-nitrotyrosine staining in free-floating sections blocked in 5% normal goat serum (S-1000, Vector Laboratories) and incubated overnight with rabbit anti-HNE (Alpha diagnostic International, #HNE11S, 1:500) or rabbit anti-3NT (Millipore Sigma, # AB5411, 1:500). On the following day, sections were incubated with goat anti-rabbit Alexa 594 or 488 (Invitrogen # A32740, #A32731,1:300) for two hours at room temperature, washed in PBS, and mounted

CellPress
OPEN ACCESS

using an antifade aqueous media (Vectashield Plus with DAPI, Vector Laboratories). Images were acquired on LSM 880, and mean fluorescence intensities were quantified on Fiji ImageJ.

Cytokine analysis

Mouse brain hippocampus was homogenized in RIPA buffer containing protease and phosphatase inhibitor cocktail. Sample were centrifuged at 10,000 x g for 10 min at 4°C and supernatant was collected. Protein concentration was measured by BCA method and an equal amount of samples were analyzed by mouse cytokine 32-plex discover assay (Eve technology, Canada).

Hippocampal neuronal survival

Survival of young hippocampal neurons was performed by BrdU labeling, as previously described.[69] Briefly, for labeling newborn neurons a single dose of BrdU (150 mg/kg, i.p) was injected at the 5th month in mid-disease and 11th month in advanced disease cohort along with P7C3-A20/vehicle injection. Thereafter P7C3-A20/vehicle injections were continued up to the 6th month in mid-disease and 12 months for the advanced disease cohort. Brain tissue was harvested, and sectioning was performed as described above. To measure survival of newborn hippocampal neurons, the number of BrdU+ cells/mm3 in the dentate gyrus was measured 30 days after BrdU injection. Free-floating 40 μm thick sections were stained for BrdU, and unmasking of BrdU was achieved by incubating the tissue sections for 2 h in 50% formamide/2 x saline sodium citrate (SSC) at 65°C followed by a 5 min wash in 2 X SSC and subsequent incubation for 30 min in 2 M HCL at 37°C. Sections were processed for immunohistochemical staining with mouse monoclonal anti-BrdU (Sigma, SAB4700630, 1:100). The number of BrdU+ cells in the entire dentate gyrus and subgranular zone (SGZ) was quantified by counting BrdU+ cells within the SGZ and dentate gyrus in every fifth section throughout the entire hippocampus and then normalized for dentate gyrus volume using Nikon Metamorph and NIH ImageJ software with appropriate conversion factors.

Blood brain barrier integrity analysis

Blood-brain barrier (BBB) was analyzed by transmission electron microscopy (TEM) in the Cryo- Electron Microscopy Core facility of Case Western Reserve University, as previously described.[89] Briefly, brain sections were washed three times with PBS and then fixed by quarter strength Karnovsky's fixative solution for 2 h at room temperature. Sectioned were washed and postfixed for 2 h in an unbuffered 1:1 mixture of 2% osmium tetroxide (Electron Microscopy Science, 19110) and 3% potassium ferricyanide (Electron Microscopy Science, 20150). Sections were rinsed with distilled water and soaked overnight in an acidified solution of 0.25% uranyl acetate (Electron Microscopy Science, 22400). Sections were rinsed again and passed through ascending concentration of ethanol for dehydration and passed through propylene oxide (Electron Microscopy Science, 20401) and embedded in an EMbed 812 embedding media (Electron Microscopy Sciences, T300-Ni). Thin sections (70 nm) were cut on an RMC MT6000-XL ultramicrotome and mounted onto Gilder square 300 mesh nickel grids (Electron Microscopy Sciences). Sections were subsequently stained with acidified methanolic uranyl acetate and modified Sato's triple lead stain. These sections were coated finally on a Denton DV-401 carbon coater (Moorestown, NJ) and examined in an FEI Tecnai Sprit (T12) with a Gatan US4000 4k x 4k resolution charge-coupled device.

For analysis of IgG extravasation, brain sections were washed with PBS. Endogenous peroxidase activity was quenched by incubation of brain sections in 1% H_2O_2 for 45 min and nonspecific staining was blocked by incubating the sections in 5% BSA. Sections were incubated in biotinylated anti–mouse IgG antibody (Vector Laboratories #BA-2000, 1:500) overnight at 4°C. Sections were washed with PBS (3 × 5 min) and incubated with avidin–biotin complex (ABC kit, Vector Laboratories # PK-4000) and developed using 3,3′-diaminobenzidine (DAB) (Peroxidase Substrate Kit, Vector Laboratories DAB # SK-4100). Brain sections were mounted onto the slides and cleared in xylene, and coverslipped.

Reactive oxygen species detection through CellROX green and MitoSOX red

Briefly, cells were maintained and grown in the complete classic medium (Cell systems #4Z0-500) at 37°C in 95% air and 5% CO_2 in a humidified incubator. At 80–90% confluency, cells were trypsinized, resuspended, and seeded into a 24-well black visiplate with a clear bottom (PerkinElmer LLC, USA). All experiments were performed on cells between passage number 7 to 10. P7C3-A20 was dissolved in DMSO, and further dilutions were made in complete media with serum. On the following day, cells were treated with either Vehicle, 0.1 mM H_2O_2, or 5 μM P7C3-A20 in the presence of 0.1 mM H_2O_2. After 24 h of treatment, cells were loaded with CellROX green reagent (ThermoFisher Scientific #C1044) at a final concentration of 5 μM and incubated at 37°C for 30 min. Thereafter, cells were washed and maintained in PBS for imaging. Images were captured immediately on the EVOS system using a GFP filter, after which cells were permeabilized with 0.5% Triton X-100 for 10 min, and fluorescence was read at excitation and emission of 485 and 520 nm, respectively. For the MitoSOX assay, cells were seeded either into 35 mm glass bottom Petri dishes (MatTek, Ashland, MA, USA, P35G-1.5-14-C) or 24-well black visiplate with a clear bottom (PerkinElmer LLC, USA). All treatments were similar to CellROX green experiments. Following treatments, cells were loaded with MitoROX red Reagent (ThermoFisher Scientific, M36008) at a final concentration of 5 μM and incubated at 37°C for 30 min. Thereafter, cells were washed, stained with Hoechst 33342, and maintained in HBBS for imaging. Images were captured immediately on a Zeiss fluorescent microscope. For quantitative estimation, cells grown and treated in visiplates were permeabilized with 0.5% Triton X-100 for 10 min, and fluorescence was read at excitation and emission of 396 and 610 nm, respectively.

Image acquisition and quantification of immunohistochemistry

Images were acquired by using Axio scan.Z1 (Zeiss) slide scanner or Axio Imager.M2 (Zeiss). In each set of experiments, light intensity and exposure time were kept constant. ImageJ version 1.42 software (National Institute of Health, Bethesda, MD) was used for image analysis. Percent area occupied by ThioS, 6E10, GFAP, Iba1, and NeuN in the whole hippocampus and whole cortex was measured. Integrated density of IgG was measured in the cortex and hippocampus. The fold change pericyte coverage was measured by % area occupied by C13 in CD31 positive area. Analysis conditions were kept identical throughout the group for each staining. All analysis was performed blindly for each treatment group.

Measurement of mitochondrial respiration

Mitochondrial oxygen consumption rate (OCR) was measured using the Seahorse XFe96 Analyzer. HBMVECs were seeded (approximately 10,000 cells per well) in a sterile 96-well culture plate provided in the XFe96 Flux Pak (Agilent, 102601) and maintained for 24 h in Complete Classic Cell Medium with serum and CultureBoostTM (Cell System, 4Z0-500) until they reached approximately 70–80% confluency. Cells were then incubated with either 100 μM H_2O_2 or control media for 15 min, and subsequently treated with either vehicle, different concentrations of P7C3-A20 (1 μM, 3 μM, 5 μM), or 3 μM P7C3-A20 along with FK866. Plates were then incubated for an additional 24 h at 37°C in a humidified incubator containing 5% CO2. The following day, mitochondrial assay media was prepared using XF DMEM (Agilent, 103680), fortified with 1 mM pyruvate (Agilent, 103578), 2 mM glutamine (Agilent 103579), and 10 mM glucose (Agilent, 103577). Mitochondrial complex inhibitors provided in the Cell Mito Stress Test kit (Agilent, 103015) were reconstituted in the mitochondrial assay media at the following 10x stock concentrations: oligomycin (12 μM), FCCP (10 μM), and Rotenone/Antimycin A (8.8 μM), and each was loaded into the corresponding, pre-calibrated plate as described in the Cell Mito Stress Test User Guide. Media was gently aspirated from the cell culture plate and replaced with 180 μL pre-warmed mitochondrial assay media. Cells were then incubated for 45 min at 37°C in a humidified incubator containing 5% CO2 and then subjected to the ''Cell Mito Stress Test'' protocol pre-loaded on the Seahorse XFe96 Analyzer.

Protein carbonylation

Protein oxidation was assessed by estimating total protein carbonylation using the OxyBlot Protein Oxidation Detection Kit (Millipore Sigma, #S7150). Briefly, tissue was lysed in RIPA buffer, and 5 μg of homogenate was denatured using an equal volume of 12% SDS. Denatured samples were derivatized with 2,4-dinitrophenylhydrazine (DNPH), which enabled detection of carbonyl residues. Then, the derivatized samples were resolved on SDS-PAGE and detected with an anti-DNP antibody.

Ex vivo electrophysiology study

Brain slices were prepared by dissecting six and twelve-month-old mouse brains by decapitation and immediately submerging into ice-cold and oxygenated cutting solution (110 mM sucrose, 60 mM NaCl, 3 mM KCl, 28 mM $NaHCO_3$, 1.25 mM NaH_2PO_4, 5 mM glucose, 0.6 mM ascorbate, 7 mM $MgCl_2$, and 0.5 mM $CaCl_2$). Brain tissue was cut into 400 mm parasagittal sections in a cutting solution using Leica VT1200. Mouse hippocampal slice sectioning was done as described previously.[232] Briefly, the hippocampus slice was dissected and maintained in room temperature cutting solution diluted 1:1 with artificial cerebrospinal fluid (ACSF) (in mM): (125 mM NaCl, 2.5 mM KCl, 26 mM $NaHCO_3$, 1.25 mM NaH_2PO_4, 25 mM glucose, 1 mM $MgCl_2$, and 2 mM $CaCl_2$) for 20 min with constant 95% O_2/5% CO_2 perfusion. Slices were transferred and maintained in ACSF with constant 95% O_2/5% CO_2 perfusion for another 20 min before being transferred to the brain slice recording chamber (BSC1, Scientific Systems Design Inc.). *ex vivo* electrophysiology recording in mice hippocampal slices was performed as described previously.[233] Briefly, brain slices were recovered for a minimum of 40 min before being transferred into the recording chamber, where temperature was held at 30° ± 0.5°C by Proportional Temperature Controller (PTC03, Scientific Systems Design Inc.). The ACSF flow rate was kept at 1 mL/min. Field excitatory postsynaptic potential (fEPSP) was recorded from stratum radiatum in hippocampal area CA1 via glass electrode (1–4 MΩ) loaded with ACSF. A stimulating electrode made by the formvar-coated nichrome wire (A-M Systems) was positioned on the Schaffer collaterals arising from the CA3 region, which was used to deliver biphasic stimulus pulses (100 μs duration). The electric stimulation, controlled by pClamp 11 software (Molecular Devices), was delivered via the Digidata 1550B interface (Molecular Devices) and a stimulus isolator (model 2200; A-M Systems). The evoked signals were amplified using a differential amplifier (model 1800; A-M Systems), filtered at 10 Hz low cut-off, 20 kHz high cut-off, and digitized at 10 kHz. Input-output was performed at 0.5 mV increments to yield the maximum response. A stimulus intensity that would evoke less than 50% of the maximum fEPSP response was determined and used in all the electrophysiological recordings. A 20 min baseline fEPSP was recorded at 0.05 Hz as a control before the long-term potentiation (LTP) induction. LTP was induced by a high-frequency theta burst stimulation (TBS), which consisted of five trains of 200 Hz in 20 ms duration separated by 200 ms, repeated 6 times at 10 s intervals. A 60 min fEPSP was recorded at 0.05 Hz following the TBS.

Label-free quantitative proteomic analysis

Sample preparation

Hippocampal brain tissue was homogenized in 500 μL of ice-cold radioimmunoprecipitation assay (RIPA) buffer (Sigma-Aldrich, R0278), supplemented with 1x phosphatase and protease inhibitors (Thermo Scientific, 1861284). The samples were allowed to stand for 15 min at 4°C and then sonicated. Following sonication, they were centrifuged at 18,000 x g at 4°C for 30 min. The

CellPress
OPEN ACCESS

supernatant obtained from this step was used for proteomic analysis. In brief, 200 μg of total proteins were ship on dry ice to Creative Proteomics (Shirley, New York, USA), where the proteins were precipitated using cold acetone. The proteins were then dissolved in 2M urea and denatured with 10 mM dithiothreitol (Sigma-Roche, 10 197 777 001) at 56°C for 1 h, followed by alkylation with 50 mM Iodoacetamide (Sigma, A3221) for 60 min in the dark at room temperature. Next, 500 mM ammonium bicarbonate (Sigma, A6141) was added to achieve a final concentration of 50 mM ammonium bicarbonate with a pH of 7.8. The samples were digested with Promega Trypsin (Promega, V5111) for 15 h at 37°C. The resulting peptides were further purified using a C18 SPE column (Thermo Scientific), lyophilized, and then resuspended in 20 μL of 0.1% formic acid (Sigma, 1.59013) for LC-MS/MS analysis.

Nano LC-MS/MS analysis

Nanoflow UPLC, Ultimate 3000 nano UHPLC system (Thermo Scientific, Waltham, MA) was used for the study. Nanocolumn was conditioned and 1 μg of sample was loaded with a mobile phase A 0.1% formic acid in water and mobile phase B 0.1% formic acid in acetone with total flow rate of 250 nL/min. LC linear gradient was performed from 2 to 8% buffer B in 5 min, from 8% to 20% buffer B in 60 min, from 20% to 40% buffer B in 33 min, then from 40% to 90% buffer B in 4 min. Mass Spectrometry was performed by full scan between 300-1,650 m/z at the resolution 60,000 at 200 m/z, the automatic gain control target for the full scan was set to 3e6. The MS/MS scan was operated in Top 20 mode using the following settings: resolution 15,000 at 200 m/z; automatic gain control target 1e5; maximum injection time 19ms; normalized collision energy at 28%; isolation window of 1.4 Th; charge sate exclusion: unassigned, 1, >6; dynamic exclusion 30 s.

Data analysis

Raw MS files were analyzed and searched against mouse protein database based on the species of the samples using Maxquant (1.6.2.14). The parameters were set as follows: the protein modifications were carbamidomethylation (C) (fixed), oxidation (M) (variable); the enzyme specificity was set to trypsin; the maximum missed cleavages were set to 2; the precursor ion mass tolerance was set to 10 ppm, and MS/MS tolerance was 0.5 Da. Data was normalized and the cutoff value between the groups was ±1.25-fold change with p-value $\leq$0.05 was considered significant for further bioinformatics analysis. The group normalized data for both male and female is represented in Data S1.

Bioinformatics analysis

Global protein changes across different groups were analyzed and visualized using VolcaNoseR.[234] In this analysis, the $\log_{10}$ (fold change) of each protein was plotted on the x axis against the $\log_{10}$ of its p-value on the y axis. Proteins with a p-value of $\leq$0.05 and a fold change $\geq$1.25 are represented as red dots, indicating upregulated proteins. Conversely, proteins with a p-value of $\leq$0.05 and a fold change $\leq$1.25 are represented as blue dots, indicating downregulated proteins. The identified proteins, which showed statistically significant changes in abundance, were then used for Gene Ontology (GO), Kyoto Encyclopedia of Genes and Genomes (KEGG), and Reactome pathway analyses across different groups. Enrichment analysis was conducted using the Mus musculus database for mice and Homo sapiens, employing ShinyGO V0.80.[235] Top five enrichment terms with least FDR value for up and down regulated proteins were represented in the graph. Data visualization for all the enrichments, including the heatmap, was created using SRplot.[236]

Human database analysis

The proteomic label changes observed in 5xFAD VEH mice were examined in the report compiled by Askenzi et al. (2023),[228] which is based on 38 published reports on Alzheimer's disease (AD) proteomics. We focused on proteins that were altered at different clinical stages of AD, as detailed in supplementary data 5 of Askenzi et al.[228] We analyzed the significantly differentially expressed proteins in 5xFAD VEH mice compared to wild-type (WT) VEH mice, applying a p-value threshold of $\leq$0.05 and a fold change of $\geq$1.25. We checked for similar directional changes of these proteins at various stages of AD as reported in the article. The NeuroPro Score for each identified protein is indicated in the heatmap (Figure 6H). For the human transcriptomic database, we explored the transcriptome patterns of the identified differentially expressed proteins (DEPs) using the public, large-scale single-nuclei RNA sequencing dataset from The Seattle Alzheimer's Disease Brain Cell Atlas (SEA-AD) consortium (https://portal.brain-map.org/explore/seattle-alzheimers-disease/whatis and Gabitto et al., 2024).[229] This dataset includes samples from two brain regions: the middle temporal gyrus (MTG) and the dorsolateral prefrontal cortex (DLPFC). Using a pseudo-bulk based method (muscat1),[237] we conducted differential expression analysis (AD vs. healthy controls) for female and male donors across different brain regions and cell types (Figures 6, S7I, and S7J). The significant differentially expressed genes (DEGs) are defined by a p-value of <0.05 and |logFC| > 0.25, and these are highlighted in the heatmap.

QUANTIFICATION AND STATISTICAL ANALYSIS

All statistical analysis and graphical representations were performed using GraphPad Prism, version 10.2.3 (GraphPad Software, Inc.). For analysis of two groups, the Student's t test was performed. For multiple group analysis, one-way ANOVA or repeated-measured two-way ANOVA with Dunnett's post hoc test were used when appropriate. Data are shown as mean ± SEM. For the 5xFAD study, blue dots represent female animals and red dots represent male animals. p-value below or equal to 0.05 was considered significant. For mayo Banner temporal cortex bulk RNA sequencing dataset, count data were normalized using TNN method with edgeR package, and differential gene expression was performed with linear regression. Different significant levels 0.05, 0.01, 0.001, and 0.0001 were represented by *, **, ***, and **** respectively. Individual significance levels for each figure were described in the specific figure legends.